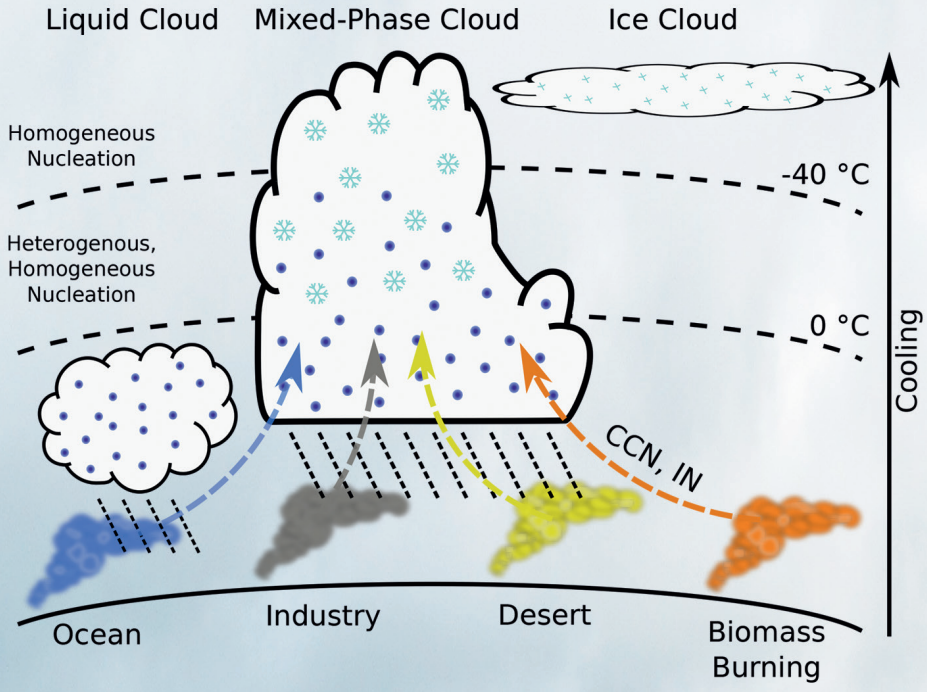

Ice Crystal Measurements with the New Particle Spectrometer NIXE-CAPS

Jessica Meyer

Mitglied der Helmholtz-Gemeinschaft

JÜLICH
FORSCHUNGSZENTRUM

Schriften des Forschungszentrums Jülich
Reihe Energie & Umwelt / Energy & Environment Band / Volume 160

Forschungszentrum Jülich GmbH
Institute for Energy and Climate Research (IEK)
Stratosphere (IEK-7)

Ice Crystal Measurements with the New Particle Spectrometer NIXE-CAPS

Jessica Meyer

Schriften des Forschungszentrums Jülich
Reihe Energie & Umwelt / Energy & Environment Band / Volume 160

ISSN 1866-1793 ISBN 978-3-89336-840-2

Bibliographic information published by the Deutsche Nationalbibliothek.
The Deutsche Nationalbibliothek lists this publication in the Deutsche Nationalbibliografie; detailed bibliographic data are available in the Internet at http://dnb.d-nb.de.

Publisher and Distributor:	Forschungszentrum Jülich GmbH Zentralbibliothek 52425 Jülich Phone +49 (0) 24 61 61-53 68 · Fax +49 (0) 24 61 61-61 03 e-mail: zb-publikation@fz-juelich.de Internet: http://www.fz-juelich.de/zb
Cover Design:	Grafische Medien, Forschungszentrum Jülich GmbH
Printer:	Grafische Medien, Forschungszentrum Jülich GmbH
Copyright:	Forschungszentrum Jülich 2013

Schriften des Forschungszentrums Jülich
Reihe Energie & Umwelt / Energy & Environment Band / Volume 160

D 468 (Diss., Wuppertal, Univ., 2011)

ISSN 1866-1793
ISBN 978-3-89336-840-2

The complete volume is freely available on the Internet on the Jülicher Open Access Server (JUWEL) at http://www.fz-juelich.de/zb/juwel

Abstract

Mixed-phase clouds consist of liquid droplets and ice crystals and appear in the temperature range between 0 °C and 40 °C. They are in the focus of recent research because model studies indicate that their degree of glaciation have an impact on the cloud radiative properties.

Up to now, mainly the measurement of bulk liquid and ice water content is used to investigate the mixed-phase cloud glaciation process. This study, for the first time, presents extensive size resolved laboratory and aircraft based in-situ mixed-phase cloud observations. For this purpose, the Novel Ice EXpEriment - Cloud and Aerosol Particle Spectrometer (NIXE-CAPS), an established cloud particle instrument, but equipped with an additional depolarization detector to distinguish ice crystals and liquid droplets, is used. The complete set of measured parameters includes concentration and phase of cloud particles in the size range of 0.61 µm to 937.5 µm. Here, the dependence of mixed-phase cloud glaciation on the initial number of ice active aerosol, relative humidity and temperature is investigated for clouds generated in the AIDA cloud chamber and for natural clouds observed on board of the British aircraft BAE146 during the COALESC campaign over the UK in 2011 .

A significant difference in the degree of glaciation is found for AIDA mixed-phase clouds evolved in either sub- or supersaturated humidity conditions with respect to water (RH_w). The droplet concentration in supersaturated RH_w regimes is constantly high (around 500 cm^{-3}) over the whole temperature range, since the droplets do not evaporate (droplet-ice coexisting regime). Under subsaturated conditions where evaporation of droplets occurs (Wegener-Bergeron-Findeisen regime), their concentrations decrease with temperature from about 100 cm^{-3} at 270 K to 1 cm^{-3} at 235 K. This decrease in droplet concentration is most likely caused by the increasing difference of the water vapor saturation pressure with respect to liquid and ice. Hence, the droplet concentration in mixed phase clouds seems to be mainly driven by the dynamic situation. The number of ice nuclei in the AIDA chamber and thus the ice crystal concentration of the AIDA clouds was constantly high. In the droplet-ice coexistence regime, where also high liquid droplet concentrations are observed, the resultant number fraction of frozen cloud particles is only about 10 % for all temperatures. In contrast, in the subsaturated Wegener-Bergeron-Findeisen regime, the ice number fraction increases with decreasing droplet concentration from about 20 % at 270 K up to 80 % at 235 K. Thus, the colder AIDA clouds in the Wegener-Bergeron-Findeisen regions show a high degree of glaciation which is expected for Wegener-Bergeron-Findeisen conditions, but complete glaciation does not occur. Nevertheless, the ice mass fraction is very close to 100 %, since the remaining particles classified as droplets are only small.

The COALESC natural clouds are found to be almost all in the Wegener-Bergeron-Findeisen regime with droplet numbers decreasing with temperature, as for the AIDA clouds. However, the number of ice nuclei in the atmosphere is much lower than in the AIDA chamber. Thus, the ice number fraction observed for the COALESC natural clouds ranges only from about 2 % at 270 K up to 20 % at 235 K. It is much lower than for the respective AIDA

clouds which glaciated in an environment with a very high number of ice nuclei. The measurements in the AIDA and COALESC mixed-phase clouds illustrate how the degree of glaciation in mixed-phase clouds is determined by both the thermodynamic situation of the cloud and the number of ice nuclei, and, most interestingly, that coexistence of droplets and ice is possible in natural mixed-phase clouds in the Wegener-Bergeron-Findeisen regime, where complete glaciation is believed to be the most probable state.

Zusammenfassung

Mischwolken bestehen aus Wassertropfen und Eiskristallen und kommen im Temperaturbereich zwischen 0 °C und 40 °C vor. Sie sind derzeit Gegenstand intensiver Forschung, da Simulationsrechnungen darauf hindeuten, dass der Grad der Vereisung einen wesentlichen Einfluss auf die Strahlungseigenschaften dieses Wolkentyps hat.
Bisher wird zumeist der integrale Wasser- und Eisgehalt zur Untersuchung des Vereisungsprozesses in Mischwolken herangezogen. In dieser Arbeit werden zum ersten Mal umfassende größenaufgelöste Labor- und flugzeugbasierte in-situ-Messungen an Mischwolken vorgenommen. Diese Messungen wurden mit dem Novel Ice EXpEriment - Cloud and Aerosol Particle Spectrometer (NIXE-CAPS), einem etablierten Wolkenpartikelmessgerät durchgeführt, welches um einen Polarizationsdetektor erweitert wurde um zwischen Tropfen und Eiskristallen unterscheiden zu können. Die gemessenen Instrumentparameter umfassen unter anderem die Konzentration und die Phase von Wolkenpartikeln im Größenbereich zwischen 0.61 µm und 937.5 µm. In dieser Studie wird die Abhängigkeit des Vereisungsgrades in Mischwolken von der Anzahl der Eiskondensationskeime, der relativen Feuchte und der Temperatur in künstlich in der AIDA-Kammer erzeugten und natürlichen Wolken, die 2011 an Bord des britischen Forschungsflugzeugs BAE146 während der COALESC-Kampagne über Großbritannien beobachtet wurden, untersucht.
Bei Mischwolken, die bei unter- oder übersättigter relativer Feuchte bezüglich Wasser (RH_w) in der AIDA-Kammer erzeugt wurden, konnten signifikante Unterschiede im Vereisungsgrad festgestellt werden. Die Tropfenkonzentration in übersättigten RH_w Umgebungen ist im gesamten Temperaturbereich konstant hoch (um 500 cm^{-3}), da keine Verdampfung der Wassertropfen stattfindet (Wasser und Eis Koexistenz-Regime). Bei untersättigten Bedingungen verdampfen die Tropfen hingegen (Wegener-Bergeron-Findeisen Regime) und ihre Konzentration nimmt mit sinkender Temperatur von etwa 100 cm^{-3} bei 270 K auf 1 cm^{-3} bei 235 K ab. Dieser Abfall wird sehr wahrscheinlich durch die steigende Differenz zwischen den Wasserdampf-Sättingungsdrücken bezüglich Wasser und Eis verursacht. Die Tropfenkonzentration in Mischwolken wird also hauptsächlich durch die Dynamik bestimmt. Obwohl die Anzahl der Eiskondensationskeime und damit die Eiskristallkonzentration in den AIDA-Wolken auf einem konstant hohen Niveau lag, ergab sich hier im Wasser-Eis Koexistenz-Regime ein Anzahlanteil von gefrorenen Wolkenpartikeln von nur etwa 10 % bei allen Temperaturen. Im untersättigten Wegener-Bergeron-Findeisen Regime nimmt der Anzahlanteil der Eispartikel mit sinkender Temperatur und Tröpfchenanzahl von etwa 20 % bei 270 K bis zu 80 % bei 235 K zu. Die kälteren AIDA-Wolken im Wegener-Bergeron-Findeisen Regime zeigen daher einen hohen Vereisungsgrad, welcher dort auch erwartet wird. Vollständige Vereisung tritt jedoch nicht auf. Trotzdem ist der Massenanteil von Eis sehr nah an 100 %, da die verbleibenden als Tröpfchen klassifizierten Partikel sehr klein sind.
Wie sich herausstellte, befanden sich die natürlichen COALESC-Wolkenmessungen fast

alle im Wegener-Bergeron-Findeisen Regime, wo die Tropfenanzahl mit sinkenden Temperaturen äquivalent zu den AIDA-Wolken abnahm. Allerdings ist die Anzahl der Eiskondensationskeime in der Atmosphäre wesentlich geringer als in der AIDA-Kammer. Daher liegt der hier beobachtete Anzahlanteil der Eispartikel nur bei etwa 2 % bei 270 K bis zu 20 % bei 235 K, also wesentlich geringer als bei den AIDA-Wolken, welche in einer Umgebung mit einer hohen Anzahl von Eiskondensationskeimen stark vereisten. Die Messungen der AIDA- und COALESC-Mischwolken zeigen, dass der Vereisungsgrad von Mischwolken sowohl von der thermodynamischen Situation als auch von der Konzentration der Eiskondensationskeime abhängt. Die Messungen zeigen außerdem, dass die Koexistenz von Wasser und Eis in natürlichen Mischwolken im Wegener-Bergeron-Findeisen Regime möglich ist, obwohl der Zustand vollständiger Vereisung hier bis jetzt als wahrscheinlichster Zustand angenommen wurde.

Contents

1. Introduction

Some of the most fascinating atmospheric phenomena such as halos or rainbows are connected to the presence of clouds within the atmosphere. Often the clouds themselves have beautiful colors and forms. Besides their physical appearance clouds also play a major role for a variety of different atmospheric processes. Their presence initiates precipitation and influences the atmospheric radiative and chemical balance. However, due to the diversity of different cloud forms and their natural spatial and temporal variability many cloud properties are still unknown.
One cloud type, for which the formation and evolution process is not well-understood, is the mixed-phase type. In general mixed-phase clouds consist of liquid droplets and/or ice crystals. The temperature interval within which both liquid droplets and ice crystals can potentially coexist is limited to 0 °C and −40 °C (Viadaurre and Hallett, 2009, Shupe and Matrosov, 2006, Pinto et al., 2001). Mixed phase clouds account for 20 % to 30 % of the global cloud coverage (Ou et al., 2009).

Mixed-phase clouds play an important role in the global climate system. For example, they influence the radiation budget of the earth which is highlighted in Figure 1.1. Shortwave solar light which irradiates the earth is reflected by the mixed-cloud particles. On the other hand, the earth's long-wave radiation is absorbed by the cloud particles and re-emitted to the earth's surface. The first process has a cooling, the latter one a warming effect (Fu and Liou, 1993). To assess the radiative impact of mixed-phase clouds, properties such as cloud thickness, cloud cover or cloud altitude are of interest. However, the mixed-phase cloud composition (ice fraction, cloud particle concentration, cloud particle size and ice crystal shape) is as important (Sun and Shine, 1994, Ehrlich et al., 2009).

In Figure 1.2 the influence of the ice fraction on the total radiation budget of mixed-phase clouds is shown exemplary for an arctic mixed phase cloud (Ehrlich et al., 2009). In this model study the ice volume fraction is varied by assuming a constant total water path TWP, three different ice crystal effective diameters and a scaling of the water and ice concentrations at the same time. The overall simulated solar forcing is negative and thus the cloud has a cooling effect. It is shown that an increase of the ice volume fraction leads to a decrease of the cooling effect. The reason is that the ice crystals are usually larger than the liquid droplets in mixed-phase clouds. Thus fewer larger ice crystals add up to the same total water path for completely glaciated clouds compared to liquid clouds. The lower concentration of cloud particles in a pure ice cloud leads to a lower optical thickness and thus to a reduction of the cooling effect. This effect is stronger the larger the ice

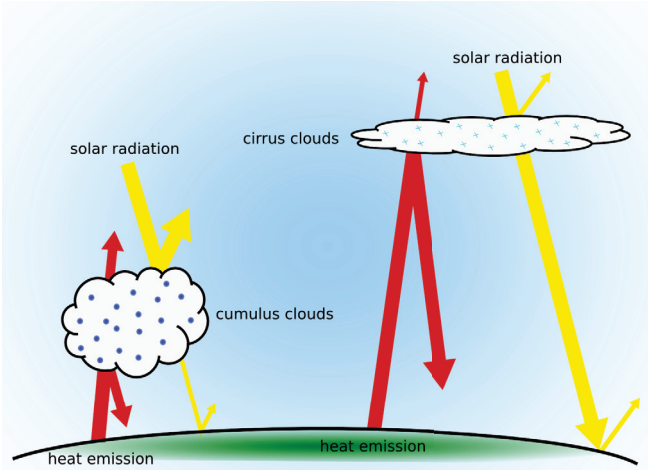

Figure 1.1.: Radiative impact that clouds have on the solar shortwave radiation and the longwave radiation emitted by the earth. The shortwave solar radiation is either reflected or transmitted depending on cloud height and cloud microphysical properties. The longwave radiation emitted by the earth is either absorbed and re-emitted to the earth surface or transmitted.

crystals are.
Ehrlich et al. (2008) also performed model studies to access the influence of ice crystal shape to the total radiative forcing of mixed-phase clouds. They concluded that non spherical ice crystals have a reduced volume compared to spherical particles which can lead to a reduction of the optical thickness and cloud top reflectance. Nevertheless, the effective size of the ice crystals play a crucial role. The larger the ice crystals are, the lower is their concentration compared to that of water droplets. Thus, for mixed-phase clouds containing a low concentration of large ice crystals the radiative cloud properties are driven by the liquid phase. The smaller the ice crystals are, the larger is their concentration compared to the liquid phase and the more important is their shape for modeling the cloud radiative feedback.
However, not only the amount and size but also the spatial distribution of liquid droplets and ice crystals (McFarquhar and Cober, 2004, Sun and Shine, 1994) or the temperature range over which mixed-phase clouds exist (Gregory and Morris, 1996, Moss and Johnson, 1994) lead to large deviations in the simulated mixed-phase cloud radiative feedback.
The impact of the atmospheric aerosol particles initiating the ice phase is also an important factor which potentially influences the mixed-phase cloud composition, properties and thus their radiative impact. The presence of these ice active aerosol particles, called Ice Nuclei (IN), can lead to rapid conversion of the liquid droplets into ice crystals ("glaciation effect", Solomon et al., 2007). Diehl et al. (2006) pointed out that the glaciation of a mixed-phase cloud is coupled with the release of latent head which in turn might increase the vertical updraft of the cloud. Thus the cloud can reach higher and colder altitudes.

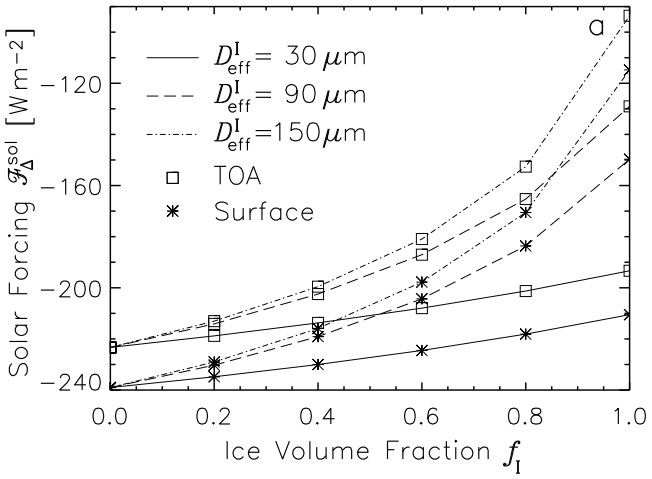

Figure 1.2.: Simulation of an arctic mixed-phase cloud which highlights the sensitivity of cloud radiative forcing to cloud ice fraction. To model the ice fraction, the total water path is held constant and different ice crystal effective diameters are assumed. The ice fraction is then varied by scaling the liquid and ice concentrations. The method leads to a decrease of the cloud radiative cooling due to a decrease of the cloud optical thickness τ. During cloud glaciation the total cloud number concentration decreases while the mean particle size increase which results in a decrease of τ.
Source: Ehrlich, A., M. Wendisch, E. Bierwirth, A. Herber, and A. Schwarzenböck, 2008: Ice crystal spape effects on solar radiative properties of artic mixed-phase clouds - dependence on microphysical properties. *Atmospheric Research*, 88:266–276, doi:10.1016/j.atmosres.2007.11.018 ©A. Ehrlich. Used with permission.

The formation of ice crystals in mainly liquid clouds can also lead to a fast growth of the ice crystals on the expense of the surrounding liquid droplets and thus to increased precipitation. The other way around an increased fraction of Cloud Condensation Nuclei (CCN), the part of the aerosol which catalyzes liquid drop formation, might cause more but smaller droplets and thus may suppress freezing ("thermodynamic effect", Solomon et al., 2007).
The level of scientific understanding for mixed-phase cloud formation and evolution is very low (Solomon et al., 2007). The need to understand the microphysical characteristics of mixed-phase clouds to improve numerical forecast modeling and radiative transfer calculations is of major interest in the atmospheric community (Sun and Shine, 1994, Gayet et al., 2009, Tremblay et al., 1996). Some of the key points which are of interest to accurately model the formation and evolution of mixed-phase clouds are:

- What physical processes initiate ice formation? How do the ambient aerosol particles affect the ice formation? Do they define the number and size of ice crystals in mixed-phase clouds at equilibrium state?

- How do the cloud characteristics such as ice crystal concentration, size and form evolve with time? How can the large variety of water and ice concentrations observed in mixed-phase clouds be explained?
- How are the liquid droplets and ice crystals distributed spatially? Are the liquid droplets and ice crystals mixed within the same cloud volume or are they spatially separated?
- How do temperature and humidity influence the mixed-phase state? Does the dynamical influence determine the mixed-phase cloud microphysical properties at equilibrium?
- How can the mixed-phase cloud microphysical properties be assessed experimentally?

These objectives are the basis for this thesis. The evolution of mixed-phase microphysical properties such as the number fraction of liquid droplets and ice crystals for different thermodynamic situations is investigated experimentally. Therefore, mixed-phase clouds generated at the Aerosol Interaction and Dynamics in the Atmosphere (AIDA) chamber of the Karlsruhe Institute of Technology (KIT) under controlled conditions as well as natural clouds observed over the United Kingdom territory are measured by using the Novel Ice EXpEriment - Cloud and Aerosol Particle Spectrometer (NIXE-CAPS), a new cloud spectrometer established at the Institute of Energy and Climate Research - 7 (IEK-7) in the frame of this study.

At the AIDA-chamber the following four experiments were performed (compare Table A.1): HALO02 in 2008, ACI03 in 2009, ACI04 in 2010 and BIO05 in 2010. In 2011, the COALESC campaign with the british aircraft BAE-146 took place out of Exeter, UK (compare Table A.2).

The structure of this thesis is as follows. Chapter 2 introduces mixed phase clouds including the freezing processes and microphysical structure. The new instrument NIXE-CAPS, which for the first time is able to distinguish ice crystals and liquid droplets for each cloud particle is described in Chapter 3. In Chapter 4 the laboratory and aircraft setups are presented and finally the results are discussed in Chapter 5. A summary and conclusion of this work is given in Chapter 6.

2. Mixed phase clouds

Traditionally cloud research is concentrated on low level liquid and high level ice clouds. Only within the last decade the cloud community focused on 'mixed-phase' clouds, which means that both water droplets and ice crystals are present. However, even in the cloud physics community no clear definition of the mixed-phase state exists. The following statements can be found in literature: "*...the definition of a mixed-phase cloud varied depending on the spatial and temporal resolution of the sampling instrument.*" (Spangenberg et al., 2006) "*...should a cloud be defined as mixed, if it has one ice particle per* 10^1 *or per* 10^{100} *droplets? Should a cloud be considered glaciated if it contains one liquid droplet per* 10^{100} *ice particles, or is it still mixed?*" (Korolev et al., 2003) "*...the mechanisms that support the formation, maintenance, and dissipation of these mixed-phase clouds are still poorly understood.*" (Spangenberg et al., 2006). In general, the exact specification of what an author regards as mixed-phase is stated in each publication.
For this thesis, the term mixed-phase is widespread. All clouds are regarded as mixed-phase as long as the air temperature is below 0 °C and above −40 °C, since only in this supercooled temperature interval the coexistence of both liquid water and ice is possible (Pruppacher and Klett, 1997). Further, the total number concentration of cloud particles larger than 3 µm diameter must exceed 0.01 cm^{-3} due to the instrument resolution.
The formation and evolution of a mixed-phase cloud is sketched in Figure 2.1. Mixed-phase clouds containing a large amount of liquid droplets are more common for the warmer temperature intervals near 0 °C, whereas mostly glaciated clouds are more frequently observed at colder temperatures (Viadaurre and Hallett, 2009, Cober et al., 2001, Shupe and Matrosov, 2006). Mixtures of water droplets and ice crystals are found most often between −5 °C and −25 °C. Above 0 °C the ice phase becomes unstable so that ice particles evaporate or melt. Below −40 °C all liquid drops spontaneously freeze and the cloud consists of pure ice (Pruppacher and Klett, 1997).

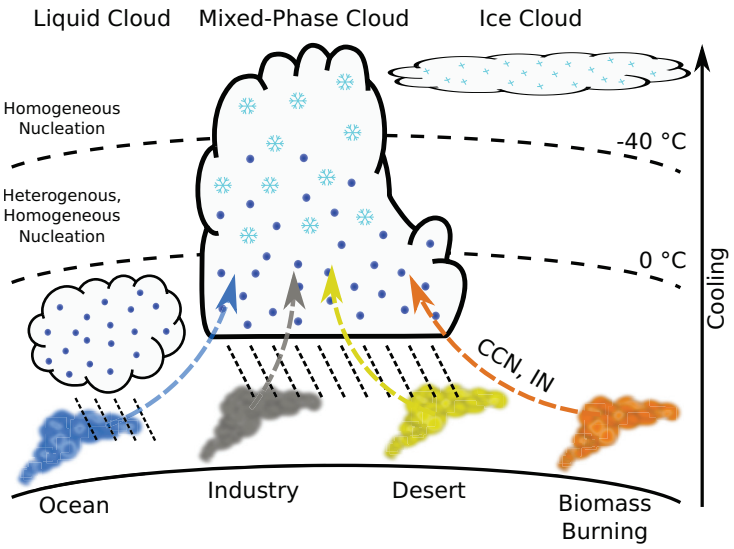

Figure 2.1.: Formation and evolution of a mixed-phase cloud. Additionally, the temperature regions where liquid and pure ice clouds persist, are indicated for comparison.

2.1. Formation

To better understand the formation process of liquid droplets and ice crystals in the atmosphere, the distribution of water molecules amongst the different water phases needs to be considered. In total three different water phases are present in the atmosphere: water vapor, liquid water and ice. Transitions between the different water phases within the atmosphere occur due to cooling or warming of air parcels.
In general, temperature and water vapor partial pressure have an influence on the water phase. The water phase diagram shown in Figure 2.2a indicates the temperature and partial pressure regions within which each phase is stable. Equilibrium between different phases exists on the boundaries separating the different phases. For the boundary between liquid and vapor, $e_w(T)$, the relative humidity with respect to water is defined by $RH_w = \frac{e_{gas}}{e_w} = 100\ \%$ whereas for the boundary between ice and vapor, $e_i(T)$, the relative humidity with respect to ice is defined by $RH_i = \frac{e_{gas}}{e_i} = 100\ \%$. e_{gas} describes the actual water vapor pressure. From here on, the index w and i describe liquid and ice conditions. Mathematically, the equilibrium between two phases is described by the Clausius-Clapeyron equation (Pruppacher and Klett, 1997). In the real atmosphere however equilibrium conditions deviate from the theoretical concept. The deviation is due to the concept of the phase diagram which assumes flat surfaces for all phases. In the atmosphere liquid water is present as spherical droplets whereas ice crystals can even have more complex forms. In addition, soluble and insoluble aerosol particles can act as Cloud Condensation Nuclei (CCN) or Ice Nuclei (IN) and thus alter the freezing and condensation relationships.

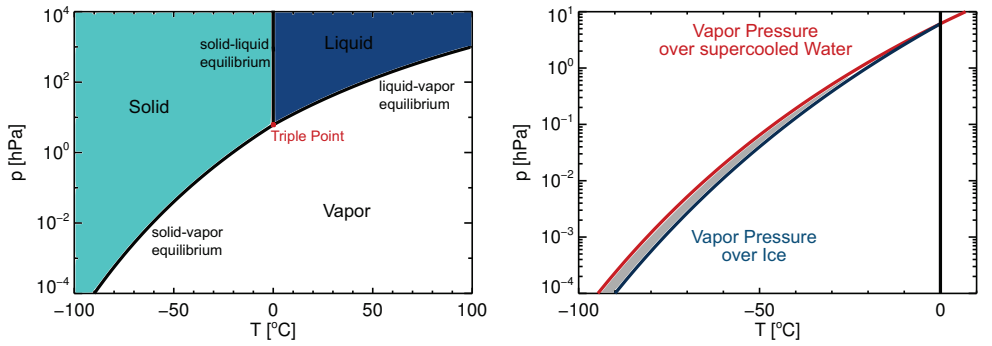

Figure 2.2.: a) Phase diagram of water which highlights the equilibrium conditions for the different water phases solid, liquid and vapor. Equilibrium between different phases is only possible at the phase boundaries. Furthermore equilibrium of all three phases only occurs at the triple point. b) Phase diagram which displays the saturation pressure of supercooled droplets and ice crystals. Below 0 °C the saturation pressure over supercooled water is higher than the saturation pressure over ice.

Liquid droplets and ice crystals form in supersaturated environments. Cloud formation generally occurs in uplifting air parcels. During the uplift the air expands and the air temperature decreases. As a result, the relative humidity with respect to water RH_w and ice RH_i increases. Water vapor condenses on the embedded aerosol particles. Soluble aerosol dissolve and liquid droplets form. Solid aerosol particles can then catalyze heterogeneous ice crystal formation and thus a mixed-phase cloud is formed.

2.1.1. Liquid droplets

Liquid droplet formation is in general initiated by CCN which can be either soluble or insoluble. The equilibrium between a soluble aerosol particle and humid air is described by the Köhler equation (Equation 2.1, Pruppacher and Klett (1997)).

$$S_{v/l} = 1 + \frac{A}{a} - \frac{B}{a^3} \tag{2.1}$$

with $A = \frac{2M_l\sigma_{l/a}}{RT\rho_l}$ and $B = \frac{2\nu m_s M_l}{4\pi M_l \rho_l}$. T is the air temperature, a the water drop radius, M_l the liquid molecular weight, $\sigma_{l/a}$ the surface tension of water, ρ_l the density, R the universal gas constant, ν the viscosity and m_s the salt mass.
The second term describes the influence of the aqueous solution drop curvature on the saturation pressure and the third term the influence of the solubility of the aerosol particle. The curvature of the droplet leads to an increased saturation partial pressure compared to flat surfaces. Furthermore, the saturation pressure variation increases for decreasing

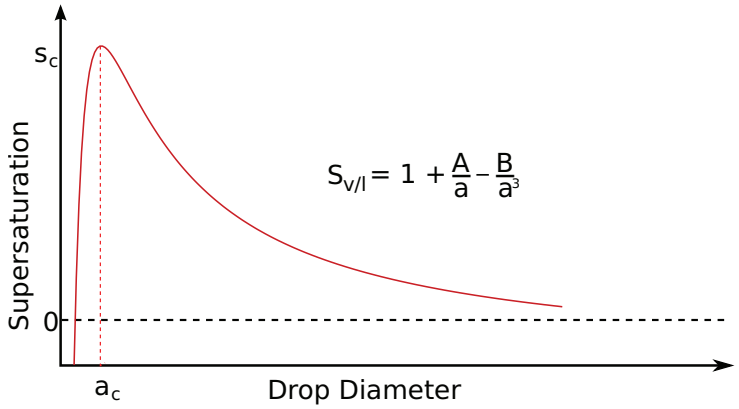

Figure 2.3.: Schematic trend of the Köhler equilibrium curve. The Köhler equation describes the equilibrium state between a soluble aerosol particle and humid air.

droplet size. The third term of Equation 2.1 describes that the critical saturation which corresponds to the maximum of the Köhler curve is increased for aerosol particles containing small amounts of salt. On the other hand the critical size a_c is then decreased to smaller values. Also, the larger the molar weight of the salt is (less soluble), the larger is s_c and the more a_c is shifted to smaller sizes.
An exemplary Köhler curve is displayed in Figure 2.3. The Köhler curve exhibit a maximum at a critical radius of $a_c = \sqrt{\frac{3B}{A}}$ which corresponds to a critical supersaturation of $s_c = \sqrt{\frac{4A^3}{27B}}$.

For aerosol sizes $a < a_c$ the equilibrium between the soluble aerosol and its surroundings is stable whereas for $a > a_c$ the situation is unstable. Unstable equilibrium implies that a perturbation of the ambient RH_w to higher values will induce aerosol growth whereas spontaneous reduction induces the evaporation of the aqueous solution droplet to a new equilibrium position. For $a < a_c$ the aqueous solution droplet may be in equilibrium with its surroundings for sub- or supersaturated conditions depending on the predominance of the curvature or solute term. On the other hand, once the critical value s_c is reached, the grown particle is in the unstable regime and grows further up to its maximum size as long as the environment is supersaturated.
The CCN properties of atmospheric aerosol particles and the implications on liquid cloud properties and climate is a wide field of research in the last decades (Solomon et al., 2007), which is beyond the scope of this thesis.

2.1.2. Heterogeneous ice formation

As already mentioned, most commonly drop formation proceeds the glaciation within mixed-phase clouds. Ice crystals are then produced via the liquid phase. The presence of solid aerosol particles catalyzes the formation of ice crystals (see Figure 2.1). Their ability to act as IN depend on their chemical and physical characteristics. Pruppacher and Klett (1997) present different laboratory and field studies which indicate that the size of the aerosol particles, their chemical bonds and crystallographic nature and their surface composition play a major role in heterogeneous ice formation, i.e. nucleation of ice on a preexisting solid IN. These studies indicate that the size of the IN has to be comparable to the size of an ice germ. Pruppacher and Klett (1997) concluded that the size of particles which act as IN, is typically larger than 0.1 µm. The studies also show an increased IN ability due to hydrogen analogue bonds on the aerosol surface and similar geometrical arrangement of the bond structure. The agglomeration of water molecules on a surface happens at distinct active sites. These sites can be edges in the molecular structure, screw dislocations or positions where the adsorption of water molecules is energetically favorable. The above mentioned characteristics depend on temperature. For mixed-phase clouds, the ice phase can be incorporated within or can be externally mixed with liquid droplets. The exact aerosol and ice interaction however is still under investigation. For example: "*The relative importance of the freezing modes in the atmosphere is not known, and in general our understanding of the physical and chemical processes underlying heterogeneous ice formation is limited.*" (Niedermeier et al., 2010) or "*...IN number concentrations at a single temperature, but in different locations and time periods, have been observed to span more than 3 orders of magnitude*" (DeMott et al., 2010) or "*How does enhanced aerosol affect ice crystal concentrations, sizes, habits and precipitation in mixed-phase clouds?*" (McFarquhar et al., 2010).
This thesis does not concentrate on ice nucleation on a specific aerosol type. Rather a wide variety of different CCN and IN active aerosol particles are considered. In fact the aerosol type known to be the dominant ice or cloud condensation nuclei for the specific experiment temperature range is selected.
Known heterogeneous nucleation mechanisms are immersion, condensation, deposition and contact freezing. The heterogeneous mechanisms are displayed in Figure 2.4. If the water vapor is directly adsorbed to the solid aerosol particle under supersaturated ice and subsaturated liquid conditions then the freezing process is called deposition nucleation. In the condensation mode the ambient air is supersaturated with respect to water and ice at temperatures below the melting point of ice. The freezing process is initiated directly after the condensation of water vapor on the solid particle surface. In mixed-phase clouds however these two processes are assumed to only be of minor importance. Contact and immersion freezing are believed to be the dominant ice nucleation mechanisms (Lohmann and Diehl, 2006). During contact nucleation an insoluble particle collides with a liquid droplet which then results in ice crystallization. During immersion freezing on the other hand the solid fragment is incorporated into a liquid droplet during drop activation by collision or secondary processes. At sufficiently low temperatures ice nucleation occurs on

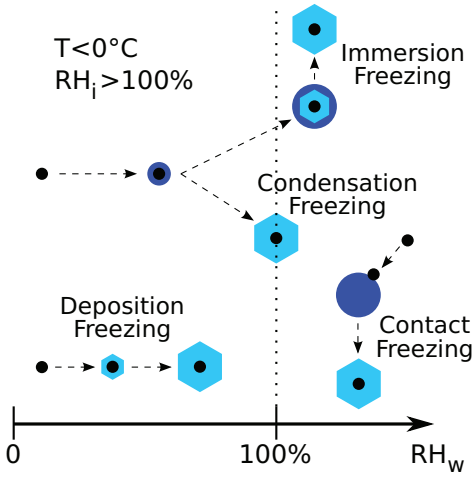

Figure 2.4.: Schematic of the different freezing mechanisms. In mixed-phase clouds the assumed dominant processes are immersion and contact freezing. During contact nucleation an insoluble particle collides with a liquid droplet which then results in ice crystallization. During immersion freezing a solid fragment is incorporated into a liquid droplet which at sufficiently low temperatures acts as ice nuclei.

the solid fragment.

As explained above, the ability of a solid aerosol particle to act as IN depends on its chemical and physical characteristics in dependence of the temperature and humidity conditions (DeMott et al., 2003). Potential solid aerosol particles are mineral dust, soot from industrial processes or biomass burning (Möhler et al., 2006), biological particles such as pollen and bacteria (Möhler et al., 2007), salt (Zuberi et al., 2001) or metallic particles (DeMott et al., 2003). One of the most active IN types found in the atmosphere is mineral dust (DeMott et al., 2003, Archuleta et al., 2005). Dust is efficiently transported from desert regions and thus affects aerosol compositions globally (e.g. Husar et al., 2001). Nevertheless, other solid aerosol types and especially soot are generally more common in the atmospherically relevant temperature range (Murphy et al., 2006) but are less active IN. Mineral dust activates to ice at low supersaturations over ice in the immersion and deposition mode. With decreasing temperature the fraction of active IN increases (Field et al., 2006, Cziczo et al., 2009, Möhler et al., 2006, Zobrist et al., 2008, Niedermeier et al., 2010, Marcolli et al., 2007, Knopf and Koop, 2006, Archuleta et al., 2005). As dust normally consists of a variety of minerals, nucleation over a broad humidity range can be observed (Knopf and Koop, 2006). The freezing onset of mineral dust depends on different parameters such as aerosol size (Archuleta et al., 2005), composition (Archuleta et al., 2005) and coating with nitrates, sulfates and organics (Niedermeier et al., 2010, Murphy and Thomson, 1997, Möhler et al., 2008, Cziczo et al., 2009, Knopf and Koop, 2006). The larger the

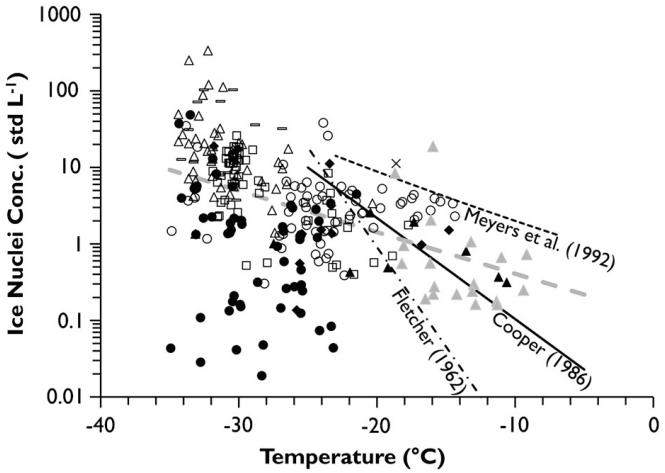

Figure 2.5.: Observed IN concentration (active at water saturation or above) in dependence on temperature. Also plotted are different parameterizations which connect the IN concentration only to temperature.
Source: DeMott, P., A. Prenni, X. Liu, S. Kreidenweis, M. Petters, C. Twohy, M. Richardson, T. Eidhammer, and D. Rogers, 2010: Predicting global atmospheric ice nuclei distributions and their impacts on climate. *Proceedings of the National Academy of Sciences of the United States of America*, 107:11217–11222, doi:10.1073/pnas.0910818107 ©Proceedings of the National Academy of Sciences. Used with permission.

aerosol is, the more active sites are incorporated at the surface and the higher is the freezing rate. On the other hand, the larger the coating thickness is, the more ineffective mineral dust becomes as IN. A pre- or deactivation of the mineral dust freezing characteristics can be observed if the aerosol particles are involved in more than one cloud formation cycle ("memory effect", Field et al. (2006), Roberts and Hallet (1968)).

Observations of IN in general show a high spatial, temporal and seasonal variability (DeMott et al., 2006). Nevertheless, the knowledge of IN active concentration in mixed-phase clouds is assumed to be crucial to predict mixed-phase cloud ice formation.
In Figure 2.5 it is shown that the average ice nuclei concentration slightly increases with decreasing temperature (dashed grey line). The figure also demonstrates that the link between IN concentration and temperature alone does not acceptably predict the IN concentration. Only recently, a parameterization is developed by DeMott et al. (2010) which connects the IN active concentration n_{IN,T_k} not only to cloud temperature T_k but also to the number concentration of aerosol particles larger than 0.5 µm in diameter $n_{aer,0}$ (Equation 2.2).

$$n_{IN,T_k} = a \cdot (273.16 - T_k)^b \cdot (n_{aer,0})^{c(273.16-T_k)+d} \tag{2.2}$$

where a = 0.0000594, b = 3.33, c = 0.0264 and d = 0.0033.
The remaining variability between DeMott et al. (2010)'s parameterization and the observed ice nuclei concentration is probably due to variations in the aerosol chemical composition.
The relatively large size of mineral dust, soil and bacterial particles in the troposphere explains the importance of aerosol particles larger than 0.5 µm. Additionally active sites on soot are commonly predicted mainly for soot diameters larger than 0.1 µm. The number of ice particles N_i is generally assumed to be linearly dependent on the number of active ice nuclei: $N_i = JN_{aer,0}$ where J is the nucleation rate.
The concept to mathematically describe heterogeneous nucleation as a "stochastic process" or as nucleation at specific particle surface sites for characteristic (deterministic) freezing temperatures ("singular approach") is still controversial (Niedermeier et al., 2011).

2.1.3. Secondary ice formation

Measurements in clouds warmer than −20 °C reveal that the number of measured ice particles sometimes exceeds the observed number of measured IN. Pruppacher and Klett (1997) state that the enhancement factor can reach 10^5 but decreases with decreasing temperature and reaches unity at −20 °C. Cantrell and Heymsfield (2005) pointed out that many processes involving ice generation are not determined in detail yet. A variety of studies exist which evaluate potential sources and mechanisms of ice production. Model studies of observed mixed-phase cloud conditions are used to narrow down the dominant effects (e.g. Fridlind et al., 2007).
The best-known ice multiplication process is the Hallet-Mossop mechanism where in the temperature interval of −3 °C and −8 °C ice splinters shed during the riming of ice crystals. Another known process is the fragmentation of large droplets during the freezing process which mainly takes place between −5 °C to −15 °C. Other known reasons for ice particle production are fragmentation of delicate crystals by mechanical influences (Pruppacher and Klett, 1997), ice-ice collisions (Takahashi et al., 1995), breakup and shedding of crystals during sublimation (Bacon et al., 1998, Oraltay and Hallett, 2005), ice nucleation on drop residuals (Beard, 1992) and circulation induced IN entrainment (Prenni et al., 2007). Zobrist et al. (2007) further demonstrated the IN potential of organics which can lead to non-homogeneous freezing of evaporating droplets (Field et al., 2001, Bigg, 1996). The contamination of in-situ instruments by shattering on the instrument inlets can be another reason for the observed enhanced ice crystal numbers (Fridlind et al., 2007). Unknown microphysical processes should not be ruled out completely either (Fridlind et al., 2007). The quantitative contributions of secondary ice formation processes for each thermodynamic situation is still unknown.

2.2. Cloud life cycle

During the life cycle of a mixed-phase cloud the number, size and phase of cloud particles change. Common processes included in cloud models are diffusional growth, condensation of water vapor, accretion of cloud water on ice particles, ice particle melting and evaporation of cloud droplets and ice crystals. Additionally, cloud particles collide and/or coalesce with each other. Also breakup of droplets and crystals due to mechanical stress occur. For more detailed information on the microphysics of each process the reader is referred to Pruppacher and Klett (1997). For atmospheric observations and model studies the cloud situation above the mixed-phase level also needs to be taken into account as seeding of high level ice crystals may occur.

Clouds containing ice crystals are accounted for producing most of the global precipitation (DeMott et al., 2010). The dominant mechanism under which cloud particles grow to precipitation sized droplets in mixed-phase clouds is the Wegener-Bergeron-Findeisen (WBF) process. It is based on the fact that below 0 °C the ice saturation pressure is lower compared to the liquid saturation pressure (compare Figure 2.2b). Ice crystals in the vicinity of water droplets grow on their expense if RH_w is less than 100 % (Korolev, 2007a). The growth of the ice crystals takes place quite rapidly. Due to their large size the ice crystals then gravitate. During their fall they pass warmer temperature regions, start to melt and eventually transform into raindrops.

The removal of ice crystals due to sedimentation is determined by the ice crystal fall speed, which greatly varies depending on the ice mass, the crystal area which is projected to the flow and the crystal dimensions (Mitchell, 1996). Additionally, the fall speed also strongly depends on pressure and temperature (Pruppacher and Klett, 1997). For more information on the relationship between ice crystal fall velocity and the particle dimensions the reader is referred to Pruppacher and Klett (1997), Mitchell (1996) or Heymsfield et al. (2002). Roughly, ice crystals being a few hundred µm in diameter exhibit fall speeds between approximately 10 cm/s and 100 cm/s (Pruppacher and Klett, 1997).

Another aspect of the mixed-phase evolution is the emerging ice crystal shape. The crystal shape is an important factor for the mixed-phase cloud radiation and precipitation budget (see Chapter 1). In general ice crystals exhibit a large variety of different shapes. Bailey and Hallet (2002, 2004) and other laboratory studies referenced in Pruppacher and Klett (1997) which are all based upon ice growth on small single ice crystals, indicate that the shape of ice crystals is dependent on their growth conditions. Temperature and relative humidity control the shape evolution. The conditions for a specific ice crystal form can be found in Pruppacher and Klett (1997) or Bailey and Hallet (2004). In general at temperatures above −10 °C the columnar character prevails. Between −10 °C and −40 °C the grown shapes are more plate-like whereas for temperatures colder than −40 °C columnar appearance again dominates. Different relative humidity regimes control the exact thickness and shape of the columnar and plate-like forms. The growth rate of each face of

an ice crystal is different and temperature dependent. Until now no microphysical theory exists which can explain this shape dependence. One approach involves the energy balance between the thermal and diffusional barrier and the barrier needed to form a new surface (Pruppacher and Klett, 1997). In fact water molecules are especially incorporated at dislocations such as steps or spirals, called active sites, which seem to be energetically favorable. Ice crystals that experience a change in temperature and/or relative humidity during their growth superimpose the shape corresponding to the new environment onto the already grown shape. Pruppacher and Klett (1997) for example show a stellar crystal onto which branches needle like structures grow. In contrast to forming ice on single crystal germs another possible way of freezing is through the liquid drop phase. Pruppacher and Klett (1997) name different authors which observed irregular shapes, bulges and intrusions after polycrystalline drop freezing.
During evaporation the ice crystals generally exhibit smoother surfaces and less edges. Pristine crystals evolve into spheroidal forms (Nelson, 1998). Within the cloud physics community the applicability of the above presented laboratory studies is still under discussion. The restricted resolution of in-situ cloud spectrometers further limits the atmospheric investigation.

2.3. Microphysical properties

Mixed-phase clouds are highly variable. The range of different microphysical parameters such as Liquid Water Path (LWP), Ice Water Path (IWP), Liquid Water Content (LWC), Ice Water Content (IWC), relative humidity RH, total drop and ice number concentration N_{tot}, mean cloud particle diameter and effective drop and ice radii are summarized in Table 2.1.

The published mixed-phase cloud properties are mainly based on observations of single-layer clouds, since multi-layered mixed-phase clouds are not in the focus of this thesis. Nevertheless, more information on multi-layered mixed-phase cloud systems can be found in Lawson et al. (2001) or Fleishauer et al. (2002).

Cober et al. (2001) report that the observed ice crystal diameters within glaciated clouds are mostly larger than 35 µm. For mainly liquid clouds and mixed-phase clouds sizes less than 30 µm dominate the size measurements. Their measurements for completely glaciated clouds furthermore reveal that the number concentration of small ice crystals is 100 to 500 times larger than the concentration of large cloud particles above 125 µm.

Although mixed-phase cloud properties are highly variable, the mixed-phase clouds often have distinct vertical structures. The largest IWC, ice crystal dimensions (larger than 200 µm) and ice particle concentrations are found in the lower part of the cloud (Hobbs and Rangno, 1985, Hobbs et al., 2001, Fleishauer et al., 2002, Pinto et al., 2001). Ice crys-

Parameter	Value	Reference
T	0 °C to −40 °C	Korolev et al. (2003)
IWP	<10 gm^{-2} to 100 gm^{-2}	Shupe and Matrosov (2006) Hobbs et al. (2001) Shupe et al. (2008)
LWP	10 gm^{-2} to 300 gm^{-2}	Shupe and Matrosov (2006) Hobbs et al. (2001) Pinto et al. (2001) Shupe et al. (2008)
IWC	0.005 gm^{-3} to 0.09 gm^{-3}	Shupe and Matrosov (2006) Pinto et al. (2001) Gultepe et al. (2000) Hobbs et al. (2001) Shupe et al. (2008)
LWC	0.01 gm^{-3} to 0.35 gm^{-3}	Fleishauer et al. (2002) Pinto et al. (2001) Hobbs et al. (2001)
RH_w	98 % to 100 %	Korolev and Isaac (2006)
$N_{tot,ice,max}$	2 cm^{-3} to 5 cm^{-3}	Korolev et al. (2003)
$N_{tot,water,max}$	250 cm^{-3} to 30 cm^{-3}	Korolev et al. (2003)
$R_{eff,ice}$	50 µm and 200 µm	Spangenberg et al. (2006) Pinto et al. (2001) Shupe et al. (2008)
$R_{eff,water}$	10 µm and 15 µm	Spangenberg et al. (2006) Korolev et al. (2003)

Table 2.1.: Ice Water Path (IWP), Liquid Water Path (LWP), Ice Water Content (IWC), Liquid Water Content (LWC) , $R_{eff,ice}$ and $R_{eff,water}$ values are based on multiple publications. The total ice and water number concentrations are averages of Korolev et al. (2003)'s extensive dataset. $N_{tot,ice,max}$ and $N_{tot,water,max}$ describe the average measured maximum ice and liquid number concentrations for −5 °C and −35 °C respectively.

tals in the upper part of single-layer clouds are rare and small (Hobbs and Rangno, 1985, Gayet et al., 2009), though low concentration of relatively large ice crystals are also found at cloud top (Gayet et al., 2009). The liquid water content, droplet size and liquid number concentration is found to increase with height (Carey et al., 2008, Fleishauer et al., 2002, Pinto et al., 2001, Pinto, 1998, Hobbs et al., 2001) with a maximum near the cloud top.

Korolev et al. (2003), Cober et al. (2001), McFarquhar and Cober (2004) indicate that ice fractions $\mu = \frac{\text{IWC}}{(\text{LWC+IWC})}$ below 0.1 and above 0.9 are observed regularly in mixed-phase clouds. Only a minority of the observed clouds show ice fractions of $0.1 < \mu < 0.9$. Thus, mixed-phase clouds are often dominated by one phase (McFarquhar and Cober, 2004). Korolev et al. (2003) concluded that "*the typical glaciation time for mixed-phase clouds is lower than the residence time of the cloud particles in the air mass*". The microphysical cloud properties depend on the ice fraction. Korolev et al. (2003) report a decreasing cloud particle concentration with increasing ice fraction, probably caused by the Wegener-Bergeron-Findeisen (WBF) process. This observation is consistent with Gayet et al. (2002), who found that during the glaciation process a transition of a large number of liquid droplets to a smaller number of larger aspherical ice crystals takes place, i.e. that the amount of cloud droplets and ice crystals may change over the cloud lifetime. Glaciation times are discussed in Section 2.4.

Another important factor is the temperature dependence of the mixed-phase microphysical properties. Korolev et al. (2003) found that the ice, liquid and total water contents are in general decreasing functions of temperature. For completely liquid clouds the liquid water content (LWC) decreases from 0.16 gm^{-3} at −5 °C to 0.08 gm^{-3} at −35 °C and for completely glaciated clouds the ice water content (IWC) decreases from 0.1 gm^{-3} at −5 °C to 0.02 gm^{-3} at −35 °C. On the contrary, Fleishauer et al. (2002) reported no obvious dependence between ice water content (IWC) and temperature but rather observed a maximum between −8 °C to −20 °C where the difference of ice and water saturation pressure is largest. For the ice fraction, Korolev et al. (2003) found an increase with decreasing temperature whereas the liquid fraction decreased with temperature. Accordingly, the droplet number concentration for mostly liquid clouds declines with decreasing temperature from 200 cm^{-3} at −5 °C to 30 cm^{-3} at −35 °C (Table 2.1, Korolev et al., 2003). No obvious total number concentration temperature dependence is evident for mostly glaciated clouds ($N \approx 2$ cm^{-3} to 6 cm^{-3}), though. The ice and droplet concentrations of clouds containing both water and ice crystals are limited by the glaciated and liquid case for each temperature interval.

The average volume diameter of liquid cloud droplets slightly increases with decreasing temperature from 12 µm at 0 °C to 18 µm at −35 °C (Korolev et al., 2003, Shupe and Matrosov, 2006). The mean volume diameter of ice crystals on the other hand shows a maximum of approximately 40 µm between −15 °C and −10 °C. However, this analysis considerd only cloud particles with sizes up to 100 µm. Including all clouds observed in the temperature interval 0 °C to −40 °C the mean cloud volume diameter has a similar temperature dependence as liquid clouds but with slightly higher values between 15 µm to 20 µm.

As demonstrated above, the knowledge of the mixed-phase cloud microphysical properties greatly improved within the last decade. But the overall formation and development of mixed-phase clouds is still poorly understood. Some of the key questions and concerns are: How do instrument limitations affect the mixed-phase cloud research? How reliable are the measured total number concentrations? How does shattering on the instrument edges affect the measurements? How is the exact morphology of the ice crystals and how can these be assessed? "*What is the spatial scale of mixing between liquid and ice, and how does it vary with height, meteorological conditions, etc.? For mixed-phase clouds, how are the liquid and ice partitioned with respect to particle sizes (e.g., are all small particles liquid and all large particles ice)?*" How ... "*to distinguish small ice particles from high concentrations of supercooled droplets*"? What "*concentrations of small ice particles* (are present) *in mixed-phase clouds?*" (McFarquhar et al., 2010)

2.4. Dynamic impact

Mixed-phase cloud observations especially over the arctic are reported frequently (Shupe and Matrosov (2006),Korolev et al. (2003)). From a dynamic point of view, the coexistence of multiple phases over an extended period of time is unstable. Thus, mixed-phase cloud evolution is commonly associated with the Wegener-Bergeron-Findeisen (WBF) process (references in Korolev and Isaac, 2003a, see also Section 2.2).
Korolev and Isaac (2003a) estimate glaciation times between 20 min to 40 min for ice crystal concentrations of $10^2 - 10^3$ l^{-1} and liquid water contents below 0.5 gm^{-3} which are commonly observed in mixed-phase clouds (Section 2.3). The glaciation time increases for lower ice crystal concentrations but typically does not exceed a few hours. However, mixed-phase clouds are observed which persisted in a quasi steady state for long periods of time (Shupe and Matrosov, 2006). The partitioning of liquid droplets and ice crystals on small spatial scales in these clouds is unknown. If they are assumed to coexist within the same cloud sub volume for a long time period, then the question remains what mechanism does exist to stabilize the system? On the other hand, if they are spatially separated within the cloud, how can such a layering be produced?
To explain the coexistence between ice crystals and liquid droplets Harrington et al. (1999) and Rauber and Tokay (1991) suggest an approach which is based upon the balance between the condensation rate of liquid droplets, the ice crystal precipitation rate and the ice crystal growth rate. The liquid water formation is assumed to exceed the ice formation in the updraft region of the cloud. Nevertheless, once ice crystals are formed, the WBF process is assumed to take place and the ice crystals grow fast on the expense of the surrounding water droplets. Due to their size the ice crystals then sediment down. The resulting mixed-phase cloud system is stable.
Korolev and Isaac (2003a) and Korolev and Field (2008) on the other hand indicate that the vertical velocity of the atmospheric system affects the mixed-phase cloud stability. In

general, the vertical velocity influences the cooling rate of the air parcel and thus also affects the relative humidity, cloud particle growth behavior and glaciation time. Korolev and Field (2008) simulated uplifting clouds and found that for uniform updraft a mixed-phase mid-level layer can be established. Furthermore assuming harmonic or turbulent motions result in two layered cloud systems. The lower half of the cloud system consists of ice crystals whereas the upper half contains ice crystals and liquid droplets. For turbulent motion the upper layer is patchy with alternating mixed-phase and only ice parts. The simulations match the observations of mostly liquid layers at the top of single layer mixed-phase clouds (Section 2.3). To establish coexistent liquid and ice regions, the vertical velocity must exceed a certain threshold and the cloud system a certain height as defined in Korolev and Field (2008). The threshold updraft velocity which is required to initiate the evolution of multiple phases is a function of the integral radius of ice $N_i\bar{r}_i$ (Korolev and Mazin, 2003). This is due to the fact that specific humidity conditions are required for liquid droplet and ice crystal coexistence (see Equation 2.4). The relative humidity in turn is influenced by updraft velocity and ice crystal and liquid droplet concentration and size (see Equations 2.6 and 2.7).

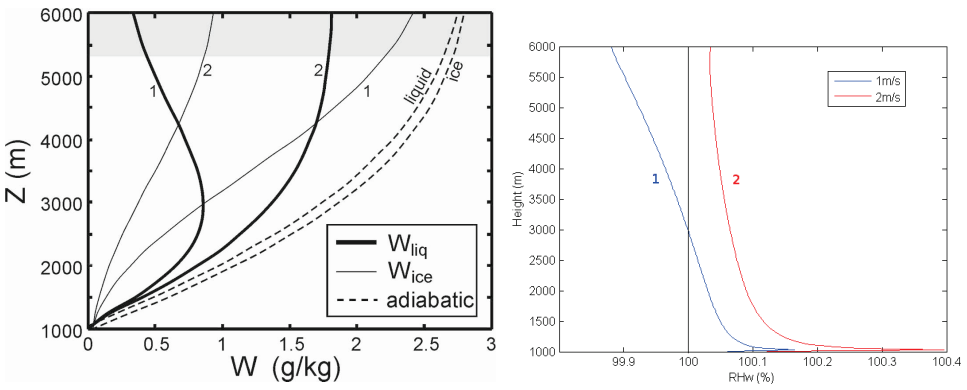

Figure 2.6.: a) Modeled liquid water content W_{liq} and ice water content W_{ice} for two clouds uplifted at $u_z = 1$ ms^{-1} (labeled 1) and $u_z = 2$ ms^{-1} (labeled 1). Initial cloud microphysics: ice crystal concentration $N_i = 100$ L^{-1}, ice radii $r_{io} = 50$ μ m, supersaturation $S_{i0} = 0$ and temperature $T_0 = -5$ °C.
Source: Korolev, A., 2007a: Limitations of the Wegner-Bergeron-Findeisen mechanism in the evolution of mixed-phase clouds. *Journal of the Atmospheric Sciences*, 64:3372–3375, doi:10.1175/JAS4035.1 ©American Meteorological Society. Used with permission.
b) Simulated relative humidity with respect to water RH_w.
Source: Korolev, A., 2011: personal communication ©A. Korolev. Used with permission.

To explain regions of liquid and/or ice growth, Korolev (2007a) focuses on the relative humidity regimes rather than the updraft velocity. Three thermodynamic situations are identified in mixed-phase clouds:

$$\mathrm{RH_w} < 100\% \qquad e_w > e > e_i \qquad \mathrm{RH_i} > 100\% \tag{2.3}$$
$$\mathrm{RH_w} > 100\% \qquad e_w > e_i > e \qquad \mathrm{RH_i} > 100\% \tag{2.4}$$
$$\mathrm{RH_w} < 100\% \qquad e > e_w > e_i \qquad \mathrm{RH_i} < 100\% \tag{2.5}$$

If the cloud is exposed to WBF-conditions (Equation 2.3 and Section 2.2), droplets evaporate while the ice crystals grow, since the air is subsaturated with respect to water but supersaturated with respect to ice. In case $\mathrm{RH_w}$ and $\mathrm{RH_i}$ are both supersaturated (Equation 2.4), droplets and ice crystals can coexist and grow simultaneously. On the other hand, both ice crystals and liquid droplets evaporate if $\mathrm{RH_w}$ and $\mathrm{RH_i}$ fall below saturation (Equation 2.5).

To assess the evolution of the microphysical properties of clouds exposed to the different thermodynamic situations, Korolev (2007a) simulated an uplifting cloud, but allowing the cloud to rise at different speeds. Their results are illustrated in Figure 2.6. A smaller updraft velocity $\mathrm{u_{z,1}}$ cause the WBF process to occur when $\mathrm{RH_w}$ (line 1 in Figure 2.6b) becomes subsaturated. For the lower part of cloud 1 (below 3000 m) both liquid and ice particles grow. Above the threshold level the ice water content $\mathrm{W_{ice}}$ = IWC increases whereas the liquid droplets evaporate, which can be seen from the decrease in the liquid water content $\mathrm{W_{liq}}$ = LWC.

For cloud 2 a higher vertical velocity is assumed, which leads to a supersaturated environment with respect to both water and ice (line 2 in Figure 2.6b) at all heights. Thus a simultaneous growth of liquid droplets and ice crystals takes place at all levels. Remarkable differences in the modeled $\mathrm{W_{liq}}$ and $\mathrm{W_{ice}}$ are obvious from Figure 2.6a for the two clouds. $\mathrm{W_{liq}}$ of cloud 1, uplifted with a small vertical velocity and thus in the WBF regime, is lower than for cloud 2 which develops under coexistence conditions. The difference is largest at cloud top where the size and concentration of the liquid droplets of cloud 1 decreases due to the subsaturated environment with respect to liquid. On the contrary, the modeled $\mathrm{W_{ice}}$ is higher for cloud 1 than for cloud 2 for all heights. The difference increases with height due to the increased glaciation of the cloud. Although Korolev (2007a)'s simulations are simplified and neglect processes such as sedimentation or aggregation, they clearly show the completely different microphysical development of mixed-phased clouds in the WBF in comparison to the coexistence regime.

In a recent model study, Ervens et al. (2011) performed sensitivity studies to identify the dominant effects influencing the liquid and ice partitioning in mixed-phase clouds. The cloud glaciation is examined in dependence on IN concentration and nucleation mode, ice particle shape, properties of CCN and IN and updraft velocity. They found coexistent droplet and ic growth for most of the selected conditions which are chosen based on observations made during two field campaigns (SHEBA and MPACE). Evaporation of liquid

droplets and simultaneous growth of ice crystals is initiated in low updrafts (WBF conditions). Thus, the sensitivity studies by Ervens et al. (2011) support Korolev (2007a)'s suggestion that the updraft velocity, and thus RH_w and RH_i, plays a key role in liquid and ice partitioning. But, Ervens et al. (2011) also show that the degree of glaciation in mixed-phase clouds is also driven by the number of IN, simply because to some extent the ice crystal concentration is controlled by the IN number.

In general, the mixed-phase cloud glaciation during the equilibrium phase is influenced by IN active aerosol, thermodynamic conditions and updraft velocity during the cloud formation period. The IN define the onset of ice formation as well as the initial number of ice crystals. The ice crystal formation and the updraft velocity on the other hand then further influences the relative humidity conditions:

$$\Delta RH = \Delta RH_{cooling} - \Delta RH_{growth} \tag{2.6}$$

$$\Delta RH_{growth} = \Delta RH_{ice} + \Delta RH_{liquid} \tag{2.7}$$

where ΔRH is the total change of the relative humidity (with respect to liquid and ice), $\Delta RH_{cooling}$ is the change caused by the uplifting of the air parcel, ΔRH_{growth} is the change in relative humidity due to ice crystal (ΔRH_{ice}) and liquid droplet (ΔRH_{liquid}) growth or evaporation.
In case of strong cooling, $\Delta RH_{cooling}$ strongly increases. ΔRH_{growth} is not large enough to decrease RH_w below 100 %. Resultantly, both liquid droplets and ice crystals can coexist. If the uplift is smaller, the increase of $\Delta RH_{cooling}$ is slower. Then, ΔRH_{growth} is large enough to decrease RH_w into the subsaturated liquid WBF regime, which in result leads to ice growth and droplet evaporation.

Up to now, it is unclear which processes dominate the evolution of the ice phase within mixed-phase clouds. Do the concentration and composition of CCN and IN dominate the glaciation mechanism or do the dynamic effects dominate? Especially instrumental issues limit the mixed-phase cloud research. Until now, mainly the bulk IWC and LWC are used to assess the glaciation process within mixed-phase clouds (Korolev et al., 2003). Thus, size segregated experimental mixed-phase cloud observations are required. This thesis is designed to help identifying the processes controlling the liquid and ice partitioning. The experimental approach is outlined in the next section.

2.5. Objectives of this study

This thesis concentrates on the analysis of size resolved microphysical properties in mixed-phase clouds. Motivated by the challenging open questions discussed in the last section, the following key questions of mixed-phase cloud research are assessed:

What measurement technique is suitable to investigate the distribution of water droplets and ice crystals within mixed-phase clouds? How reliable is this measurement technique?

In this study, measurements are performed with an established in-situ cloud particle spectrometer (see Chapter 3), which is equipped with a newly developed polarization measurement technique to simultaneously detect aspherical ice crystals and spherical water droplets.

In which thermodynamic situations can mixed-phase clouds generally persist and how do the corresponding water and ice microphysical properties evolve?

The thermodynamically possible scenarios presented in Section 2.4 question the assumption that the mixed-phase cloud glaciation is exclusively controlled by the Wegner-Bergeron-Findeisen process. In this thesis, thermodynamic situations for coexistence of liquid droplet and ice crystals as well as Wegener-Bergeron-Findeisen situations are investigated. Therefore, mixed-phase clouds are generated in the AIDA cloud chamber under controlled temperature and humidity conditions and the evolution of the microphysical cloud properties is studied. Of special interest is the liquid and ice partitioning with respect to cloud particle size. The advantage of artificially produced clouds is that their time evolution can be studied in a well defined and unperturbed environment.

Are all possible mixed-phase thermodynamic situations really observed in natural clouds?

The observed artificial cloud situations are not necessarily transferable to natural clouds. Similarities and differences to natural clouds are assessed and possible causes for differences are discussed. To this end, airborne measurements in mixed-phase stratocumulus clouds are performed on board of the British BAE146 during the campaign Combined Observation of the Atmospheric boundary Layer to study the Evolution of StratoCumulus (COALESC) over the United Kingdom (UK).

How do the microphysical properties of mixed-phase clouds vary with temperature?

To represent mixed-phase cloud properties in climate models, the temperature dependence of their microphysical properties has to be known. To establish the largest possible variety of different initial conditions, the size and concentration of liquid droplets and ice particles is evaluated at the AIDA chamber in the temperature range of 0 °C and −40 °C.

3. Instrumentation: The new cloud spectrometer NIXE-CAPS

The new Jülich cloud particle spectrometer NIXE-CAPS is established at the IEK-7 in the frame of this thesis. NIXE-CAPS[1] (see Baumgardner et al., 2001) is a combination probe where two different techniques are combined into one single instrument. The subsystems of NIXE-CAPS are the Novel Ice EXpEriment - Cloud and Aerosol Spectrometer (NIXE-CAS) and the Novel Ice EXpEriment - Cloud Imaging Probe (NIXE-CIP):

$$\text{NIXE-CAPS} = \text{NIXE-CAS} + \text{NIXE-CIP}$$

NIXE-CAS measures the size and, for the first time, the asphericity of every single aerosol particle, water droplet and ice crystal in the size range of 0.61 µm and 50 µm. NIXE-CIP on the other hand detects the particle size and number between 15 µm and 945 µm.
This type of instrumentation was operated for the first time by the cloud group of the IEK-7. Therefore, one major task accomplished if this thesis is the development of a comprehensive data analysis procedure. The software that is provided by the NIXE-CAPS manufacturers is only designed to record and display the raw data. For the analysis presented here, the NIXE-CAPS dataset needs more extensive processing, especially to obtain information about the shape of the cloud particles. In addition, the NIXE-CAPS output is converted into other well-established quantities such as number size distributions of liquid and ice particles. Finally, the evaluation of the measurement quality and the reduction of the instruments uncertainties is discussed. In the following sections the NIXE-CAPS measurement and analysis techniques are introduced.

3.1. The CAS-Depol

The NIXE-CAS employs light scattering by aerosol particles, water droplets and ice crystals to deduce the particle size (Droplet Measurement Technologies, 2009). Furthermore, each scattering event is counted. As a new feature, measurements of the polarization state of the laser light are used to distinguish between spherical and aspherical particles. Thus,

[1] manufactured by DMT, Boulder, CO, USA

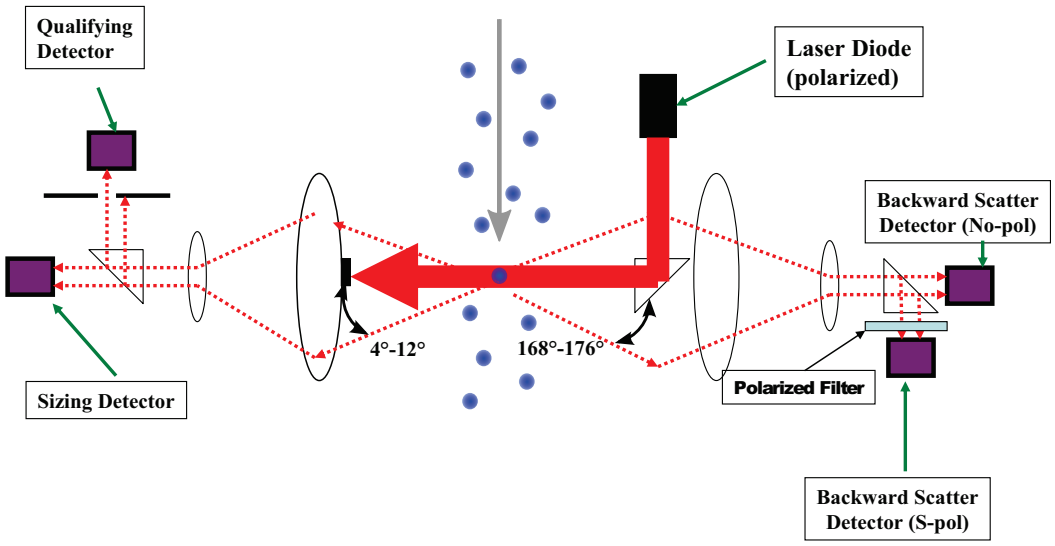

Figure 3.1.: Schematic of the Novel Ice EXpEriment - Cloud and Aerosol Spectrometer (NIXE-CAS) optical setup. Source: Droplet Measurement Technologies (2009)

it is possible to detect the size and number of small cloud droplets and ice crystals on a single particle basis. The following sections give an overview over the optical setup, the theory linking the intensity of scattered light to the particle size as well as the measurement limitations and uncertainties. In particular the new polarization technique is presented and discussed in detail.

3.1.1. Electro-optical design

In Figure 3.1 the optical setup of the NIXE-CAS instrument is shown. A 680 nm linearly polarized laser beam illuminates a stream of sample air. Two transparent windows separate the optical setup from the air stream. The focus of the laser beam is 150 µm wide and located in the middle of two scattering collecting lenses. The aerosol particles, cloud droplets and ice crystals contained in the sample air scatter the laser light. The scattered light is detected in forward direction from 4° to 12° and in backward direction from 168° to 174° by circular detectors. A dump spot and the forward collecting lens limit the angle in forward direction whereas the backward collecting lens defines the backward angle.
To size the particles the intensity of the scattered light in forward direction is measured. Simultaneously, the scattering events are counted. To avoid false sizing due to scattering from low intensity regions of the Gaussian-distributed laser beam, the most intense portion of the beam, the so called Sample Area (SA), is selected. The SA is defined by its length

along the laser beam called Depth Of Field (DOF) and the width of the beam perpendicular to the DOF and the air flow called Effective Beam Diameter (EBD). The center of the DOF is the Center Of Focus (COF) of the instruments lens system. A particle in the center of focus is exactly imaged in the exact forward direction. On the other hand, if it passes the laser beam away from the center of focus (COF), then its image appears larger but its intensity is lower. To narrow the sample area (SA) down to the 10 % to 15 % highest intensity region of the laser beam, 66 % of the forward scattered light is directed onto a qualifying detector while 33 % of the forward scattered light is focused onto a sizing detector by a beam splitting element. The qualifying detector is masked by a 200 µm x 1200 µm rectangular slid. Particles which cause a larger scattering signal at the qualifying detector than the sizing detector are counted and sized. This ensures that only particles are accepted which pass the laser beam near the center of focus. The sample area is measured and modeled to be 1.5 mm x 0.15 mm. The three dimensional Sample Volume (SV) is given by Equation 3.1.

$$\mathrm{SV} = \mathrm{SA} \cdot \mathrm{v} \cdot \mathrm{t} \tag{3.1}$$

where v is the airspeed and t the sampling time.

Two detectors in the backward direction measure the light scattered between 168° to 174°. Reflections of the non-scattered incident laser light into the back hemisphere are avoided by the use of a dump spot. A prism separates the backscattered light into two equal portions. One detector measures the total backscattered light whereas another detector is equipped with a polarization filter to detect the polarized component perpendicular to the incident laser polarization.

An extensive electronic system exists to process the raw measured intensities, to sort the intensities into size bins and to transfer the data to an externally connected computer. The Particle Analysis and Display System (PADS) software communicates with the instruments internal electronic system and saves incoming data and displays the raw data in real time. The measured intensities are amplified and digitized in different stages to better resolve the size regions of interest. The scattered intensity is thus internally converted into an analog to digital (A/D) value, from here on called A/D count. The A/D values can range from 0 to 12287. More information on the A/D counts are given in Appendix A.3.1. For the forward scattered light three different gain stages exist, where each is applied depending on the forward scattered intensity. For the perpendicular polarized component of the backscattered intensity only one gain is applied, whereas for the total backward scattered light two gain stages exist.

3.1.2. Data storage

In total two different data files exist. One includes all housekeeping, meteorological and particle frequency distribution data for one second intervals. In the other file, called Particle by Particle (PBP), the single particle intensities as well as InterArrival Time (IAT) and times of occurrence for each single particle are stored. The scattering information of a maximum of 512 particles can be stored within the PBP file between two readouts of the internal NIXE-CAS memory. The NIXE-CAS data is classified into four categories: the housekeeping, the particle frequency histogram, the basic meteorological and the particle by particle measurements. The housekeeping data covers temperature measurements at different locations of the instrument, laser current and voltage as well as the noise thresholds for the different gain stages. Pressure, temperature, relative humidity and airspeed measurements fall into the meteorological category. For the particle frequency histogram 30 intensity thresholds are predefined. As explained later, these intensity thresholds can unambiguously be converted into size thresholds. Depending on the forward scattered light of each particle the number of particles measured in the corresponding channel is counted. Thus a frequency histogram with the number of particles per intensity bin is recorded. In the PBP file, the peak intensity amplitudes converted to A/D counts for the forward, backward and polarized detectors are stored. Additionally, the interarrival time (IAT) between two successive particle scattering events is recorded there. The frequency histogram measurements also include distributions of the interarrival time (IAT) per second.

3.1.3. Particle size determination

The concept of the NIXE-CAS particle size measurement is based on the Mie scattering theory for spherical particles. The theoretical background of single particle scattering is given in Appendix A.3.2.
The NIXE-CAS particle size is determined by relating the intensity scattered into at a specific angle in forward direction to the incident intensity of the laser beam:

$$I_s = E_{\parallel s} E^*_{\parallel s} + E_{\perp s} E^*_{\perp s} = \frac{\sigma_i}{{r_d}^2} I_i \tag{3.2}$$

I_s is the measured intensity at the detector position, $E_{\parallel i}$ and $E_{\perp i}$ are the scattered and incident parallel and perpendicular electrical field components, σ_i is the differential scattering cross section and r_d is the radial distance between particle origin and observer (Thomas (2003)).
NIXE-CAS does not directly measure σ_i but the detectors and the electronic amplification system output A/D counts (see Section 3.1.1) that are related to the measured intensity. The relation between σ_i and the A/D counts is determined by calibration using particles of known size.
The differential scattering cross section σ_i is to a first approximation independent of the

particle shape when the light is scattered into the forward direction. If the refractive index of the particles is constant, the forward scattering cross section $\sigma_{i,f}$ is to a first approximation only dependent on the particle size.
The particle size can then be related to the scattering cross section $\sigma_{i,f}$ by Mie theory. For this purpose, a look-up table or graph is generated which contains the differential scattering cross sections calculated by Mie theory for various particle sizes and refractive indexes. Figure 3.2a displays the Mie curves for the NIXE-CAS setup for particles between 0.5 µm and 50 µm in diameter. The green line represents particles with refractive index of 1.51 (glass) whereas the blue line represents calculations for particles with refractive index of 1.33 (water).

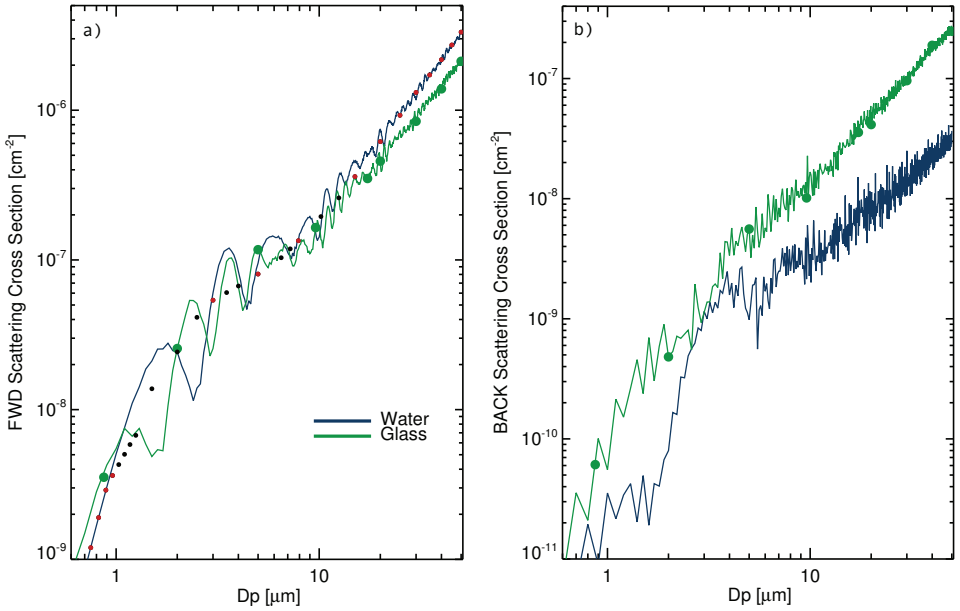

Figure 3.2.: Illustration of calculated differential scattering cross sections for a variety of differently sized spherical particles consisting of water (refractive index of n = 1.33, blue curve) or glass (refractive index of n = 1.51, green curve). a) Scattering into the NIXE-CAS forward direction and b) scattering into the NIXE-CAS backward direction. The calculations are based on the Mie theory. The green points indicate the glass bead sizes used for calibration of the NIXE-CAS instrument. The black dots indicate the instrument thresholds in which the single particles are classified and the red dots indicate the merged size thresholds.

To convert the measured A/D counts to differential scattering cross sections σ_i, the system must be calibrated. For the calibration mono dispersed glass beads and latex beads are used. The glass beads are available in the size range between 5 µm and 50 µm with a size deviation smaller than 5 % whereas the latex particles range between 0.61 µm and

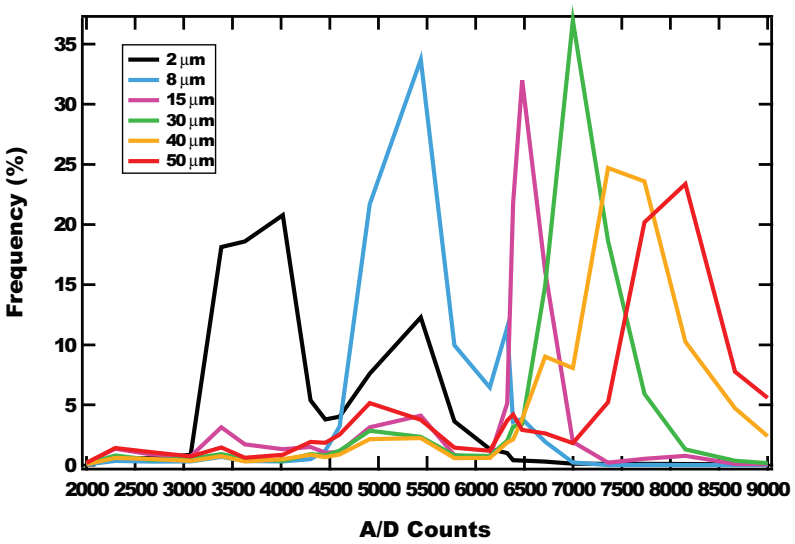

Figure 3.3.: Frequency histogram which demonstrates the range of A/D counts measured by NIXE-CAS for different mono dispersed glass beads used for calibration. The different glass bead sizes are indicated by color. The A/D counts at peak value are used to calculate the detector scale factor. Source: Baumgardner (2011)

2 µm with less than 5 % size deviation. The glass beads are disposed into air which is then guided through the NIXE-CAS sample volume. In contrast, the latex particles are only available as aqueous solution. Thus a spray of these particles needs to be dried prior to directing it through the NIXE-CAS sample volume. The measured A/D count distributions for different streams of mono dispersed glass and latex particles are shown in Figure 3.3. For the calibration the peak of the frequency distribution is selected. The relation between peak A/D count C_i and differential forward scattering cross section $\sigma_{i,f}$ is linear. The calibration constant S_i is defined by:

$$S_i = \frac{C_i}{\sigma_{i,f}} \tag{3.3}$$

Thus, for each calibrated particle size a linear calibration coefficient S_i is determined. The forward scattering cross section $\sigma_{i,f}$ for each particle size and refractive index is given in Figure 3.2a. For a single amplification system each calibration coefficient would be equal: $S_1 = ... = S_n$. But since the NIXE-CAS electronics for the forward intensity measurements consist of three gain stages, calibration particles for each gain interval need to be used to determine the calibration coefficient for each gain stage. The refractive index of the used glass beads is 1.51. The refractive index of measured atmospheric spherical ice crystals is 1.31 and for cloud droplets 1.33. Thus, if the calibration constants are known, atmospheric

particles of unknown size can be sampled and the scattered intensity of each particle can be calculated. To identify the particle size, the theoretical scattering cross section for refractive index 1.33 in Figure 3.2a is used for liquid droplets.

The curve defined by the calibration particles (green dots) in Figure 3.2a reveal one measurement limitation of this technique. The points form a smooth, monotonically increasing function. Ambiguities evident for the theoretical calculated curves (i.a. green line) are not resolved. Two unknown particles of different size may produce the same measured scattering cross section. They are assigned to the same size and one particle may thus be falsely sized. To minimize this uncertainty, size intervals are defined so that sizes representing the same scattering cross section are sorted into the same size interval. The method of size combination is exemplified in Figure 3.5 where the black dots represent the middle of each bin and the black vertical lines intersecting the black bar indicate the bin boundaries. The width and location of each size interval is dependent on the particles refractive index n as the oscillating behavior of the Mie curves change with n (compare green and black curve in Figure 3.2a).

Another limitation of the measurement technique is the assumed independence of the differential scattering cross section $\sigma_{\mathrm{i,f}}$ from the particle shape in forward direction. This uncertainty can be reduced by performing theoretical calculations for aspherical particles (ice crystals) to relate the differential scattering cross section $\sigma_{\mathrm{i,f}}$ to the particle size and shape. For small aspherical particles, T-matrix calculations and for larger aspherical particles geometrical optic calculations can be used to evaluate the scattering behavior for the instrument configuration.
T-matrix calculations are extensively discussed by Mishchenko et al. (2000) or Mishchenko et al. (2005). Similar to the Mie theory, the incident and scattered fields are expanded into vector spherical harmonics. The expansion coefficients of the incident and scattered fields are then related by a transition matrix $\mathbb{T}$. The so called T-matrix is determined in the particle reference system and is calculated by the use of the Huygens principle. To calculate the T-matrix the particle size, shape and refractive index is needed.
The geometrical optic approximation (Mishchenko et al., 2000, 2005) is based on the assumption that each incident plane wave can be separated into a collection of independent parallel rays. These rays are then traced by using Snells law and the Fresnel equations on the particle surface. Also Frauenhofer diffraction needs to be taken into account for the forward scattering direction. The rays are then evaluated in narrow angular ranges.

Figure 3.4 shows the calculated differential cross sections σ_{i} in forward direction for aspherical prolate particles with aspect ratios 0.5 and 0.75 for the NIXE-CAS optical setup and a particle refractive index of 1.31 (ice). For comparison the corresponding Mie curve (a/b = 1) for the refractive index of 1.33 (water) is included in red. The red points indicate the differential scattering cross sections, calculated with Mie theory, which correspond to predefined particle size thresholds. The thresholds (also compare Figure 3.5) are chosen to guarantee minimal particle sizing ambiguities. The blue and green points indicate the

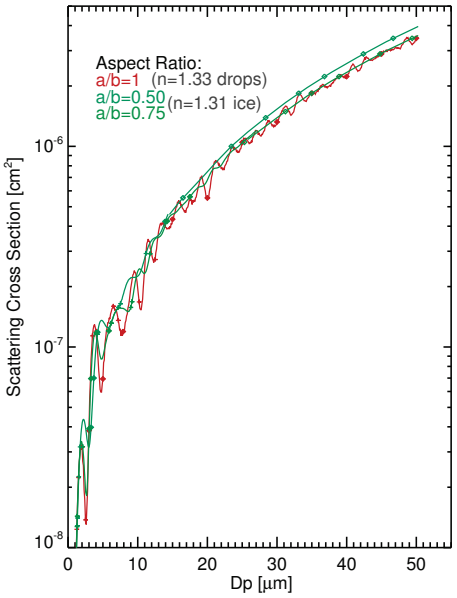

Figure 3.4.: Same as Figure 3.2 but the differential scattering cross sections for prolate ice spheroids (refractive index of n = 1.31) are theoretically calculated on the basis of T-matrix and geometric optics theory. Again the optical setup of the NIXE-CAS instrument is simulated and the Mie curve is plotted for comparison purposes. The colors indicate two different particle aspect ratios a/b = 0.5 and a/b = 0.75.
The data is based upon algorithms developed by M.I. Mishchenko, A.Macke and P.Yang. The calculations are provided by Garsteiger, J., 2011: personal communication

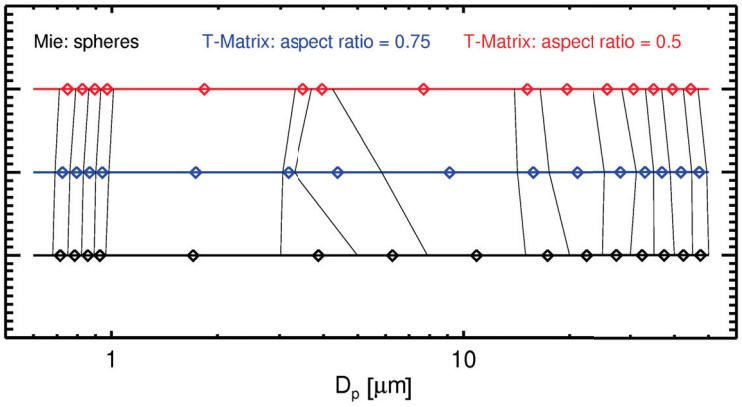

Figure 3.5.: CAS size bins as determined by the different theories for scattering on spherical (black) and aspherical (red and blue) cloud particles (compare Figures 3.2 and 3.4). The dots indicate the middle of each bin and the vertical black lines define the bin boundaries.

corresponding size thresholds for spheroidal particles with aspect ratios of 0.5 and 0.75 which result in almost the same differential scattering cross sections. The shift of the size channels from spherical to aspherical particles is mostly below 10 % (see Figure 3.5). The deviation is highest for the intermediate size range between 1 µm and 10 µm. When aspherical ice crystals are sampled, the modified size thresholds are used. The aspect ratio which is used for the calculation of the differential scattering cross section is decided from case to case. For mixed-phase clouds 0.75 appears to be a reasonable value according to Korolev and Isaac (2003b). Note here that with the new feature to measure the polarized component of the backscattered light for each particle (see Section 3.1.4), it is not only possible to distinguish for the first time between liquid droplets and ice crystals but also to apply the correct curve of scattering cross section versus size to sort the particles in the right size interval.

Alternatively, also the scattering in backward direction could be used to measure the particle size. Within the NIXE-CAS instrument a detector covering the angular range of 168° to 176° is installed. The backward differential cross section can be modeled with Mie theory and is displayed in Figure 3.2b. The calibration of the backward A/D counts, which the detector and amplification system output, to the equivalent backward differential scattering cross section is performed equivalently as for the forward direction. The amplification system of the detector measuring the total backscattered light consists of two gain stages. Thus two linear calibration constants need to be determined. In this thesis, the size determination from the measurements of the intensity scattered into the backward direction is not used, because the light scattered into the backward hemisphere is more sensitive to the shape of the particles than the light scattered into the forward hemisphere.

3.1.4. Particle shape determination

With the new detector implementation of the NIXE-CAS to measure the intensity of the polarized components of the backscattered light the asphericity of the particles can be deduced in addition to the particle size. Thus, a distinction between spherical water droplets and aspherical ice particles is for the first time possible with this type of instrumentation. A theoretical background on scattering and polarization as well as a more extensive illustration of the here presented algorithm to identify liquid droplets and ice crystals is given in Appendix A.3.3. For the detection of the particles asphericity, the polarized components of the scattered light are usually measured in backward direction because the scattering in that direction is influenced by the particle shape. For the NIXE-CAS setup, the initial laser light is polarized linearly and the scattered cross-polarized component, which is the perpendicularly polarized component to the polarization state of the incident laser light, is detected. Furthermore the total backscattered light is recorded.

But why does the polarization state of light scattered by aspherical particles differ from that scattered by spherical particles? Aspherical particles that scatter light alter the po-

larization state due to internal reflections of the light on the particle lattice. Furthermore, electric dipoles are induced within the particle when it is exposed to external electric fields. Bends and edges in the particle surface can influence the strength and orientation of the electric dipoles and thus alter the state of polarization of the re-emitted light waves.

For the NIXE-CAS experimental setup, water droplets do not strongly alter the polarization state of the incident light or in other words depolarize the light (compare Appendix A.3.3). Theoretical calculations for aspherical particles of a specific form however predict a wide variety of different polarization values depending on the size and orientation of the sampled ice crystals (Nicolet et al. (2007), Sassen and Hsueh (1998), Freudenthaler et al. (1996) and Appendix A.3.3). This theoretical knowledge is used as a starting point to develop a new cloud phase detection algorithm.
As already mentioned, the NIXE-CAS measures the intensities of the cross polarized components of the backscattered light compared to the incident laser polarization. The raw output, however, are not differential scattering cross sections but A/D counts (see Section 3.1.1), which are hereafter called cross polarized A/D counts. For the separation of water droplets and ice crystals, a cloud of water droplets is used as reference. For spherical cloud particles it is expected that the measured cross-polarized component is small. Because the cross polarized backscattered intensity is predicted to be sensitive to the particle size, the total forward scattered intensity is also taken into account.
Figure 3.6a displays the cross polarized A/D counts versus size frequency distribution of a

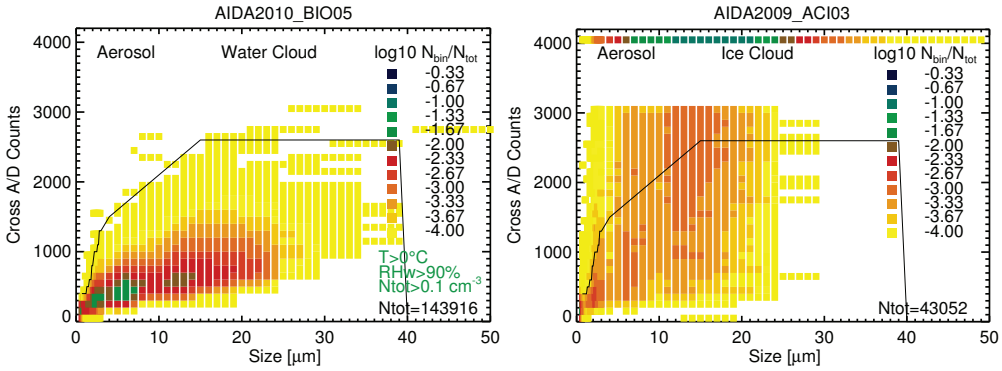

Figure 3.6.: Frequency histograms of particle sizes vs A/D counts of the cross polarized backscattered light component for a) a liquid and b) a pure ice cloud generated during the BIO05 experiment 10 and ACI03 experiment 22. The black line represents the threshold line to distinguish spherical and aspherical particles.

pure water cloud obtained during the AIDA measurement period BIO05 (see Table A.1). It is evident that the cross polarized A/D counts are size dependent. The larger the particles, the larger are the measured A/D counts. To distinguish water droplets and ice crystals, a threshold line is defined which is unique for the optical configuration of the NIXE-CAS. All

points situated below the threshold lines are classified as spherical, all above as aspherical. The above described method is not only applicable to measurements of liquid droplets and ice crystals, but also to the aerosol mode measured by NIXE-CAS. In this mode, condensed aerosol particles are distinguished from dry highly aspherical aerosol particles.
In comparison to pure water clouds, Figure 3.6b displays the cross polarized A/D counts vs size for an ice cloud formed below −38 °C (AIDA measurement period ACI03, see Table A.1). The threshold line to separate ice crystals from liquid droplets is plotted in black. At this temperature, droplets no longer exist, so that the cloud can clearly be identified to consist of only ice particles. A number of particles are detected at the cross polarized backscattered saturation threshold of the NIXE-CAS amplification system. The particles cause a cross polarization signal which is larger than the maximum value of the amplification system and thus their signals are set to the saturation value of 4095. In Figure 3.6b the saturated counts are aligned along the horizontal line at 4095 cross polarized counts. All particles with counts between the threshold (black line) and the saturation line and all particles at the saturation line are classified as ice particles. Thus in ice clouds, some fraction of the cloud particles especially those of smaller size which are located below the threshold line are not unambiguously classified as ice particles.
Figure 3.7 shows a time series of cloud microphysical measurements obtained during the AIDA-HALO02 experiment 4. Panel c in particular displays the time evolution of the NIXE-CAS size resolved aspherical particle fractions. The size is indicated on the ordinate and the color code describes the fraction of aspherical particles per size interval and time step. The aspherical fraction is determined on the basis of the algorithm described in this section. Taking into account the total number concentration measured by NIXE-CAS, the ice and liquid total number concentrations (Figure 3.7b) can be deduced. Between the two vertical blue lines in Figure 3.7 the evolution of a liquid cloud is displayed (compare Figure 3.17 and Section 3.5). At 400 s the evaporation of cloud droplets and the onset of ice formation takes place (light blue vertical line in Figure 3.7 and 3.17). A pure ice cloud evolves. From that point on the cloud is completely glaciated, since the temperature decreases to around −38 °C which is the temperature of spontaneous homogeneous freezing of liquid droplets. The NIXE-CAS aspherical fractions and ice number concentrations measured for the ice cloud section in Figure 3.7b point out a large percentage of ice crystals. Nevertheless, a small amount of particles with sizes below 10 µm are detected as liquid droplets instead of ice crystals (Figure 3.7c). That is because their signal is below the threshold line shown in Figure 3.6. For the ice cloud section the measured total aspherical particle fraction is around 90 %. Thus, up to 10 % of the measured cloud particles are detected as liquid droplets. It is unlikely that the small cloud particles which are classified as liquid really inhibit that phase. Another possibility is that the cloud particles remain spherical during the freezing process. Thus, an uncertainty especially for small particles remains for the liquid and ice classification scheme. But overall the technique represents a significant improvement to diagnose the phase of small cloud particles.
From now on, the terms spherical and aspherical are equivalently used to the terms liquid and ice. The former expressions are used to underline the increased uncertainty in the detection mechanism of small cloud particles.

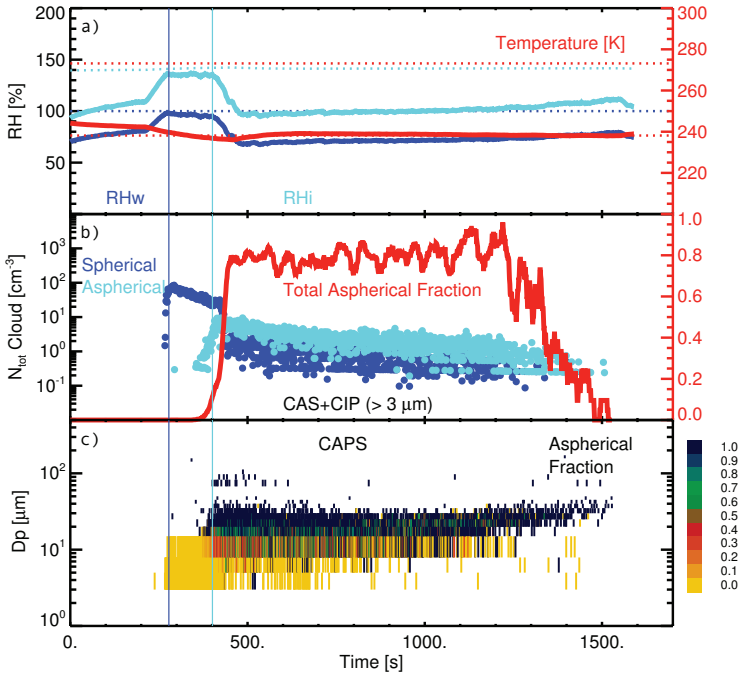

Figure 3.7.: Time series of an AIDA ice cloud cycle (HALO02, experiment 4). a) Temperature (red), $RH_{liquid} = RH_w$ (blue) and $RH_{ice} = RH_i$ (turquoise); b) spherical and aspherical total particle number concentration, aspherical particle fraction (red) and c) size resolved aspherical particle fraction. The calculation of these parameters is based upon the measurement of cross polarized light in NIXE-CAS backward direction as well as the size of the particles. Details about the measurement technique can be found in Sections 3.1.1, 3.1.3, 3.1.4 and Appendix A.5.1. The dark blue line indicate water drop formation and the light blue line simultaneous water droplet evaporation and ice crystal formation.

On the basis of these single ice crystal measurements, also shape patterns might be derived in future to be able to classify different ice crystal shapes.

3.2. CIP greyscale

The second NIXE-CAPS sub-instrument, the NIXE-CIP, is an Optical Particle Counter (OPC), first introduced by Knollenberg (1970). A two dimensional image of cloud droplets and ice particles in the size range between 7.5 µm and 937.5 µm with a resolution of 15 µm is recorded. From the image, the particle shape as well as the particle size can be derived. The following sections give a brief overview over the optical setup as well as the measurement limitations and uncertainties.

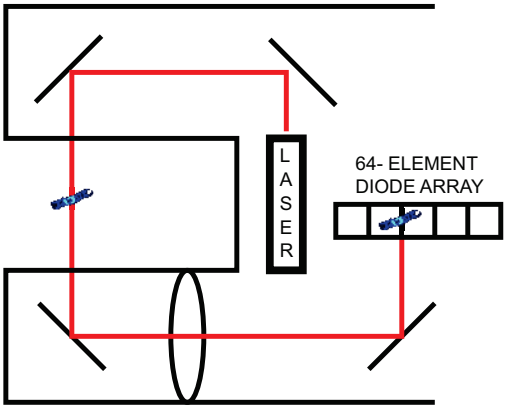

Figure 3.8.: Schematic of the Novel Ice EXpEriment - Cloud Imaging Probe (NIXE-CIP) optical setup

3.2.1. Electro-optical design

In Figure 3.8 the optical setup of the NIXE-CIP instrument is shown. A collimated 680 nm laser beam is directed onto a stream of particles. Particles passing through the laser beam shadow the laser light. This shadow is displayed on a detector array by means of a collecting lens. The detector array consists of 64 elements each 15 µm wide. The intensity of the laser light measured by the detectors is monitored as a voltage level. The voltage level of each array is compared to a running mean value for cloud free conditions. If the voltage level of one detector element deviates by more than 50 % from its running mean value, the state of all detectors is recorded until the light intensity increases to the running mean value for each detector again. A shadowing of more than 50 % thus indicates a particle in the laser beam. The NIXE-CIP electronics convert the measured laser intensity into a digitized signal. The digitized images are compressed by an algorithm described in detail in Droplet Measurement Technologies (2008a) and Droplet Measurement Technologies (2008b). In contrast to older versions, the NIXE-CIP records not only the ON and OFF state of each detector diode but also three different levels of intensity. These levels can be defined by the user but are normally set to 25 %, 50 % and 75 % shading.

The level of each of the 64 detector elements is memorized. Together the 64 detector diodes form an array, called a slice. While the particle moves through the laser beam, the 64-element array needs to be recorded several times to obtain a complete two-dimensional image. Each particle is thus scanned. The frequency rate f at which the state of the detector array is stored is given by:

$$\mathrm{f} = \frac{\mathrm{v}}{\mathrm{res}} \tag{3.4}$$

where v is the particle or air velocity and res=15 µm is the resolution of each detector array element. The number of detector diodes X along one direction, which are shaded by at least 50 %, multiplied by their resolution result in the particle size: $Dp = X \cdot res$.
During aircraft operation the air velocity is determined by a Pitot tube integrated within the NIXE-CAPS instrument. For laboratory operation the air is directly transported to the NIXE-CAPS sample volumes and thus a circulation of the Pitot tube by the sampling air is not given (cf Equation 4.2). For this operation mode a constant velocity larger than the maximum expected air velocity is pre-set. Thus, depending on the quality of the airspeed measurement, over- or undersampling of the image can occur. Undersampling results in information losses while the images get distorted due to oversampling. If the integrated Pitot tube does not provide the correct airspeed, externally measured airspeeds can be used as input parameter.
To determine the NIXE-CIP number concentration, the NIXE-CIP sample volume is important. The mathematical expression of the NIXE-CIP sample volume (SV) is given by Equation 3.5 which is equivalent to Equation 3.1.

$$SV = DOF \cdot EAW \cdot v \cdot t \tag{3.5}$$

The sample area (SA) is defined by its length along the laser beam called depth of field (DOF) and the width of the sample area perpendicular to the DOF and air flow, called Effective Array Width (EAW). Unlike for the NIXE-CAS SA, the NIXE-CIP SA depends on the measured particle diameter. A detailed description of the NIXE-CIP EAW and DOF calculations are given in Appendix A.4.1.

The shadow of the particle image recorded by the NIXE-CIP instrument has one special characteristic. The center of the particle shadow appears bright due to the diffraction of the laser light on the particle image and is called Poisson spot. The Poisson spot is present independently of the particle diameter or the observer distance. Nevertheless the size and intensity level of the Poisson spot are influenced by the distance from the center of field (COF) (Korolev and Isaac, 2006). Due to the limited resolution of the instrument the Poisson spot often isn't visible in the NIXE-CIP image depending on the particle type and imaging conditions.

The NIXE-CIP data recording is similar to NIXE-CAS. The data is stored on an externally connected computer. The internal instruments electronics communicates with the externally installed PADS software in real-time. The PADS software displays the particles and also stores the data. The output are two files, one containing the compressed particle images, the other one housekeeping, meteorological and particle histogram data. The transfer of data between the internal electronics and the PADS software is a limiting factor for the maximum recorded numbers of particles, because during the transfer of data, the probe is not able to detect particles traveling through the sample volume. However the so called 'dead-time' is shortened in comparison to older NIXE-CIP versions.

3.2.2. Calibration of NIXE-CIP

For the size calibration of the NIXE-CIP instrument ideally water droplets should be used. For a correct reproduction of the particle shape the fall speed of the water droplets through the sample volume is needed. For laboratory setups, the Pitot tube which measures the airspeed through the NIXE-CIP sampling volume is not enclosed by the air containing the calibration particles. Thus, another calibration method is needed. The physical equivalence of the diffraction of a spherical water droplet and an opaque disc is useful for that purpose. A disc engraved with several opaque circles of different size is used. The disc is rotated at a constant speed of 25 m/s in the NIXE-CIP sample volume. The velocity is then set to 25 m/s during recording and the optical setup is aligned in such a way that the measured sizes match the known circle sizes.

3.2.3. Particle shape determination

Aside from the particle size, also the particle shape can be determined from the NIXE-CIP images. A NIXE-CIP shape recognition scheme developed by Korolev and Sussman (2000) is implemented in the Jülich evaluation program. The Korolev and Sussman (2000) habit scheme makes use of simple measurements of diameter, perimeter, area and x and y dimensions of the particle to determine the particle shape. A special characteristic of the habit scheme is, that the particles are not classified separately. Rather a statistical analysis of the above mentioned characteristics is performed for particle ensembles of at least 100 particles. The reader is referred to Appendix A.5.2 for more information.
The algorithm classifies the cloud particles into four categories: irregular, needle like, dendric and spherical particles. Unfortunately, spherical ice crystals (e.g. plates) can in some cases not be distinguished from spherical liquid droplets. The fraction of frozen particles (= irregular + needle like + dendric ice crystals) should thus be understood as a lower ice fraction threshold.

3.3. CAPS data processing

The primary NIXE-CAPS output parameters are described in Sections 3.1.1 and 3.2.1. To evaluate the NIXE-CAPS measurements scientifically, these data sets need further processing to reduce the instruments uncertainties. In addition, the NIXE-CAPS output parameters are converted into scientifically useful quantities. From each NIXE-CAPS output file a number frequency histogram can be deduced. From these histograms the following parameters are derived:

- **Particle size distribution:**
  The particle number size concentration dN is the number of particles per unit volume

for each defined size interval. Basically, the number of particles for each size bin is counted and then divided by the individual sample volume for that size and time interval. The NIXE-CAS and NIXE-CIP sample volumes are defined in Sections 3.1.1 and 3.2.1. Each channel can be divided by the logarithmic bin width of the given size interval to obtain the normalized size distribution $\frac{dN}{dlogD_p}$, from now on called $dN/dlogD_p$.

- **Total particle number concentration:**
  The total particle number concentration N_{tot} is the number of particles per unit volume for the whole NIXE-CAPS size range. All particles per size bin per unit volume from the unnormalized particle size distribution add up to the total number concentration N_{tot}. Depending on the scientific task the total particle number concentration of the sub instruments NIXE-CAS or NIXE-CIP can be evaluated separately.

- **Particle shape:**
  For the whole NIXE-CAPS size range between 1 µm and 937.5 µm (except for the size range 50 µm and 67.5 µm) a discrimination between spherical water droplets and ice crystals is possible. The NIXE-CIP shape detection is only applicable for particle sizes larger than 67.5 µm. The derivation of shape information from the NIXE-CAS and NIXE-CIP measurements are described in Section 3.1.4, 3.2.3, A.3.3 and A.5.2 respectively.

- **Water droplet and ice crystal number concentration:**
  To calculate the droplet and ice total number concentration, the percentage of spherical and aspherical particles is multiplied by the corresponding total number concentration. To obtain the droplet and ice size distribution, the NIXE-CAS Particle by Particle (PBP) and NIXE-CIP image data sets and the number size concentrations from the histogram or PBP data sets are combined.

Further parameters which can be calculated from the NIXE-CAPS measurements are: surface area and mass concentration, fall velocity, phase function, extinction, mean and median volume and effective radius, liquid water and ice water content, rain rate and radar reflectivity. The methods are for example described in Droplet Measurement Technologies (2009), Mitchell (1996), Mitchell et al. (1990), Baker and Lawson (2006), Heymsfield et al. (2002). Techniques to evaluate the spatial spacing of cloud particles are described in Baumgardner (1986), Paluch and Baumgardner (1989), Baker (1992), Malinowski et al. (1994). A method to identify the refractive index of aerosol particles is presented by Baumgardner et al. (1996).

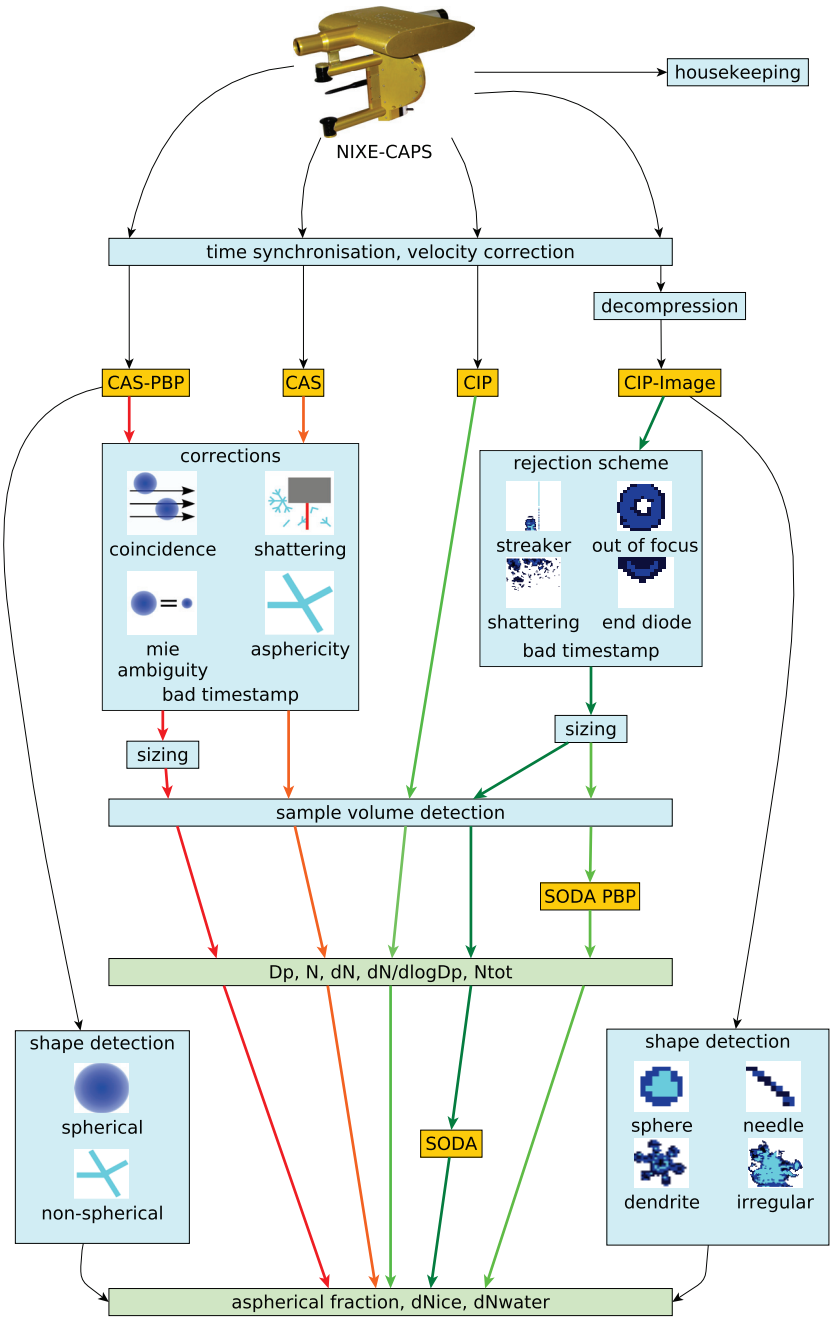

Figure 3.9.: Sketch of the main program steps performed by the Jülich evaluation program to analyze the NIXE-CAPS measurements.

The Jülich evaluation program separately analyzes each data file of each sub instrument. The reason to evaluate all NIXE-CAPS data sets although the contained information overlap is that transmission errors sometimes occur which requires a cross-check of the data. After processing of the individual data files, the data sets are combined. The basic analysis is similar for each data set.
The data processing steps performed by the Jülich evaluation program are sketched in Figure 3.9. A first step is the synchronization of the time recorded by NIXE-CAPS and the respective platform (AIDA or aircraft). A next step is the validation of the NIXE-CAPS velocity, since this is a crucial parameter to determine the sampling volumes and thus the particle concentrations.
For the NIXE-CAS datasets, cloud particles shattered or splashed on the instruments edges have to be removed. Additionally, coincident particle events in the NIXE-CAS sample volume need to be corrected. And finally, ambiguities and influences of the particle size on light scattering (see Section 3.1.3) have to be minimized. A detailed description of the individual correction schemes can be found in Appendix A.5.1.
To evaluate the NIXE-CIP images, the program SODA, developed at National Center for Atmospheric Research (NCAR) (Boulder, USA), is used. Basically, the particle images are processed to deduce the particle size and to reject cloud particles which are not properly imaged. Additionally, sample volume uncertainties (out of focus problems) can be reduced and shattered particles can be rejected. A more detailed description of the individual correction schemes can be found in Appendix A.5.2.
Then, the instruments sample volumes are calculated (see Section 3.1.4 and 3.2.1 and appendix A.5.1 and A.5.2) and the shape of the cloud particles are determined for NIXE-CAS and NIXE-CIP (see Section 3.1.4 and Appendix A.5.2).
In a final step, the liquid and ice total particle number concentrations and size distributions are calculated.

3.4. Measurement limitations and uncertainties

The uncertainties of all NIXE-CAPS quantities are addressed in detail in this section. Additional uncertainties due to unique measurement setups are illustrated in Section 3.5.

3.4.1. NIXE-CAS

The NIXE-CAS dataset covers single particle size as well as ensemble concentration measurements for particles smaller than 50 µm in diameter. The NIXE-CAS uncertainties for these quantities are presented below and are based upon the articles by Baumgardner et al. (1992) and Droplet Measurement Technologies (2009). Extensive revisions of the below presented NIXE-CAS measurement limitations have been conducted. For more information on this type of investigation the reader is referred to e.g. Wendisch et al.

(1996), Hovenac and Lock (1993) or Burnet and Brenguier (2002). The new version of the NIXE-CAS instrument used in this thesis furthermore provides information on the particle phase. No uncertainties for this measurement quantity are published but estimations are presented in Section 3.1.4 and 3.5.

Particle sizing:
Baumgardner et al. (1992) pointed out that errors in particle sizing can result from multiple factors such as laser beam inhomogeneities, electronic response time, scattering ambiguities, shape dependent scattering effects, imprecise knowledge of the particle's refractive indexes, coincident measurements of particles within the laser beam, calibration uncertainties or temperature instabilities of the detectors. All these measurement limitations are discussed below.
Firstly, the intensity of the laser is not uniform but assumed to be Gaussian distributed. The particles are counted when they travel through regions where the intensity is higher than 85 % of the maximum value. The result is a minor spreading of the measured size distribution (Wendisch et al., 1996). Baumgardner et al. (1992) estimated the uncertainty to be in the order of 10 % as the theoretical Mie scattering intensity for particles larger than 1 µm in diameter approximately varies with the second power of the particle size. A by 20 % reduced intensity due to laser beam inhomogeneities thus results in a mis-sizing of approximately 10 %. Additional laser beam non-uniformities were estimated by Hovenac and Lock (1993) to be smaller than 10 %.
Another NIXE-CAS sizing uncertainty described by Baumgardner et al. (1992) is the decrease of the measured intensity due to high airspeeds and large electronic response time. For the new Jülich NIXE-CAS version these uncertainties are negligible though because the electronic system is constructed to accurately operate at airspeeds as high as 200 m/s.
As already discussed in Section 3.1.3, the ambiguity of the Mie and T-matrix scattering curves might lead to misinterpretations of some particle sizes. Combining several size bins reduces the likelihood of mis-sizing. In addition, due to the instrument geometry of the forward detector, the light scattered in the forward hemisphere is slightly shape dependent. Thus, the measured size of the ice crystals is slightly dependent on their orientation in the laser beam. Regarding the asphericity of the ice crystals, Droplet Measurement Technologies (2009) also states that ice particles which pass partly in the sample volume (SV) and partly outside the SV might sometimes be counted. This is due to the scattering pattern which ice crystals generate on the qualifier and forward detectors. With T-matrix calculations however the deviations due to shape dependent scattering can be corrected and minimized as demonstrated by Borrmann et al. (2000).
Normally, for aircraft based measurements the refractive index n of the sample particles is only poorly known. Baumgardner et al. (1992) showed that measurement uncertainties due to refractive index variations are largest for particles between 1 µm and 5 µm in diameter. For larger particles, the refractive index is well approximated by that of liquid water or ice. For smaller particles, the refractive index error should be minimized for example by evaluating additional aerosol composition measurements. For mixed compositions an average refractive index could be used. Overall, the uncertainty due to incomprehensive

knowledge of the refractive index can be reduced to a negligible amount by a reasonable choice of n.
Mis-sizing due to coincident occurrence of particles in the laser beam is addressed by Droplet Measurement Technologies (2009). The measured size of a particle might be increased due to a second particle present in the laser beam at the same time. However, coincidence only becomes important above 750 cm^{-3}. For measurements with concentrations higher than 750 cm^{-3} corrections can be applied (see Section A.5.1). The overall uncertainty due to coincidence effects can thus be neglected when the data is analyzed carefully.
Lastly, other NIXE-CAS sizing limitations are uncertainties of the calibration procedure or instabilities of the temperature control for the forward detectors. For normal operation these uncertainties are in the order of 1 % and thus negligible.

On average, the combined sizing uncertainty of the NIXE-CAS instrument is stated to be ±20 %. But all the above mentioned errors sources need to be taken care off. Otherwise the measurement error can be larger.

Particle number concentration:
The largest source of error for the particle number concentration is the definition of the sample area (SA) in accordance to Droplet Measurement Technologies (2009). The NIXE-CAS sample area (SA) is not strictly rectangular but has its maximum dimension in the center of field (COF) and can be described by a prolate spheroid. The manufacturer used a stream of droplets and a micropositioner to map the sample area (SA) and estimated it to be accurate within ±20 %. This includes slit width, magnification, gain, temperature stability and aberration uncertainties.
For high number concentrations the coincidence of particles in the laser beam and the increased dead-time of the electronic system affects the NIXE-CAS number concentration uncertainty (compare Section A.5.1). The measured number concentration starts to saturate in comparison to the actual cloud concentration. The manufacturer estimated the error in measured number concentration to be smaller than 5 % below 750 cm^{-3} due to a probability of below 1 % of coincidences in the laser beam (cf Baumgardner et al., 1992).
For small total number concentrations N, normally encountered in cirrus clouds, the uncertainty increases due to counting statistics. Baumgardner et al. (1992) predicts a sampling error of about 10 % if the number of sampled particles is approximately 100. Generally the uncertainty is proportional to the square root of the number of particles and is thus negligible for moderate and high number concentrations.
Uncertainties in total number concentration can be increased due to shattering of ice particles and splashing of water droplets on instrument edges. The shattered particles can often be sorted out (cf Section A.5.1). Additionally, comparisons of the NIXE-CAPS measurements to equal quantities obtained by other instruments (e.g. N_{tot}, LWC or IWC) can further be used to confirm the NIXE-CAPS accuracy.
Lastly, airflow distortions can be produced by winglets and other aircraft influences, which may lead to erroneous particle concentrations. The user needs to make sure that such

effects are minimal.

On average the combined uncertainty of the NIXE-CAS number concentration is stated to be ±20 %.

3.4.2. NIXE-CIP

The NIXE-CIP dataset covers single particle size and shape as well as ensemble concentration measurements for particles larger than 7.5 µm in diameter. The NIXE-CIP uncertainties for these quantities are presented below and are based upon the references in Section A.5.2 and the user guide Droplet Measurement Technologies (2009). Extensive revisions of the below presented NIXE-CIP measurement limitations have been conducted. For more information on this type of investigation the reader is referred to Strapp et al. (2001), Gayet et al. (1993) and others.

Particle sizing:
The size of a particle, captured by the NIXE-CIP instrument, is based upon the shadow projection of the image onto a diode array. Distortions of the particle shadow can have several reasons.
First, a two dimensional image is constructed by recording one-dimensional slices of the particle at different positions in the laser beam. The two-dimensional image can then be reconstructed if the speed of the particle through the sample volume is known. Incorrect airspeed measurements, used to record the one dimensional image slices, might lead to an over- or undersampling of the particle. The image of the particle is either compressed or stretched. The particle image can be corrected after recording by using a more accurate airspeed measurement to determine the image sample rate. The manual Droplet Measurement Technologies (2009) estimates the average uncertainty of distortions due to airspeed errors to be about ±15 %.
Knollenberg (1970) developed a rejection scheme for particles that pass the laser beam far away from the center of field (COF) and thus would experience image distortions. With their rejection scheme they stated the sizing to be accurate within 10 %. Later several authors such as Korolev et al. (1991) discovered that for the Knollenberg (1970) rejection scheme larger image distortions might occur. They claim the sizing uncertainty to be up to 65 % for measured particles with diameters below 60 µm. Several correction schemes for spherical particles are proposed but up to now no correction scheme is available for aspherical ice crystals. The sizing uncertainty for the smaller particles measured by NIXE-CIP increases because the detector element dimensions are then equal to the particle dimensions. In extreme cases a 15 µm particle can either shadow one detector element fully or two detector elements by 50 %. This can lead to an oversizing of 100 %. The sizing error decreases with increasing particle size. Thus, NIXE-CIP measurements of particles having diameters below 60 µm should be used with care. For this thesis only NIXE-CIP size measurements above 50 µm are considered whereas for the smaller particle sizes the

NIXE-CAS measurements are used. Thus the largest error source is avoided. The reader should also be aware that the orientation of aspherical ice crystals in the air stream has an influence on the particle size. Nevertheless, this orientation uncertainty is on average reduced when a large ensemble of cloud particles is evaluated.

Overall the uncertainty in measured NIXE-CIP size for particles larger than 60 µm is estimated to be about 20 %.

Particle number concentration:
Similar to NIXE-CAS, the uncertainties in the NIXE-CIP concentration measurements are mainly due to a limited knowledge of the sample volume. The NIXE-CIP sample volume (SV) uncertainty is estimated to be about 20 % (cf de Reus et al., 2009).
The NIXE-CIP electronic system is designed to provide accurate measurements for aircraft velocities up to 200 m/s. Thus, measurement errors due to electronic response times are regarded negligible for the instrument version used here.
For small measured total number concentrations the uncertainties due to counting statistics become important. The uncertainty is proportional to the square root of the number of particles and is thus negligible for moderate and high number concentrations.
Lastly, uncertainties in total number concentration can be increased due to shattering of ice crystals and splashing of water droplets on instrument edges. The shattered particles can mostly be rejected. Additionally, comparisons of the NIXE-CIP measurements to equal quantities obtained by other instruments (e.g. N_{tot}, liquid water content (LWC) or ice water content (IWC)) can further be used to confirm the NIXE-CIP accuracy. Within the sample volume, airflow distortions might occur which are produced by winglets and other aircraft influences. The airflow distortions may lead to erroneous particle concentrations. The user needs to make sure that such effects are minimized.

Overall the uncertainty in measured NIXE-CIP number concentration is estimated to be about 20 %, limited by the uncertainty of the sample volume.

3.5. Instrument inter-comparisons

It is reasonable to check the performance of the new NIXE-CAPS instrument under controlled laboratory conditions prior to the application on aircraft. The operation of the NIXE-CAPS at the laboratory facility AIDA avoids a number of aircraft based disturbances of the measurements, such as shattering effects and air stream changes induced by the wings or other nearby mounted instruments. In addition improved electronics and new optical components justify a comprehensive analysis of the performance of the new Jülich NIXE-CAPS. A number of publications presenting aircraft based comparisons of NIXE-CAPS to other particle measuring systems are already available (cf Baumgardner et al., 2002, Baumgardner, 1983, Gayet et al., 1993) and provide a basis for the here presented

comparisons.
To evaluate the NIXE-CAPS performance under controlled conditions, comparisons to other well established laboratory and aircraft based instruments were performed. These instruments are intensively tested and widely used in atmospheric research. In the following section the operation of the instruments are shortly introduced and inter-comparisons to the NIXE-CAPS instrument are discussed. The different instruments uncertainties are stated below whereas a detailed analysis of the NIXE-CAPS accuracy is presented in Section 3.4.

3.5.1. Comparison of total particle number concentration

One of the fundamental parameters that can be measured with NIXE-CAPS is the total number concentration of particles in the size range between 0.61 µm to 50 µm (NIXE-CAS) and 15 µm to 937.5 µm (NIXE-CIP), respectively. The total particle number concentration is the number of particles in a given size range per unit volume. To compare the total number concentrations of different instruments, their size ranges need to overlap. Only the total particle number concentration in the overlapping size range is then used for comparison purposes. As the NIXE-CAPS instrument covers a very wide range of particle sizes, several instruments covering only a smaller size interval are needed to check the overall validity of the total number concentration measured by NIXE-CAPS. During the AIDA measurement periods, comparisons with the instruments WhitELight ScAttering Spectrometer 1 (WELAS1), WhitELight ScAttering Spectrometer 2 (WELAS2) and the 2- Dimensional Stereo probe (2-DS) are performed.

a. **NIXE-CAS and WELAS1**:
The main instrument which is usually used to measure the total particle number concentration inside the AIDA chamber is the WhitELight ScAttering Spectrometer (WELAS). To cover the whole cloud droplet and ice crystal size range, two instruments are currently in use; the WELAS1 measures particles larger than 0.1 µm and WELAS2 particles larger than 50 µm. Briefly, the WELAS measurement technique is based on light scattering. In contrast to the NIXE-CAS instrument, a white light source is used to illuminate the particles and the scattered light is detected at an angle of 90°. Similar to the NIXE-CAS instrument, WELAS size measurements are calibrated using latex particles. Care has to be taken when ice particle size distributions are analyzed, as the WELAS is only calibrated to spherical particles. Nevertheless, for the WELAS optical setup, the scattered intensity is also slightly dependent on the particle shape. The relative uncertainty in total number concentration is stated to be about 10 % although the count efficiency rapidly decreases below 1 µm. Details are given by Benz (2006).
In Figure 3.10 a time series of total number concentration measured by NIXE-CAS (red) and WELAS1 (yellow) for the size range of 0.61 µm and 50 µm is shown ex-

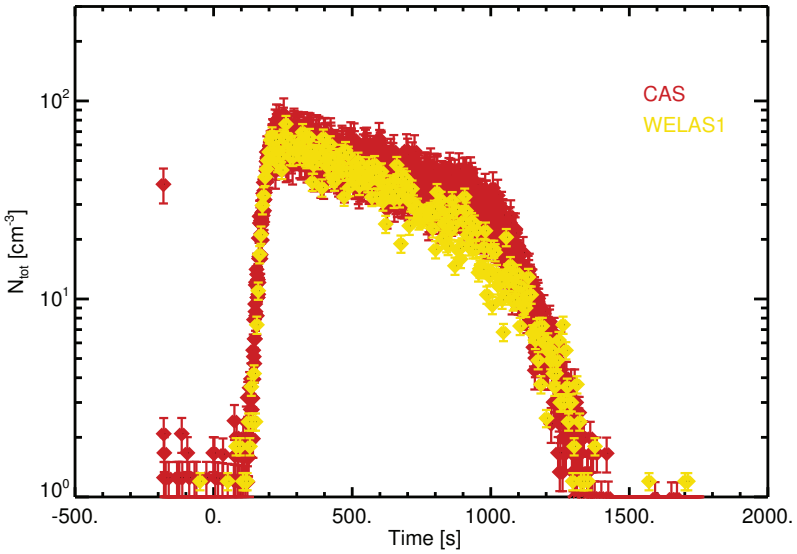

Figure 3.10.: Time series of total number concentration in the size range 0.61 µm and 50 µm for the ACI03 experiment 23 measured by NIXE-CAS in red and WELAS1 in yellow. Created with processed WELAS1 data received in February 2010.

emplary for the ACI03 experiment 23. From the WELAS1 measurement range the total number concentration in the NIXE-CAS size range is extracted. Thus, the two instruments are directly comparable. From Figure 3.10 it is evident that the measured WELAS1 and NIXE-CAS total particle number concentrations agree within their stated uncertainties. This excellent agreement does not hold for all experiments performed at the AIDA chamber. Sometimes large discrepancies are observed for which no systematic behavior such as pressure dependencies could be identified. Furthermore, no obvious instrument malfunctions could be located. Additionally, the scatter of the NIXE-CAS and WELAS1 measured total number concentrations sometimes reach about 20 percent to 30 %. A possible reason for the differences might be sampling losses in the instruments sample tubes. An additional source of uncertainty could be the calculation of the air velocity on the basis of AIDA pressure and temperature measurements instead of using direct velocity measurements to determine the NIXE-CAS sample volume. After all, the exact flow patterns within the sample tubes are unknown. Nonlinear flow usually influences the air velocity which might lead to temporal and spatial velocity fluctuations which are not accounted for in the NIXE-CAS analysis. Finally, the cloud inside the AIDA chamber is not necessarily homogeneous and can lead to a larger scatter in measured total number concentration.

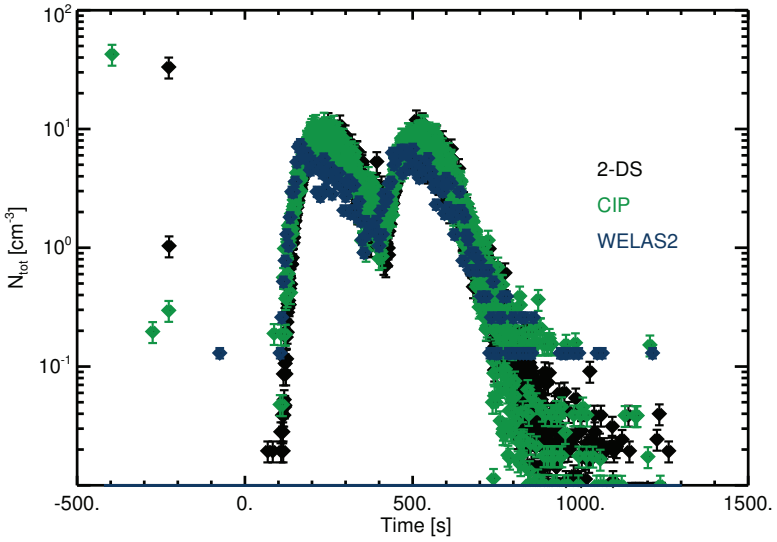

Figure 3.11.: Time series of total number concentration in the size range 15 µm and 945 µm for the ACI03 experiment 44, measured by 2-DS in black, NIXE-CIP in green and WELAS2 in blue. Created with processed WELAS2 data received in August 2010 and processed 2-DS data received in May 2011.

b. **NIXE-CIP, WELAS2 and 2-DS**:
Figure 3.11 displays the comparison of total number concentration for particles sizes between 15 µm and 945 µm. The time series of the total number concentration measured by WELAS2 (blue), NIXE-CIP (green) and 2-DS (black) is shown in Figure 3.10 exemplary for the ACI03 experiment 44. The WELAS2 measurement principle as well as its measurement uncertainties are stated in the last paragraph. The 2-DS is an OPC, like the NIXE-CIP (see Section 3.2.1), but two laser beams, which are installed at right angles, illuminate the particles at the lasers intersection region. Thus, two images of the same particle are recorded. The size resolution of the 2-DS is 10 µm. Size, shape, particle size distribution and total number concentration for particles larger than 10 µm can be determined. The 2-DS uncertainty is stated to be about unit20% for total number concentration. More information about the 2-DS can be found in Lawson et al. (2006).

As displayed in Figure 3.11, the total number concentrations, measured by NIXE-CIP,WELAS2 and 2-DS in the overlapping size interval 60 µm to 250 µm, agree within their stated uncertainties. The variation in time for WELAS2 is slightly different than for the two other instruments which might be due to a slight time shift. It is also evident that the WELAS2 total number concentration is slightly lower than those measured by NIXE-CIP and 2-DS. Additionally the scatter of the NIXE-CIP and 2-DS measurements is slightly broader than for WELAS2. From Figure 3.11 the

spread is estimated to be about 20 % to 30 % for NIXE-CIP. No larger deviations are detected during the other AIDA experiments. Possible reasons for the slight offset of NIXE-CIP to WELAS2 might be due to sampling losses in the sample tubes similar as for NIXE-CAS and WELAS1 . Or fluctuations of the flow in the sampling tubes, which are not accounted for in the calculation of the air velocity from the AIDA pressure and temperature measurements, effect the determination of the NIXE-CIP sample volume (see Section 4.2). Lastly, the homogeneity of the cloud inside the chamber is unknown and might be the reason for the broad band of measured NIXE-CIP total number concentrations.

Overall, the comparisons between NIXE-CAPS and WELAS and 2-DS total particle number concentration measurements agree reasonably. The uncertainty in NIXE-CAS and NIXE-CIP total number concentration for the AIDA experiments is therefore confirmed to be about 30 %, which is in good agreement to formerly published values (see Section 3.4).

3.5.2. Comparison of particle size distribution

The primary parameter measured by the NIXE-CAPS instrument is the particle size distribution. Again, several instruments are needed for the comparison over the whole NIXE-CAPS size range. For the comparison, the normalized particle size distribution of each instrument is used. Secondly, different techniques are employed by the different instruments to determine the particle diameter. Thus, a consistent parameter for particle size must be used when comparing the particle size distributions measured by different instruments. During the AIDA measurement periods the droplet and ice crystal size distributions were measured with the Video Ice Particle Sampler (VIPS), the Small Ice Detector 3 (SID3) and the 2-DS. Aerosol size distributions were measured with the Scanning Mobility Particle Sizer (SMPS) and the Aerodynamic Particle Sizer (APS). The different instrument operation principles and uncertainties are discussed below whereas a detailed analysis of the NIXE-CAPS accuracy is given in Section 3.4. Briefly, the overall uncertainty in size and concentration is estimated to be about 20 %.

a. **Size range** $D_p < 5$ µm**:**
The aerosol size distribution inside the AIDA chamber is typically measured with APS and SMPS. SMPS is used for the small aerosol mode between 0.09 µm and 0.6 µm, whereas with APS the larger aerosol particles between 0.7 µm and 4 µm are measured.
The SMPS (Möhler et al. (2008)) measures the size dependent electrical mobility of particles. Aerosol particles are therefore charged and then separated by size in an externally applied electric field. The narrow size-ranged particles are then counted.
The APS (Möhler et al., 2008) measures the particle size on the basis of the particles

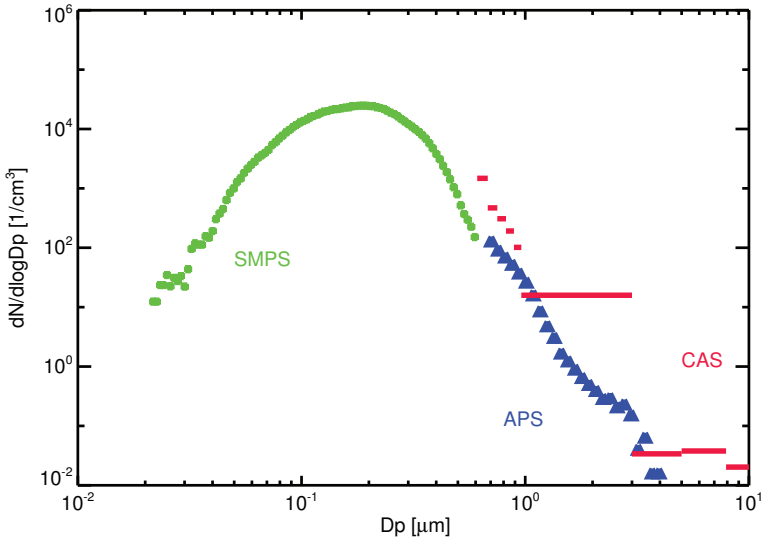

Figure 3.12.: Aerosol size distribution before pump start during the ACI03 experiment 24. The aerosol size distribution measured by SMPS is displayed in green whereas the aerosol size distributions measured by APS and NIXE-CAS are shown in blue and red respectively. Created with processed APS and SMPS data received in July 2010.

inertia after acceleration. The aerodynamic velocity of each aerosol particle depends on the particle surface area and mass. Thus, from the particles aerodynamic velocity, the aerodynamic particle size can be obtained. The aerodynamic particle diameter is the size of a sphere having the same measured aerodynamic characteristics. The SMPS and APS particle sizes are converted into volume-equivalent sphere size. This is the size of a spherical particle having the same terminal velocity as the particles measured with APS and SMPS. For the conversion a shape factor of 1.1 is assumed which from previous comparisons to other measurements is determined to be the appropriate factor (Möhler et al., 2008).

Normalized aerosol size distributions measured by APS (blue), SMPS (green) and NIXE-CAS (red) are displayed in Figure 3.12 for the ACI03 experiment 24. The width of the NIXE-CAS bars indicate the size range of each NIXE-CAS size bin. For sizes below 1 µm the NIXE-CAS size bins are narrow and the NIXE-CAS slightly overlaps the combined size range of SMPS and APS. Overall, the NIXE-CAS size distribution seems to be shifted to slightly larger sizes compared to the measured APS and SMPS size distribution. This behavior is systematically observed for all experiments where APS, SMPS and NIXE-CAS measurements are available. Nevertheless, the envelope of the APS and SMPS and the NIXE-CAS size distributions are similar. The reason for the size shift of the NIXE-CAS size distribution compared to that of APS and SMPS may be due to the different size detection techniques of the

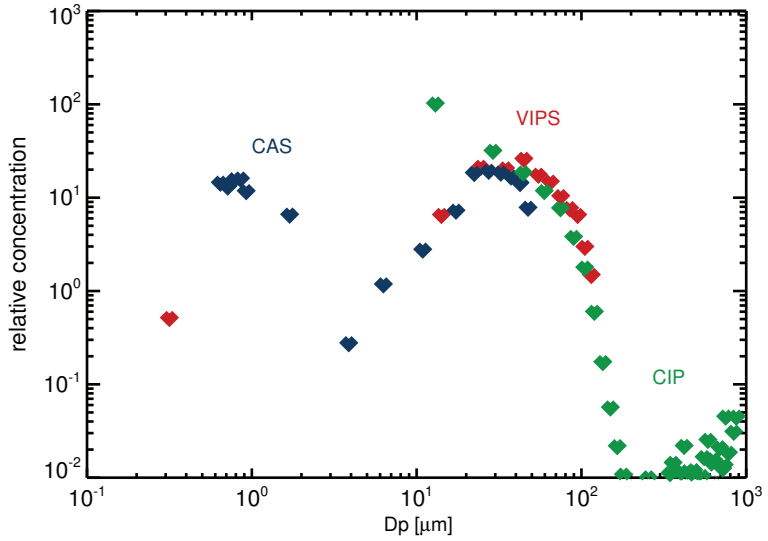

Figure 3.13.: Relative size distributions for the time period 900 s to 925 s after AIDA pump start for the HALO02 experiment 21, measured by NIXE-CAS (blue), NIXE-CIP (green) and VIPS (red). Created with processed VIPS data received in March 2009.

instruments. The diameters measured by NIXE-CAS and APS and SMPS strictly coincide only for spherical aerosol particles.

b. **Size range** $D_p = 5$ µm **to** 50 µm:
To analyze the NIXE-CAPS accuracy for size distribution measurements in the intermediate size range between 5 µm and 50 µm, measurements of the VIPS instrument are used. The VIPS (cf Baumgardner et al. (2002)) is an established airborne particle imaging instrument. A high resolution video camera is focused on a belt coated with silicone oil. Particles are imaged when trapped onto the belt. Particle sizes down to 5 µm can be resolved. The particles are manually sized and counted.

Figure 3.13 displays the particle size distributions measured during the HALO02 experiment 21 by VIPS (red), NIXE-CAS (blue) and NIXE-CIP (green). Since VIPS only records relative number concentrations, only the shape of the size distribution can be compared. From Figure 3.13 it is evident that the shape of the VIPS size distribution for sizes larger than 3 µm can be reproduced by a combination of those from NIXE-CAS and NIXE-CIP. In the overlap region NIXE-CAS and NIXE-CIP also agree reasonable, except for the lowest NIXE-CIP size bin. As already outlined in Section 3.4, the uncertainty for this size bin is high and thus the measured deviation is not surprising. The NIXE-CAS and VIPS aerosol measurements (D_p <3 µm) do not cover the same size range. A combination of the VIPS and NIXE-CAS aerosol mea-

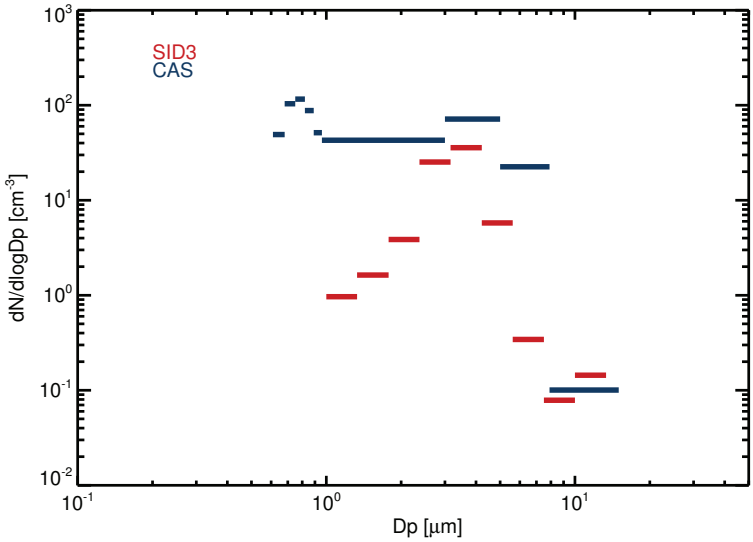

Figure 3.14.: Aerosol, water droplet and ice crystal size distribution measured by NIXE-CIP (green) and SID3 (black). The time period between 787 s and 1087 s after AIDA pump start during the HALO02 experiment 15 is displayed. Created with processed SID3 data received in December 2010.

surements nevertheless results in a reasonable distribution with a maximum around 1 µm and a decrease to smaller sizes.

Another instrument to measure the particle size distributions in the intermediate size range is the SID3 (Schnaiter (2011)). SID3 is a recently developed instrument which measures the light scattered by individual cloud particles larger than 1 µm within the angular range between 6° and 25°. Scattering patterns in azimuthal and polar direction are recorded. The scattering patterns contain information about particle size and shape. Furthermore, each particle is counted to obtain a complete cloud particle size distribution.

Figure 3.14 illustrates the NIXE-CAPS and SID3 size distributions measured during the HALO02 experiment 15 between 787 s and 1087 s after pump start. During this specific experiment, SID3 mainly detected columnar and irregular ice particles. The width of the bars in Figure 3.14 indicates the range of each NIXE-CAS and SID3 size bin. Obviously, the cloud particle distribution measured by SID3 is slightly narrower than the one measured by NIXE-CAPS. Additionally, the maximum values at approximately 4 µm detected by SID3 are a little lower than the ones determined by NIXE-CAPS. Nevertheless, the shape of the measured size distributions agree reasonably and the size at which the maximum concentration is detected is equal. Thus, although the absolute concentrations measured by SID3 and NIXE-CAPS differ slightly, the overall form and concentration range agree reasonably well.

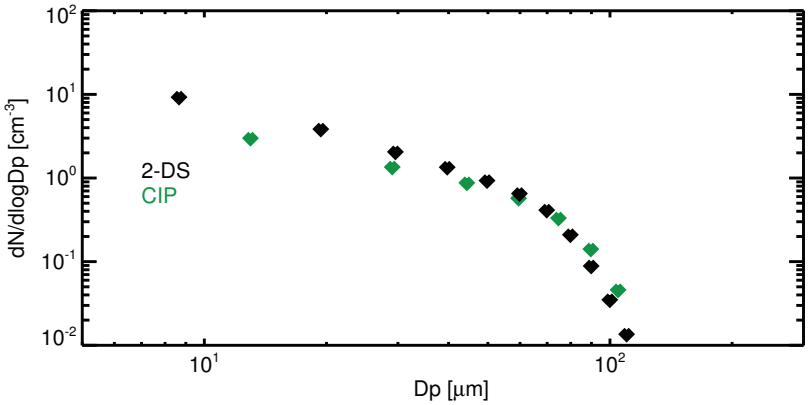

Figure 3.15.: Water droplet and ice crystal size distribution of the NIXE-CIP (green) and 2-DS (black). The particle size distributions measured between 200 s and 300 s after AIDA pump start during the ACI03 experiment 44 are displayed. Created with processed 2-DS data received in May 2011.

c. **Size range** $D_p > 50$ µm**:**
For the larger liquid droplets and ice crystals the size distribution of NIXE-CIP is compared to that measured by the 2-DS, which is already introduced in the previous paragraph. Figure 3.15 is similar to Figures 3.12 and 3.13. The particle size distribution measured by 2-DS during the ACI03 experiment 44 is indicated in black and the one measured by NIXE-CIP is displayed in green. For the larger sizes above 60 µm the NIXE-CIP measures slightly higher particle concentrations, whereas for particle sizes below 40 µm the 2-DS values exceed the NIXE-CIP values. The high uncertainty of measured NIXE-CIP particle numbers for sizes below 60 µm is already addressed in Section 3.4. Overall the measurements agree reasonably well except for the lowest NIXE-CIP size bin.

d. **Sizing:**
Finally a comparison of particle sizes between a newly developed aircraft-based instrument called Particle Habit Imaging and Polar Scattering (PHIPS) and NIXE-CAPS is presented to provide more evidence for an overall good NIXE-CAPS performance. The PHIPS instrument is a newly designed airborne optical sensor for measurements of 3D particle morphology as well as particle phase function (Abdelmonem et al. (2011)). The system consists of two identical vertically positioned imaging devices with which an image resolution of 3 µm can be obtained. Particles in the size range of 10 µm up to 800 µm can be sized. Additionally, the scattering intensity for forward, side and backscattering directions between 1° and 170° with an angular resolution of

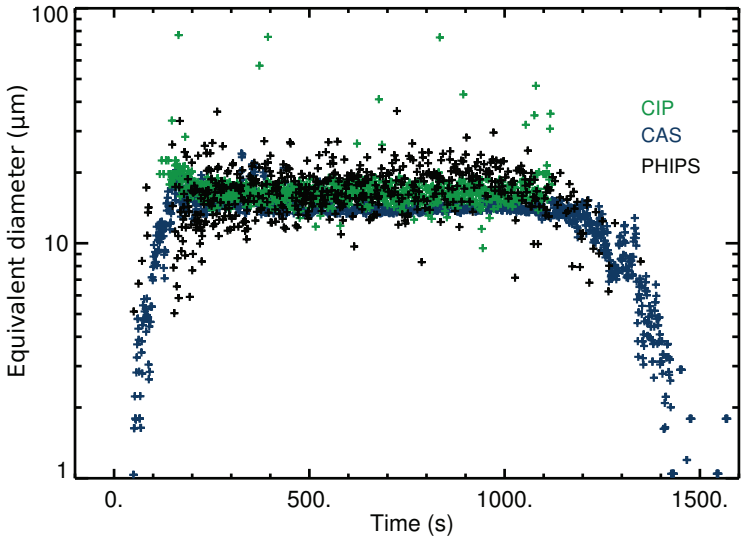

Figure 3.16.: Time series of median volume diameter measured by NIXE-CAS (green) and NIXE-CIP (blue) during the ACI03 experiment 23. The single particle area equivalent diameters which are simulateneously detected with the PHIPS instrument are displayed in black.
Source: Abdelmonem, A., M. Schnaiter, P. Amsler, E. Hesse, J. Meyer, and T. Leisner, 2011: First correlated measurements of the shape and scattering properties of cloud particles using the new Particle Habit Imaging and Polar Scattering (PHIPS) probe. *Atmospheric Measurement Techniques*, 4:2125–2142, doi:10.5194/amt-4-2125-2011

1° to 8° are measured simultaneously. PHIPS is optimized for single particle detection and characterization, not for bulk measurements. A detailed description can be found in Abdelmonem et al. (2011).
Figure 3.16 displays NIXE-CAPS and PHIPS particle sizes measured during the ACI03 ice nucleation experiment 23. Due to its small sample volume in the scattering-imaging synchronization mode, PHIPS detects only a few particles per second. Thus, the black points shown in Figure 3.16 reflect single particle size measurements. In contrast, NIXE-CAS and NIXE-CIP detect large numbers of particles per second. For a reasonable comparison, the one second size distributions detected by NIXE-CAS and NIXE-CIP are converted to a median volume diameter which is a cloud particle volume weighted size. In Figure 3.16, the median volume diameters of NIXE-CAS and NIXE-CIP are displayed in green and blue. The agreement of the presented NIXE-CAS, NIXE-CIP and PHIPS particle sizes is amazingly good considering the different detection methods of PHIPS and NIXE-CAPS. One aspect which adds to the reasonable agreement is the fact that most of the cloud particles exhibit sizes in the overlapping size region of all three instruments.

Overall the comparisons between NIXE-CAPS, APS, SMPS, VIPS, PHIPS, SID3 and 2-DS size distribution measurements are consistent to each other. Only the smallest NIXE-CIP size bin shows a tendency to disagree with other instrument measurements.

3.5.3. Comparison of depolarization

To assess and evaluate the new measurement feature to detect polarized light in backward direction (compare Section 3.1.4), the NIXE-CAPS instrument is compared to the Scattering Intensity Measurements for the Optical detectioNof icE (SIMONE), which is installed at the AIDA chamber to measure the depolarization ratio of particles. The depolarization ratio is defined by $\delta_l = \frac{I_\perp}{I_\parallel}$, where $I_\parallel$ and $I_\perp$ are the parallel and perpendicular polarized components of the backscattered light. The conversion of the NIXE-CAS measurements of cross polarized and total backscattered light into bulk linear depolarization ratio is explained in detail in Appendix A.3.3.
SIMONE is comparable to a LIght Detection And Ranging (LIDAR) system and is used to distinguish the phase of clouds generated inside the AIDA chamber. The measurement setup consists of a 488 nm polarized light beam which is focused onto a 7 cm^{-3} large AIDA air volume. The parallel and perpendicular components of the scattered light are measured at 178°. The linear polarization ratio (see Section 3.1.4) is sensitive to particle asphericity and thus a detection of the bulk cloud phase is possible. With the additional detection of forward scattered light at 2° information on the average particle size can also be deduced. A detailed description of SIMONE can be found in Schnaiter et al. (2007).
Figure 3.17 shows a measured time series of the bulk linear depolarization ratio δ_l (introduced in Section 3.1.4) measured by NIXE-CAS (black) and SIMONE (green). Time series of the same experiment thermodynamic parameters and basic particle measurements are shown in Figure 3.7 and 4.2. A water cloud forms at 280s after experiment start (vertical dark blue line). Before the liquid droplets form, SIMONE detects depolarized light which is generated by aerosol particles present inside the chamber. As can be seen from Figure 3.17, for this time period no change of the polarization state of the NIXE-CAS laser light is detected. This is due to the low sensitivity of the NIXE-CAS polarized back detector during the HALO02 measurement period. From 280 s to 400 s a water cloud is present inside the AIDA chamber. Figure 3.17 reveals that for this time period NIXE-CAS detects a low δ_l which is lower than the linear depolarization ratio level detected by SIMONE. SIMONE uses a smaller detector area which is situated at an angle of 178° whereas inside the NIXE-CAS a circular detector is placed which covers the angular range of 168° to 174°. Furthermore, the background noise is different for the two instruments but plays an important role for such low intensity signals. Thus, the small depolarization signal produced by spherical particles and measured with the two instruments, is different. After 400 s (vertical light blue line) an ice cloud forms inside the AIDA chamber. For this period the measured SIMONE and NIXE-CAS signals both increase to about 0.2. Nevertheless, the scatter of the NIXE-CAS ice depolarization ratio is large in comparison to that of SIMONE. The

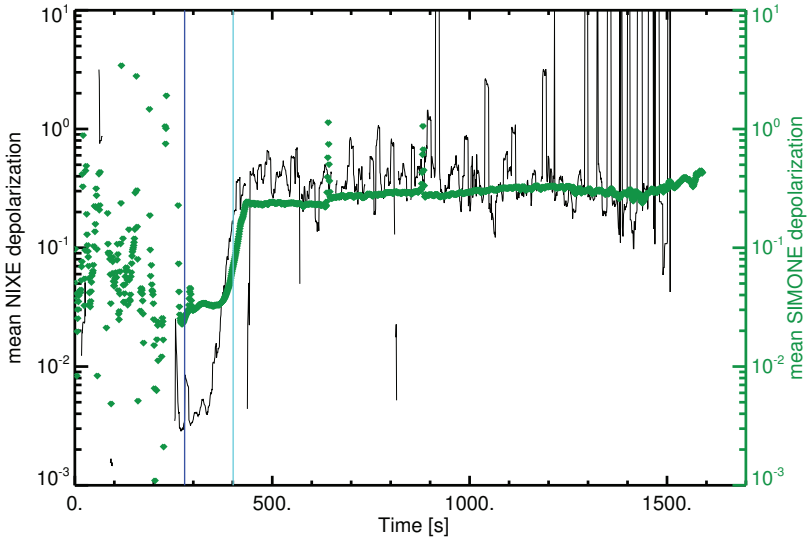

Figure 3.17.: Mean bulk linear depolarization ratio measured by NIXE-CAS (black) in green and SIMONE (green) during the HALO02 experiment 4. The vertical blue line indicates the onset of water drop formation and the vertical light blue line indicates the onset of water drop evaporation and ice crystal growth. Created with processed SIMONE data received in May 2009.

larger variation of the NIXE-CAS linear depolarization ratio observed within ice clouds is probably related to the single particle detection. NIXE-CAS captures a smaller amount of particles per second than SIMONE and thus the orientation of the particles might have an influence on the NIXE-CAS measurement. The good quantitative agreement is due to the fact that the SIMONE measurements obtained during another ice experiment are used to calibrate the NIXE-CAS back detectors (cf Section 3.1.4). However, more important is the fact that the increase of the linear depolarization ratio is detected by both instruments at the same time and that the difference in detected depolarization between water droplets and ice crystals for both instrument is of the same order.

The first attempts to measure depolarization inside a cloud and to detect the phase of cloud particles with NIXE-CAS are thus successful as shown above. The general behavior of the measured linear depolarization ratio is consistent with the SIMONE measurements.

4. NIXE-CAPS at the AIDA chamber and on board of the BAE146

The artificial cloud experiments presented in this thesis were carried out at the laboratory facility Aerosol Interaction and Dynamics in the Atmosphere (AIDA) which is situated at the KIT. This chapter introduces the experimental setup and presents the basic evolution of AIDA clouds. Moreover, a detailed description of the experiments performed as part of this thesis is given. An evaluation of the performance of the NIXE-CAPS instrument is furthermore presented, including extensive comparisons to other instruments.
The natural cloud observations illustrated in this thesis were performed on board of the British aircraft BAE146 over UK territory. In the last sections of this chapter, the instrumental setup as well as the operation of the NIXE-CAPS on board the BAE146 are described. Additionally, an overview over the scientific aims and flight conditions for which mixed-phase clouds are observed, is given.

4.1. Description of the AIDA cloud chamber

The cloud simulation chamber AIDA at the KIT offers the unique possibility to simulate atmospheric aerosol and cloud conditions. Especially aerosol chemistry and liquid and ice cloud formation mechanisms were studied intensively in the past. A detailed description is given by Benz (2006).
Figure 4.1 illustrates the AIDA. The AIDA vessel is a 84.3 m^3 chamber which is embedded in a temperature controlled room. An extensive pump- and cooling system is installed at the bottom which is used to regulate the pressure and temperature conditions inside the chamber. Operational conditions are temperatures between 183 K and 333 K as well as pressures between 0.01 hPa and 1000 hPa. Within the chamber static as well as dynamic pressures and temperatures can be established. A uniform environment is ensured by a fan installed at the chamber bottom. The atmospheric state inside the chamber is monitored by pressure and temperature sensors all along the chamber volume. Aerosol and cloud particle, trace gas and humidity instruments (Möhler et al., 2005, 2006, Ebert et al., 2005) are installed at the AIDA levels 0 to 3. The relative humidity data set is of crucial importance for this thesis. It is determined by Tunable Diode Laser Absorption

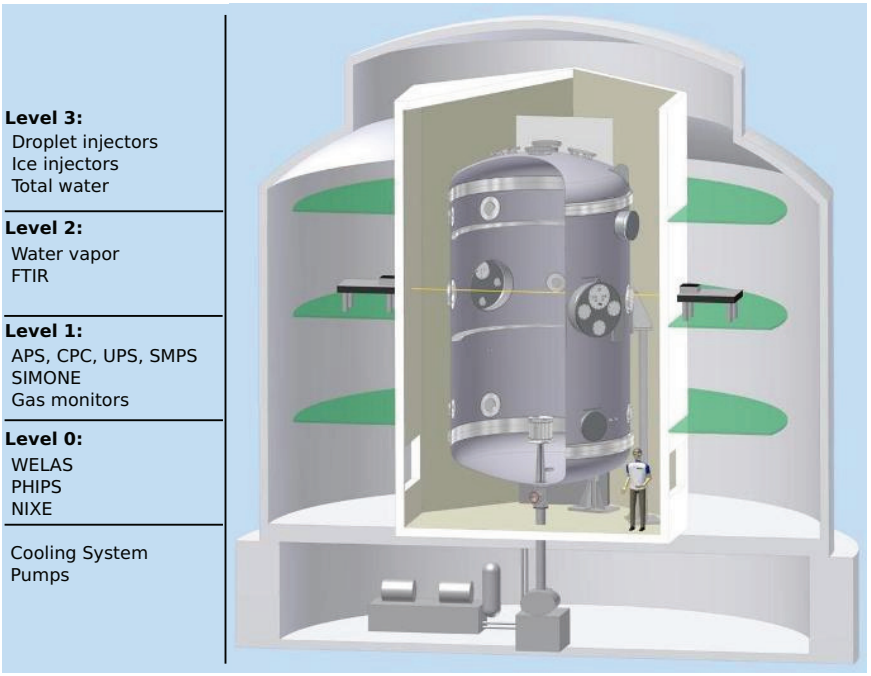

Figure 4.1.: Schematic setup of the AIDA cloud chamber and the permanent instrumentation. The instrumentation is described in detail in Section 4.1. Source: IMK-AAF and Vogt (2011)

Spectroscopy (TDLAS), which means that the water vapor concentration in the chamber is determined from its absorption characteristics. The uncertainty in relative humidity is estimated to be below 10 % (Steinke et al., 2011).

Prior to each aerosol or cloud experiment, the chamber is evacuated to remove possible residual aerosol particles. After refilling the AIDA vessel a well-defined water vapor partial pressure is adjusted. This process comprises the formation of a constant dew or ice layer on the chamber walls depending on the chosen start temperature. After equilibrium is reached, aerosol or small water or ice particles are injected into the chamber. The given temperature prior to an experiment depends on the chosen cloud conditions, whereas in most cases the pressure is equal to the surrounding air outside the chamber. Experiments initiated at lower pressures are also possible. Each experiment is started by pumping air out of the chamber volume. This pressure reduction induces an expansion of the remaining air and simultaneously decreases the temperature.

A typical AIDA cloud experiment is shown in Figure 4.2. The pump start and thus the start of the experiment is set to 0 s. The expansion which is a nearly adiabatic process causes a decrease in gas temperature (red line in Figure 4.2b) and thus an increase of relative humidity with respect to water $RH_w = RH_{liquid}$ and ice $RH_i = RH_{ice}$ (dark and light

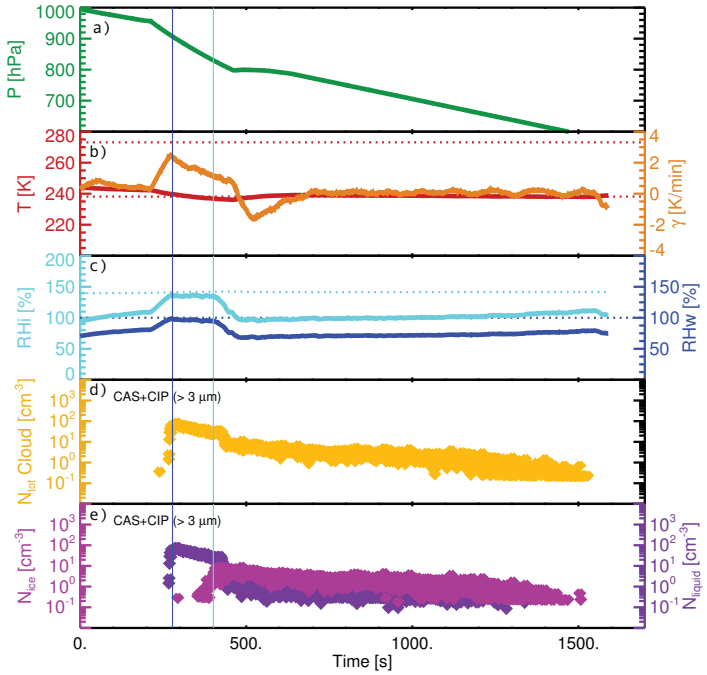

Figure 4.2.: Time series of a) pressure, b) temperature and cooling rate, c) relative humidity with respect to ice and water, d) total cloud number concentration and e) number concentration of water and ice for the HALO02 experiment 4. The dark blue vertical line indicates water drop formation and the light blue line indicates ice cloud formation. The dashed lines in b) show the homogeneous drop freezing and the water melting threshold temperatures. The light blue dashed line in c) indicates the homogeneous freezing threshold and the dark blue line the condensation threshold.

blue lines in panel c). The divergence of the experiment from adiabatic conditions is due to a warming influence of the chamber walls. The formation of a cloud is indicated by an increase of the total number concentration of cloud particles (N_{tot} Cloud) larger than 3 µm (yellow line, Figure 4.2d). Additionally, in Figure 4.2e the cloud particle number concentrations for water and ice (N_{liquid} in purple, N_{ice} in magenta) are shown. To form liquid clouds, the relative humidity with respect to water RH_w has to reach water saturation and the temperature needs to be above −38 °C. For this thesis the formation of mixed-phase clouds in the temperature interval of 0 °C and −38 °C are of major interest. The ice crystals within the AIDA in that temperature interval are commonly formed by heterogeneous drop freezing (compare Section 2.1) below 0 °C. The pumping rate can be readjusted during the experiment to simulate changes in the rate of ascent in the atmosphere.

For a certain pumping rate, the cooling rate γ (orange line in Figure 4.2b) is largest at the beginning of an experiment and reduces continuously due to heat transport from the

chamber walls to the enclosed chamber air. Thus a maximum temperature reduction of approximately 9 K can be achieved.
After pump stop the enclosed air starts to warm up. When RH_w falls below 100 %, water droplets start to evaporate whereas ice crystals evaporate below 100 % RH_i.
Observed AIDA processes are not necessarily representative for the atmosphere because the chamber walls act as source or sink for water vapor independently of the thermodynamic conditions. For the AIDA studies the water flux between the AIDA volume and the AIDA walls need to be taken into account as well as the removal of water due to the pumping process. Furthermore, the maximum size of grown water droplets inside the chamber does not exceed approximately 70 µm. This is due to sedimentation of larger droplets. In the atmosphere, droplets can grow to larger sizes. Finally, AIDA studies are idealized, because small scale variations of temperature and relative humidity cannot be simulated. Thus, the temporal evolution of natural clouds may not be reproduced.

4.2. NIXE-CAPS setup at the AIDA chamber

The NIXE-CAPS is an aircraft-based instrument for aerosol and cloud particle investigations. Normally, the instrument is mounted directly below the aircraft wing (cf Figure 4.5), facing the air to be sampled. Such a setup is not possible at the AIDA chamber. Thus, the chamber air containing the cloud particles has to be transported to the NIXE-CAPS sample volumes. As can be seen in Figure 4.3, the NIXE-CAPS is placed into a canister installed below the AIDA chamber. Two sampling lines emerging out of the chamber bottom are connected to the NIXE-CAPS canister. The sampling lines end above the two NIXE-CAPS sampling volumes so that the air can traverse through both NIXE-CAPS sample volumes. Care has to be taken that the sampling lines are straight so that no cloud particles are lost due to collisions with the sampling tube walls. Another deviation from the normal instrument operation is the measurement of air velocity. As the sampling lines end directly above the sampling volumes, no air is transported past the position at the NIXE-CAPS head where the velocity is normally measured. However, the air velocity is needed to accurately determine the NIXE-CAPS sample volumes (cf Section 3.1.1 and 3.2.1). For the AIDA measurements the air velocity is calculated from the pressure and temperature measurements inside the AIDA chamber. During the measurements a constant air flow of 110 Standard Liters per Minute (SLM) is set. The velocity can then be calculated as follows:

$$v = \frac{Q}{A \cdot \rho} \tag{4.1}$$

where v is the air velocity, Q is the mass air flow, A the sample tube area cross section and ρ is the density of the air. The density of the air depends on air temperature T and pressure p.

$$\rho = \frac{\rho_0 \cdot \mathrm{p} \cdot \mathrm{T}_0}{\mathrm{T} \cdot \mathrm{p}_0} \tag{4.2}$$

where ρ_0 =1.293 kgcm^{-3} for T_0 =273.15 K and p_0 =1013.25 hPa.

While the natural cloud conditions cannot be exactly simulated at the AIDA chamber, it is especially suitable for testing the instrument without influences induced by the aircraft. Normal air velocities through the NIXE-CAPS sample volumes at the AIDA chamber are slower (10 m/s to 25 m/s) than during aircraft operations where air velocities between 100 m/s to 200 m/s occur. Shattering effects as described in Section A.5.1 do not occur at the AIDA chamber because the air is transported vertically from the chamber to the NIXE-CAPS sample volumes.

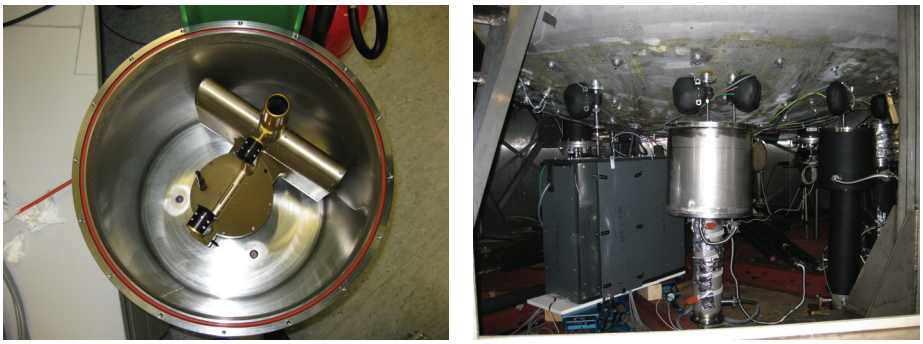

(a) Installation of NIXE-CAPS in a canister (b) Installation of NIXE-CAPS under the AIDA

Figure 4.3.: NIXE-CAPS integration at the AIDA chamber

The setup used for the analysis of the NIXE-CAPS dataset is listed in Table A.3. Basically, no shattering correction is applied to any of the instruments measurements. The speed of the sample air is determined by Equations 4.1 and 4.2. Furthermore, the equivalent-area size detection and the all-in sample volume method are chosen for the NIXE-CIP analysis. The all-in method is chosen because a consistent analysis of all AIDA experiments is preferred for the scientific interpretation and within the AIDA chamber a variety of different, not necessarily symmetric, ice forms are generated. Additionally, most ice crystals observed in the AIDA chamber do not touch the end diodes. For the NIXE-CIP sizing, the equivalent-area sizing method is applied because the NIXE-CAS optical particle size is also dependent on the particles cross sectional area and thus somehow consistent to the NIXE-CIP equivalent-area size. Finally, for the ice crystal NIXE-CAS analysis, a mean ice crystal aspect ratio of A/B = 0.75 is assumed for the definition of the size channel thresholds. The assumption is based upon measurements made by Korolev and Isaac (2003b), who reported mean aspect ratios of A/B = 0.75 for ice crystals observed in mixed-phase clouds. Most important, all cloud particles measured in the NIXE-CIP

size range above 67.5 µm are classified as ice crystals because it is known that the liquid droplets within the AIDA chamber do not grow to sizes larger than 70 µm (see Benz (2006)).

4.3. Description of the cloud experiments

This thesis focuses on the formation and evolution of mixed phase clouds for different thermodynamic situations. The AIDA measurements presented in the following sections were made between 2008 and 2010. A total of 146 experiments within the four measurement periods HALO02, ACI03, ACI04 and BIO05 were performed. Each period focused on different thermodynamic ranges and aerosol types relevant for the temperature range. Thus, a widespread and satisfactory coverage of mixed-phase cloud atmospheric states is accomplished. Consequential, a large variety of ice initiating aerosol types are examined in this thesis, including coated and uncoated mineral dust, soot, biological aerosols, sulphuric acid particles as well as mixtures among these. Table A.1 summarizes the experiment conditions for each measurement period.

The measurement period **HALO02** was carried out in October 2008. The experiments in this period were performed over a wide temperature range between −5 °C and −80 °C. One main focus was the validation of new particle spectrometers which are planned to be used as standard in-situ cloud particle instrumentation on board of the new German research High Altitude and LOng range reseach aircraft (HALO). Thus, part of the experiments were designed to simulate basic cloud formation and evolution processes using well characterized initial aerosol particles such as soot and sulphuric acid which are known to play a role in natural cloud formation. Inter-comparisons of cloud particle sizes and number concentrations measured by different spectrometers were performed. On the other hand, one set of experiments was designed to address the ability of cloud particle imagers to resolve and characterize different ice crystal shapes. Therefore, small seed ice (monocrystalline ice particles) was injected into the chamber which developed into larger ice crystals. The form of these ice crystals depended on the initial experiment temperature and the achieved supersaturation (cf Bailey and Hallet, 2002, 2004).

The measurement periods **ACI03/ACI04** were carried out in October 2009 and October 2010. The experiments in this period focused on the evolution of mixed-phase clouds in an intermediate temperature range between −10 °C and −40 °C. The experiments were designed to evaluate the potential of different types of mineral dust and soot particles with regard to their efficiency to act as Ice Nuclei (IN) and Cloud Condensation Nuclei (CCN). A comprehensive analysis of the activation efficiency with respect to temperature as well as the competition between different types of aerosols on cloud formation was evaluated. Furthermore, the alteration of IN and CCN activity of soot and mineral dust particles in dependence of the thickness of different organic coatings was addressed. Another point of interest was the distribution of water and ice with regard to size and number concentration

during the evolution of the clouds.

The measurement period **BIO05** carried out in March 2010 focused on the evolution of warm clouds between 2 °C and −15 °C. BIO05 was designed to assess the potential of biological particles (especially bacterial cells) to act as CCN and heterogeneous IN. Studies referred in Möhler et al. (2007) indicate that bacteria act as IN at temperatures as high as −4 °C which is significantly higher than other known IN types. Following Möhler et al. (2007), the fraction of IN active cells also increases rapidly with decreasing temperature. The experiments in March 2010 were a follow-up of earlier studies conducted at the AIDA chamber (cf Möhler et al. (2008)). For the bacteria types used then, no IN activity was observed above −5°C and the IN active fraction was rather low of the order of 10^{-4}. But qualitative measurements of the fraction of cloud condensation and ice nucleation active cells in dependence of temperature are rare and thus a main subject addressed during the BIO05 experiments.

4.4. The COALESC campaign

The Combined Observation of the Atmospheric boundary Layer to study the Evolution of StratoCumulus (COALESC) campaign was carried out between February and March 2011 over UK territory. During the campaign, the aircraft BAE146 was used as scientific platform. It covers an altitude range between 50 ft (15 m) above sea or 250 ft (76 m) above ground and 35000 ft (10.7 km). The duration of the COALESC flights are around 5 h to 5.5 h at operational airspeeds of approximately 100 m/s.
The main focus of the aircraft based measurements was the observation of stratocumulus cloud layers as they evolved and were advected from the North sea over land. Another set of flights aimed at observing the evolution of contrails which were produced by the aircraft prior to experiment start. Additionally, flights within cirrus clouds were coordinated with satellite overpasses for validation purposes. Mixed-phase clouds were mainly encountered during the ascent to high altitudes, the descent from high flight levels and at a few intermediate straight flight legs. The geographical location of the mixed-phase clouds observed during the campaign is displayed in Figure 4.4.

Besides the basic thermodynamic measurements of temperature, relative humidity and wind, mainly particle microphysical and chemical measurements were performed. The particle microphysics ranged from measurements of cloud particle size, shape and number concentration to the detection of aerosol mass, size and number concentration. Additionally, total water and liquid and ice water content measurements were conducted.
Besides the NIXE-CAPS particle data, the most important measurement parameter for this thesis is the humidity within the clouds. Two dew point hygrometers, the GE 1011B (General Eastern Instruments (1987)) and the CR2 (Buck research instruments L.L.C. (2008)) which are based upon the same measurement technique, are standardly installed on board of the BAE146 for measurements of the air humidity. The instruments are placed

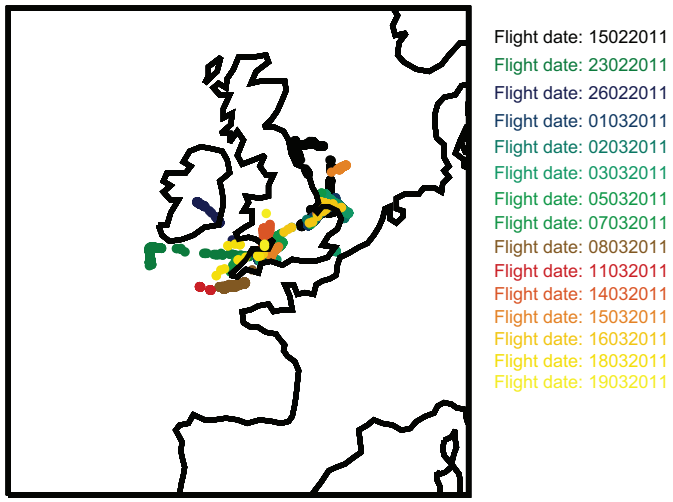

Figure 4.4.: Geographic location of all mixed-phase cloud encounters during the COALESC campaign

inside the aircraft cabin. Sample air is pumped through an inlet into the instruments housings where the air is then directed towards a mirror-like metal surface. The temperature of the mirror is cooled until a liquid or ice layer is established onto the mirror surface. The mirror temperature is regulated so that an equilibrium state between sample air and liquid or ice phase on the mirror is sustained. The temperature at the mirror surface is then measured. The measured temperature is called dew point or frost point temperature (T_d or T_f) depending on the phase of the condensate layer on the mirror.
The equilibrium pressure of water vapor over an ice or liquid surface e_i and e_w can be described by the following two equations (Murphy and Koop, 2005):

$$\begin{aligned} e_w = & \frac{1}{100} \cdot \exp(54.842763 - \frac{6763.22}{T} - 4.210 \cdot \log(T) + 0.000367 \cdot T + \\ & \tanh(0.0415 \cdot (T - 218.8)) \cdot (53.878 - \frac{1331.22}{T} - 9.44523 \cdot \log(T) \\ & + 0.014025 \cdot T)) \end{aligned} \tag{4.3}$$

$$e_i = \frac{1}{100} \cdot \exp\left(9.550426 - \frac{5723.265}{T} + 3.53068 \cdot \log(T) - 0.00728332 \cdot T\right) \tag{4.4}$$

where the stated temperature T range is 110 K to 273.16 K for ice and by 123 K to 332 K for water.
Depending on the phase of the condensate layer, the partial pressure of the sample air e_{gas} is then defined by $e_{gas} = e_w(T_d)$ if a liquid layer is established on the mirror or $e_{gas} = e_i(T_f)$ if an ice layer is formed on the mirror.

The humidity can then be calculated as follows:

$$\mathrm{RH_w} = \frac{\mathrm{e_{gas}}}{\mathrm{e_w\,(T)}} \tag{4.5}$$

$$\mathrm{RH_i} = \frac{\mathrm{e_{gas}}}{\mathrm{e_i\,(T)}} \tag{4.6}$$

where T is the sample air temperature.
Unfortunately, between 0 °C and −30 °C, the phase of the condensate on the instruments mirrors is not unambiguous. The condensate layer may be ice or liquid depending on the flight history. In the laboratory, at temperatures around −20 °C liquid condensate layers are observed up to half an hour before freezing occurs. The data processing for the General Eastern does not include a discrimination of the phase of the condensate on the mirror. Thus, all temperature measurements of the GE 1011B above −20 °C are interpreted as dew point, all below as frost point measurements. This results in an increased uncertainty in the intermediate temperature interval between 0 °C and −20 °C. The CR2 measurements are analyzed more carefully. Periods when the mirror temperature obviously doesn't reflect the ambient humidity or when the phase of the water on the mirror is unknown, are flagged. Additionally, the CR2 has undergone extensive test alongside other hygrometers to improve the data quality.
Overall, for this thesis, the CR2 humidity measurements are preferred. The GE 1011B measurements are used for comparison and backup purposes.

4.5. NIXE-CAPS setup on board of the BAE146

On board of the BAE146, the NIXE-CAPS instrument is installed in a pod below the wing (see Picture 4.5). The pod is part of a main carrier which is installed below the right wing. Six instruments can be positioned in the main carrier. The NIXE-CAPS instrument is installed at the bottom right position where the least influences from other instruments and the wings are expected. The data acquisition and instrument control system is installed inside the aircraft cabin.

NIXE-CAS and NIXE-CIP calibration checks are performed on a regular basis during the campaign period. The parameter setup of the NIXE-CAPS post-flight analysis is listed in Table A.3. The most important difference in comparison to laboratory experiments is the employed correction scheme for shattered ice particles and splashed liquid droplets which is based on an analysis of the single particle interarrival times (see Section A.5.1). In general, for the observed mixed-phase clouds no severe shattering is identified. Only a minor part of the cloud particles is rejected (compare Figure A.4 and Appendix A.5.1). Similar to the evaluation of the laboratory ice crystal measurements, the NIXE-CAS ice particle size thresholds are defined by assuming a mean ice crystal aspect ratio of A/B = 0.75

(a) BAE146 (b) NIXE-CAPS at BAE146

Figure 4.5.: NIXE-CAPS integration on board of the BAE146

for ice crystals observed within mixed-phase clouds. The assumption is based on measurements made by Korolev and Isaac (2003b), who observed a mean ice crystal aspect ratio of A/B = 0.75 for ice crystals observed in mixed-phase clouds. Also similar to the AIDA measurements, the equivalent-area size detection and all-in sample volume method are chosen for the NIXE-CIP analysis.
The airborne NIXE-CAPS velocity measurement is controversial. When comparing it to the measurements of the turbulence probe located at the aircraft nose, the NIXE-CAPS velocity measurement is up to 30 % lower (Abel, 2011). As the two instruments are located at different locations on the aircraft, smaller deviations are expected. Nevertheless, the exact velocity below the wings and thus potential drifts of the NIXE-CAPS velocity measurement are still unknown at present and thus no correction is applied.
Additionally, during the COALESC campaign the overlap of the different gain circuits did not seen to work properly. At this point, the electronic configuration is tested and thus a proper correction scheme is still under development. It is known that the total cloud particle concentration is not affected. The impact on the cloud particle size distribution seems to be dependent on the cloud particle concentration and produces dips at the gain stage intersections (Johnson, 2011). A correction scheme is not included in this analysis but it is expected to not alter the distributions significantly.

5. Results and Discussion

The lack of understanding of the partitioning between liquid droplets and ice during the formation and lifetime of mixed-phase clouds is one of the key uncertainties in state-of-the-art research. In Chapter 2 dynamical influences affecting the glaciation of the cloud over its lifetime are addressed. Commonly the Wegener-Bergeron-Findeisen (WBF) (see section 2.4) is assumed to be the dominant mechanism. It is initiated only for humidity conditions subsaturated with respect to water and supersaturated with respect to ice. Obviously, the water vapor concentration inside the clouds play an important role for the partitioning of the liquid and ice phase. If so, why should the generation of ice within mixed-phase clouds be limited to the WBF process? Indeed, i.e. Korolev (2007a) generalizes the perspective of ice formation and growth in mixed-phase clouds. He suggests that a partial glaciation of mixed-phase clouds might also occur for supersaturated or subsaturated humidity conditions with respect to both liquid and ice (see section 2.4).

To investigate the importance of the thermodynamic environment to mixed-phase cloud glaciation and microphysics, the evolution of mixed-phase clouds is investigated at the AIDA chamber (see section 4.3) for different humidity and temperature regimes. In particular, the fraction of frozen particles and the ice crystal and liquid droplet concentrations are determined in dependence on particle size for the first time. Taking these results into account, observations in natural stratocumulus clouds (see section 4.4) are discussed.

5.1. Relative humidity and microphysical properties in mixed phase clouds

This section explores the effect of water vapor on AIDA mixed-phase clouds in the WBF and coexistence regimes introduced by Korolev (2007a) (see Section 2.4).
The AIDA chamber, presented in Section 4.1, offers ideal conditions to study the evolution of mixed-phase clouds in different humidity regimes under controlled conditions. These conditions may not represent the thermodynamic variability of atmospheric clouds, but the relation between relative humidity and microphysical properties is more obvious.
The expected response of the cloud microphysics to the two different humidity regimes is as follows (see also Section 2.4): If the air is subsaturated with respect to liquid and supersaturated with respect to ice (WBF regime), then the ice crystals are expected to grow on the

expense of the surrounding liquid droplets. If on the other hand, the air is supersaturated with respect to both liquid and ice (coexistence regime), the ice crystals and liquid droplets compete for available water molecules and are expected to grow simultaneously.

Two experiments, one performed in the WBF regime and the other in the coexistence regime, are displayed in Figures 5.1 and 5.2. The two experiments are started at approximately the same initial temperature of −28 °C/245 K and −23 °C/250 K respectively. Panel (a) displays the thermodynamic history of each experiment, temperature in red and $RH_{liquid} = RH_w$ and $RH_{ice} = RH_i$ in dark and light blue colors. Prior to cloud generation, the air within the chamber is cooled to a predefined start temperature. Aerosol particles catalyzing liquid droplet and ice crystal formation during the cooling phase of the experiment are injected into the chamber. For the HALO02 experiment 4 (Figure 5.1) GfG soot, which is similar to diesel soot, is generated in a spark discharge generator (GfG-1000 soot generator, PALAS). Before the start of the ACI03 experiment 6 (Figure 5.2) min OC CAST soot, generated in a combustion aerosol standard burner (miniCAST flame soot generator) and Asian Dust (AD2) is dispersed in the chamber. The cooling at the start of each experiment is accomplished by pumping air out of the chamber, which leads to an expansion of the air inside the chamber. A cooling of the air causes the relative humidity with respect to water and ice to increase. In both experiments, as soon as liquid water saturation (RH_w =100 %) is reached, liquid droplets form. The formation and growth of cloud particles are indicated in panel (b) to (d). In panel (b), the cloud particle size versus experiment time step is displayed. The color code shows the particle number concentration per size bin, with the highest values highlighted in dark red and green. In panel (c), the temporal evolution of the total liquid and ice cloud particle concentration as well as the measured number fraction of ice is shown. The fraction of frozen cloud particles in dependence on particle size is displayed in panel (d). Yellow colors indicate mostly liquid particles whereas blue colors describe increased fractions of ice crystals. The dark blue and light blue vertical lines in the figures indicate the onset of liquid drop and ice crystal formation.

For the experiments shown in Figures 5.1 and 5.2 the temperature conditions and the updraft velocities at experiment start are similar (HALO02 pump rate: 80 % of the maximum AIDA pump speed, HALO02 start temperature: −28 °C/245 K, ACI03 pump rate: 60 % of the maximum AIDA pump speed, ACI03 start temperature: −23 °C/250 K). Here, the glaciation depends on the onset of ice formation, and thus IN activity of the aerosol, and the thermodynamic conditions upon freezing. In the following the development of relative humidity and cloud microphysical properties for the two different experiments are investigated. Especially the observed differences in the relative humidity and the implications for the freezing process and the cloud microphysical properties are discussed.

During the HALO02 experiment 4 (Figure 5.1) the first cloud particles form as soon as RH_w reaches saturation. At that stage, the cloud is purely liquid (panel d), consisting of a large number (a few hundred per cubic centimeter) of relatively small droplets up to about

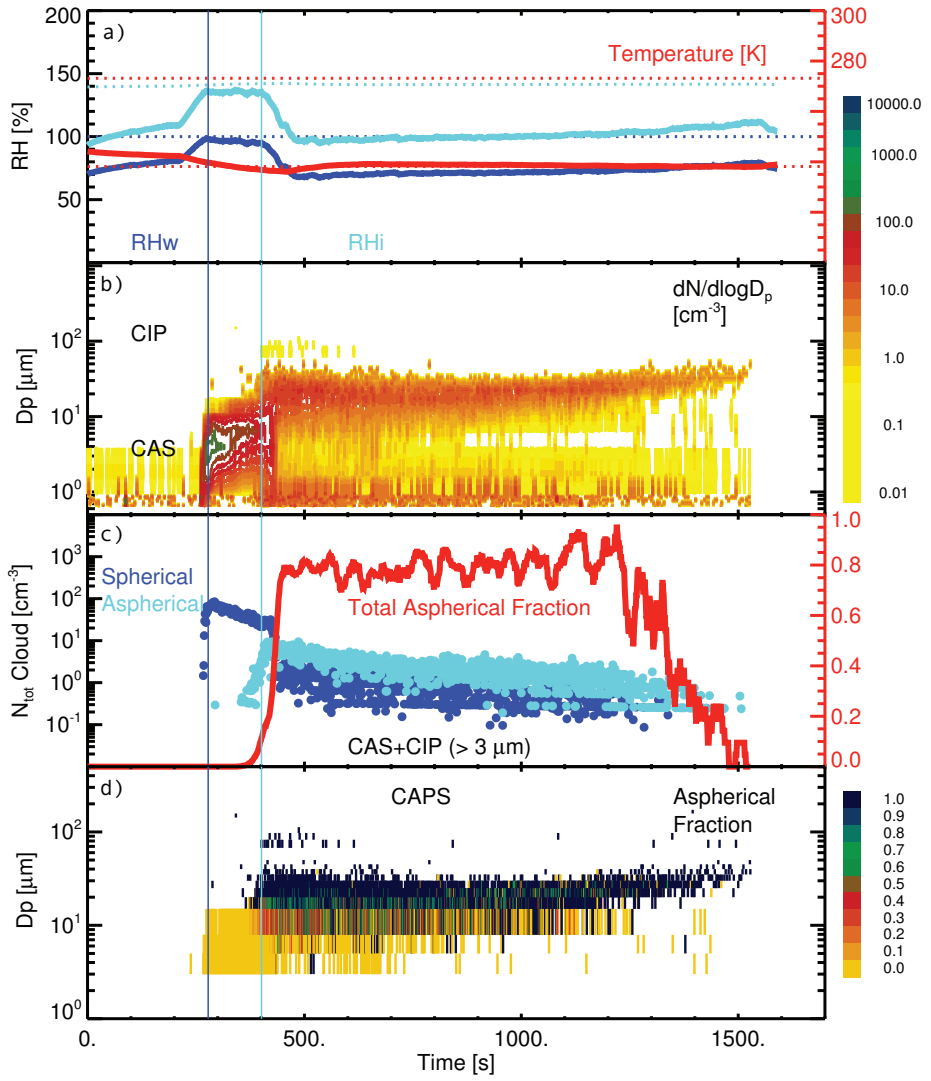

Figure 5.1.: AIDA HALO02 experiment 4, aerosol particles: soot, start temperature: −28 °C. Time series of a) temperature (red), relative humidity with respect to ice and liquid droplets (light and dark blue), b) total number size concentration, c) ice and liquid droplet total number concentration and total aspherical fraction of all cloud particles larger than 3 µm for the HALO02 experiment 4. d) Aspherical cloud particle fraction per time and size interval. The dark blue vertical line indicates water drop formation and the light blue line indicates ice cloud formation. The dashed lines in a) show the freezing and melting threshold temperatures. The light dashed line indicates the homogeneous freezing threshold and the dark blue line the condensation threshold.

20 µm (panel d). Simultaneously, the air is supersaturated with respect to ice, but no ice nucleation is initiated, because the dispersed soot is not very ice active. At 300 s after experiment start, the air temperature decreases to the critical value near 235 K (−38 °C). In this case, it is unclear whether the ice particles form heterogeneously at temperatures slightly above 235 K or homogeneously at exactly 235 K. At the time of ice formation, the cooling rate is considerably decreased in comparison to the experiment start. That is due to heat transfer from the AIDA chamber walls (see section 4.1). Panel a in Figure 5.1 indicates that RH_w becomes subsaturated in the moment when the first ice crystals appear and also during the subsequent cloud period. Thus, the ice crystals can rapidly grow to large sizes on the expense of the surrounding water droplets. During ice formation, the number of cloud particles reduces significantly due to droplet evaporation, whereas the size of the ice particles significantly increases (Figure 5.1c,d). In summary, a rapid conversion from a liquid only cloud, consisting of a large number of small droplets, into a mostly glaciated cloud, consisting of a smaller amount of larger ice crystals, takes place. The glaciation of the cloud occurs fast within a timescale of minutes. The cloud evolution displayed in Figure 5.1 is a typical example for mixed-phase cloud glaciation through the WBF process.

The evolution of the mixed-phase cloud microphysical properties for the ACI03 experiment 6 is displayed in Figure 5.2. Similar to the HALO02 experiment 4, water droplets form as soon as RH_w exceeds 100 %. At the same time, however, the first ice crystals form via immersion freezing (panel d). Most likely, ice formation is initiated immediately by the dust (AD2) particles which are known to nucleate ice at higher temperatures than the soot particles used for the HALO02 experiment 4. At that time, RH_i is close to 140 % while RH_w stays around 100 %. As AD2 is active at higher temperatures and catalyzes ice formation at the beginning of the experiment. In that period the cooling rate is highest (see Section 4.1). The high cooling rate maintains RH_w at 100 % and thus a cloud in the coexistence regime can develop (see Section 2.4). During the following steady-state cooling phase, the total concentration of liquid droplets exceeds the ice crystal concentration by a factor of 100. Nearly all cloud particles larger than 20 µm are frozen whereas all cloud particles smaller than 8 µm remain liquid. Liquid and frozen cloud particles detected in the size range between 8 µm and 20 µm occur in equal portions. In summary, the expected coexistence between a large concentration of liquid droplets and low concentration of ice crystals is observed. The ice crystals tend to be larger than the liquid droplets. The cloud evolution displayed in Figure 5.2 thus is a typical example of a mixed-phase cloud composed of liquid droplets and ice crystals at the same time.

A quantitative comparison of the produced ice crystal and liquid droplet concentration of the two experiments is difficult as the initial environment (especially the temperature) is not exactly equal. Nevertheless, the ice crystal concentrations, which evolved in the course of the two experiments, are of the same order of magnitude. On the other hand, a higher concentration of liquid droplets of slightly smaller size is observed for the experiment where liquid droplets and ice crystals coexist. Most surprisingly when comparing the two experiments is, that the slight difference of RH_w of around 2 % causes a microphys-

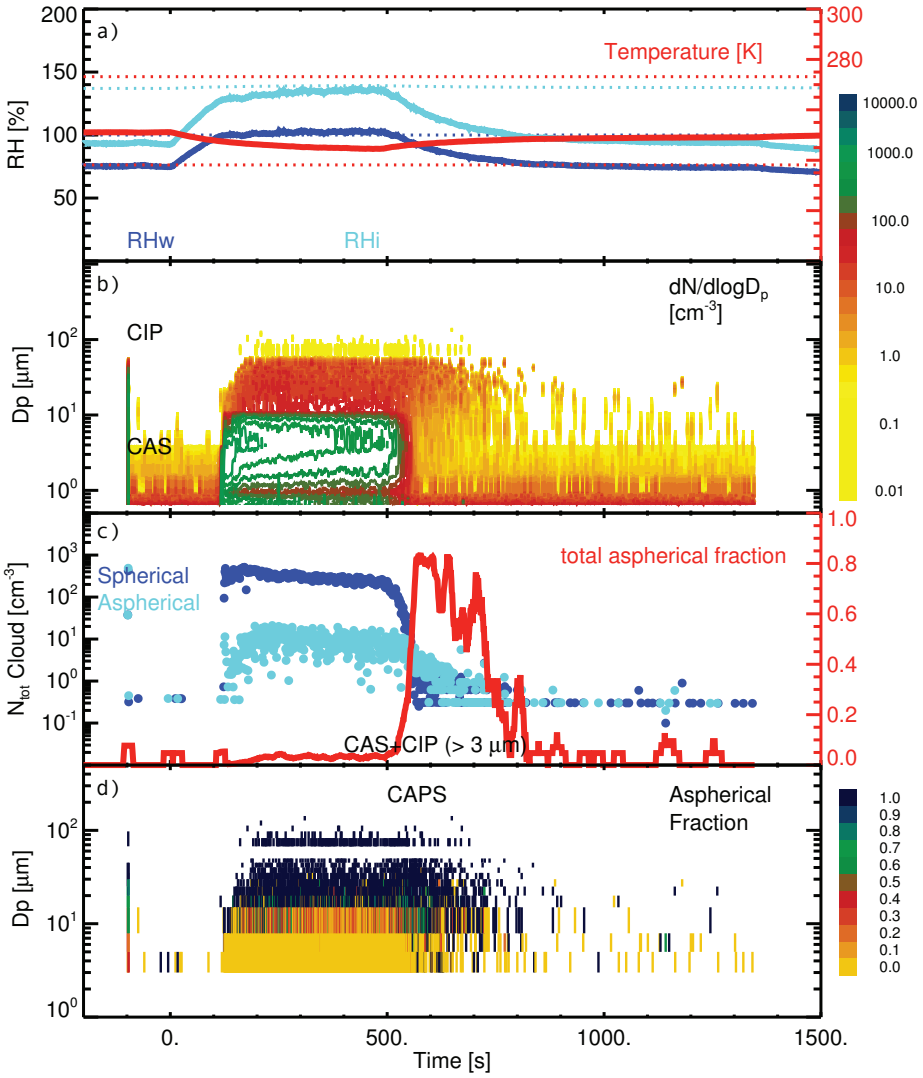

Figure 5.2.: Same as Figure 5.1 but for the AIDA ACI03 experiment 6, aerosol particles: OC CAST soot and AD2, start temperature: −23 °C

ically completely different mixed-phase cloud, which in turn would exhibit very different radiative properties. From these examples, it becomes obvious that the thermodynamic environment strongly controls the microphysical properties and the degree of glaciation in mixed-phase clouds.

5.2. Distribution of water and ice with respect to temperature

5.2.1. AIDA clouds

In Section 5.1 the evolution of mixed-phase cloud microphysical parameters is analyzed for single AIDA cloud events. Here, these observations are summarized for the whole mixed-phase cloud temperature range and for the two different humidity regimes WBF ($RH_w < 100$, $RH_i \geq 100$) and coexistence ($RH_w \geq 100$, $RH_i \geq 100$).
Out of the large number of experiments performed at the AIDA, only those suitable for this investigation have been selected. The selection criteria are described in the following. For this thesis, a connection between environmental thermodynamic situation and mixed-phase cloud microphysical characteristics is searched for, independently of the present CCN and IN type. Within the atmosphere, a variety of different aerosol types exist which exhibit different freezing characteristics. These freezing characteristics mostly determine the onset of ice formation and the initial number of ice crystals, but not the further development of the degree of glaciation. Nevertheless, only aerosols assumed to be active IN or CCN within the specific experiment temperature range are accepted. All experiments involving artificial cloud formation by spraying water droplets, seed ice or glass beads into the AIDA chamber are removed. Further, the formation and evaporation phase of each cloud is removed and only the equilibrium cooling periods are considered since in these periods the microphysics is highly variable. Time periods without cloud activation (e.g. pure aerosol sampling periods) are also rejected. The NIXE-CAPS total number concentrations must exceed 0.1 cm^{-3} before a particle ensemble is accepted as mixed-phase cloud. Finally, only cloud periods in the mixed-phase temperature range of -40 °C to 0 °C are extracted. Naturally, also instrument failure periods either affecting the temperature and humidity or the particle microphysical measurements are excluded.

The microphysical parameters of all experiments selected by the above criteria are averaged in 5 K temperature intervals and are sorted into the WBF and coexistence regimes. The average number fractions of frozen cloud particles per size and temperature interval are displayed in Figures 5.3(a) and 5.3(b) for both regimes. The temperature regions of the corresponding mixed-phase clouds are indicated by color. Blue colors identify colder, red colors warmer temperatures.
The measurements presented here, for the first time, provide a detailed experimental basis of the number fraction of frozen cloud particles, covering the whole cloud particle size

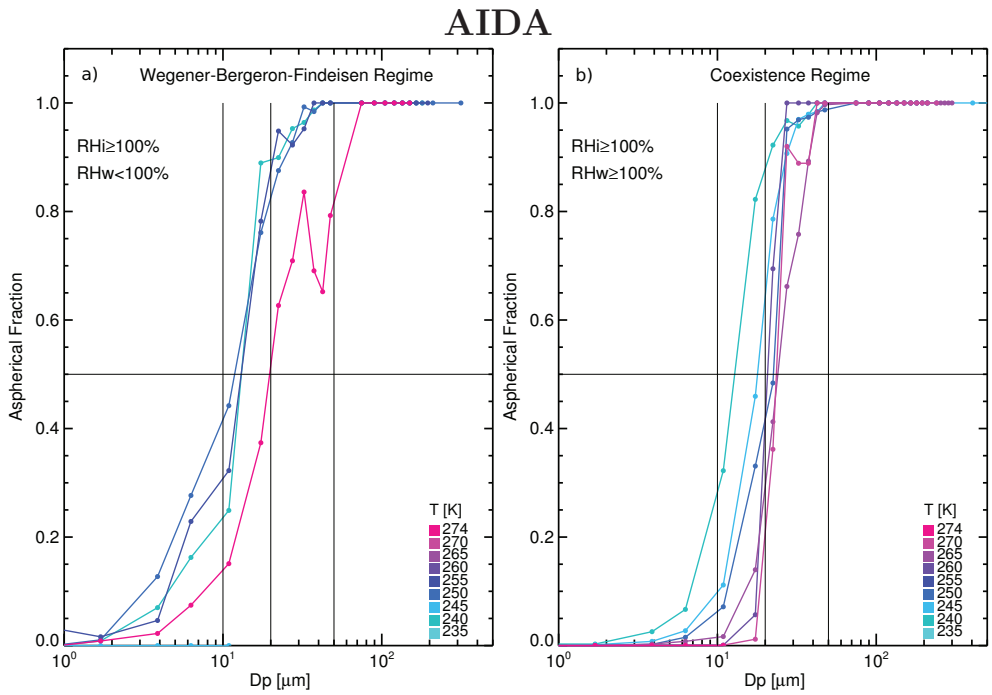

Figure 5.3.: Average number fraction of frozen cloud particles per size and temperature interval for mixed-phase clouds observed in the AIDA chamber in the a) Wegener-Bergeron-Findeisen (WBF) or b) coexistence humidity regimes. The data is averaged into 5 K temperature intervals. Colder ambient temperature observations are indicated in blue whereas warmer temperatures are colored in magenta.

spectrum as well as the complete temperature range of mixed-phase clouds.

Figure 5.3(a) combines all AIDA experiments which are performed in the subsaturated WBF humidity regime. AIDA clouds which evolve in such environments in general contain a large fraction of frozen cloud particles (compare Figure 5.1). Indeed, the blue curves in Figure 5.3(a) indicate that the cloud particles larger than 15 µm tend to be mostly frozen. Nevertheless, for that temperature interval (below −18 °C/255 K) the fraction of frozen cloud particles with diameters below 10 µm is small. The relatively low ice fraction of smaller cloud particles is in parts an instrument artifact which is described in detail in Section 3.1.4. Presumably, the fraction of small ice crystals within the small size range is higher than detected. Nevertheless, in that size interval not all cloud particles are aspherical. This is a surprising detail because in subsaturation especially small liquid droplets are expected to evaporate quickly. The mechanisms which may generate these mixed-phase clouds are as follows: Prior to the time of subsaturation and glaciation through the WBF process, all cloud particles were purely liquid (compare Figure 5.1). The largest liquid

droplets are formed first and have enough time to grow to sizes up to 25 µm. Most likely they contain the largest Cloud Condensation Nuclei (CCN) and Ice Nuclei (IN) because drop activation starts on the largest aerosol particles. Since heterogeneous freezing is related to the number of active sites on the IN (see Section 2.1.2) and thus is a function of the IN surface, the large cloud droplets freeze first and quickly grow to larger sizes. Therefore, all cloud particles larger than 25 µm are frozen and the ice fraction above that size is always 1. The smaller aerosol particles immersed in the small cloud droplets are less active and thus these cloud droplets more likely stay liquid. In general, when the WBF process takes place, the small cloud droplets evaporate quickly and thus the ice fraction in the small size range increases.
The highest temperature curve which represents experiments between 0 °C and −4 °C (274 K and 270 K, magenta curve in Figure 5.3(a)) is shifted to larger sizes in comparison to all other temperature regimes. On average the fraction of frozen particles below 30 µm is lower compared to the lower temperature intervals. A higher number of cloud droplets is the reason for this decrease of the ice fraction (see also Section 5.3). A possible explanation for this higher number might be that the evaporation of droplets and simultaneous ice growth is driven by the difference between RH_w and RH_i, which becomes larger with decreasing temperature (see Figure 2.2b). Overall, AIDA mixed-phase clouds in the WBF regime tend to be highly glaciated regardless of the surrounding air temperature.

The average glaciation behavior of mixed-phase clouds being exposed to coexistence humidity conditions is different. In comparison to Figure 5.3(a) the curves in Figure 5.3(b) are shifted towards larger sizes. This means that the fraction of frozen cloud particles smaller than 15 µm is lower for mixed-phase clouds in the coexistence region than for clouds in the WBF regime. The only exception is the curve representing the temperature interval of −38 °C to −33 °C (235 K to 240 K) which is at the same position in both figures. Thus in general, liquid droplets dominate the mixed-phase clouds encountered in coexistent humidity environments in the small size range. The larger cloud particles above 30 µm in contrast are almost all frozen. Thus, the cloud size range of these mixed-phase clouds can be divided into two size regions for the temperatures down to −35 °C/ 238 °C. Ice crystals dominate the large whereas liquid droplets dominate the small size spectrum. Liquid droplets and ice crystals of the same size are observed in the size range of about 15 µm to 40 µm. Additionally, under coexistent conditions the size of the largest observed cloud ice crystals is in general larger compared to ice crystal sizes which are observed in clouds encountered in the WBF regime. This is especially evident for the warmest temperature interval (magenta curves), where the largest ice crystals in Figure 5.3(a) only reach approximately 150 µm in contrast to nearly 300 µm in Figure 5.3(b).
Another interesting detail in Figures 5.3(a) and 5.3(b) is the dependence of the number fraction of frozen particles on temperature. For mixed-phase clouds observed in the WBF regime (Figure 5.3(a)) the curves in the colder temperature interval between −18 °C and −38 °C (255 K to 235 K) show an almost equal trend. Only the magenta curve which represents experiments performed in the warmest temperature interval between 0 °C and −4 °C is shifted towards larger sizes. Thus in these clouds the portion of liquid droplets is

higher compared to clouds in colder conditions. It should be noted that in the WBF regime no experiments in the intermediate temperature range between −5 °C and −18 °C/255 K were performed. In the coexistence region (Figure 5.3(b)), the ice fraction of cloud particles smaller than 40 µm increases with decreasing temperature. The increased fraction of smaller ice crystals with decreasing temperature is presumably due to the increased probability of heterogeneous nucleation at low temperatures.

5.2.2. COALESC natural clouds

However, it is unclear whether the above observed temperature dependence of the AIDA clouds is transferable to natural cloud systems. Do the natural clouds form and evolve as simulated in the AIDA? Or do other influences alter the observed fraction of frozen cloud particles? NIXE-CAPS microphysical measurements obtained during the COALESC campaign over the UK in March 2011 are presented here to reassess the connection between microphysical cloud characteristics and the environmental conditions for natural mixed-phase clouds. The mixed-phase selection criteria are similar to those applied to the AIDA clouds, although the aerosol rejection criteria (e.g. rejection of glass bead or seed ice experiments) are obsolete in natural mixed-phase clouds. Similar to Figures 5.3(a) and 5.3(b), the fraction of frozen cloud particles per temperature and size interval averaged over all mixed-phase clouds encountered in the WBF and coexistence humidity environments are displayed in Figures 5.4(a) and 5.4(b). In the atmosphere, mixed-phase clouds are also encountered in a third humidity regime (Figure 5.6). Here, both RH_w and RH_i are below 100 %, and thus evaporation of droplets and ice should occur (evaporation regime).
The fraction of frozen cloud particles in the COALESC natural clouds in the WBF regime (Figure 5.4(a)) is in general low compared to the findings in the AIDA chamber (Figure 5.3(a)). Almost all smaller cloud particles (below 20 µm in diameter) and a significant fraction (20 %-60 %) of the larger cloud particles remain liquid.
Moreover, almost all cloud particles smaller than 100 µm are liquid above −13 °C/260 K. The question remains if these observations are representative for single cloud events. Or is the coexistence of large liquid and frozen cloud particles a result of taking the mean between mixed-phase clouds which contain only large liquid or only large frozen cloud particles? In the same line of thought it is also possible that the low ice fraction of cloud particles between 15 µm and 50 µm in Figure 5.4(a) is a result of averaging a small number of mostly frozen cloud events with a large amount of mostly liquid clouds. In Figure 5.5, a time series of a mixed-phase cloud observed during COALESC is shown. This cloud section is representative for all mixed-phase cloud encounters during COALESC and indicates that indeed the large droplets coexist with large ice crystals and that the fraction of small frozen cloud particles is low. Probably, this coexistence is possible due to the relatively low amount of IN present within the atmosphere. No mostly glaciated clouds are observed in the temperature interval of 0 °C to −40 °C during COALESC.
Similar to Figures 5.4(a) and 5.4(b), the temperature behavior of the fraction of frozen cloud particles is shown for the evaporation regime in Figure 5.6. For all three humidity

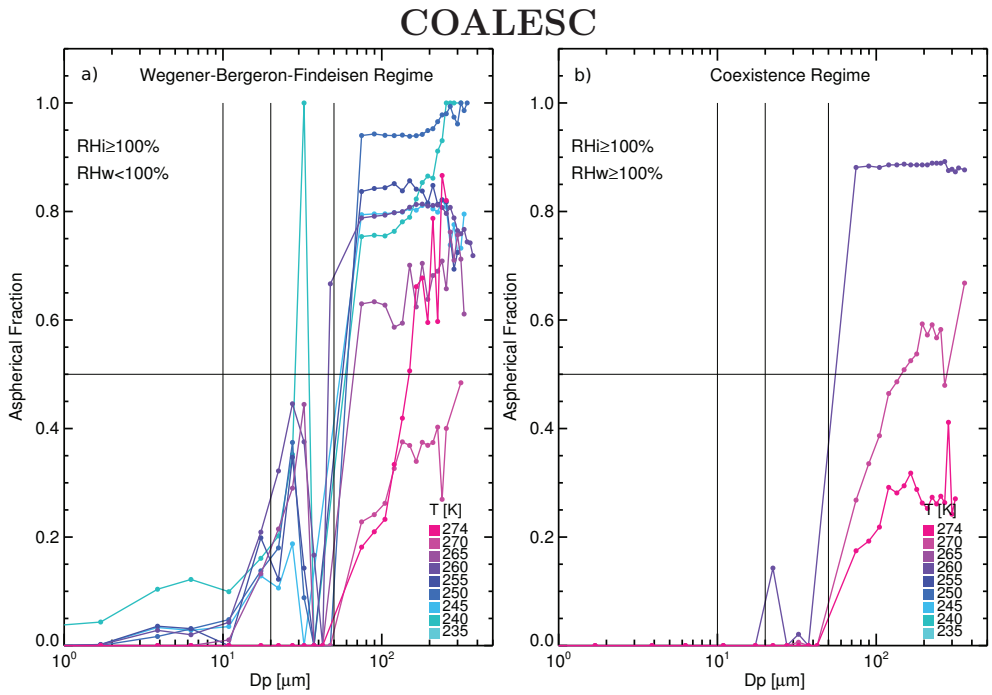

Figure 5.4.: Same as Figure 5.3(a) but for natural mixed-phase clouds observed during the COALESC campaign in the a) Wegener-Bergeron-Findeisen (WBF) and b) coexistence humidity regimes.

regimes, the temperature behavior is similar and can be divided into two regions. Above −13 °C/260 K the fraction of frozen cloud particles in general is very low. Only the largest particles have an increased probability to be frozen. At lower temperatures, the behavior is similar to the findings in AIDA mixed-phase clouds in the coexistence humidity regime, though with lower observed ice fractions. The colder the temperature is, the smaller are the cloud particles that freeze. The reason that no difference in ice fraction is observed between the humidity regimes might be due to limitations and offsets of the relative humidity measurements on board the BAE146. It seems to be impossible to distinguish between sub- or supersaturated regions of RH_w inside the clouds. It is known that the response time of the hygrometer CR2 on board the BAE146 is slow and thus small scale humidity fluctuations might not be resolved. Additionally, due to reasons explained in Section 5.4, the humidity measurements might have a wet bias and thus most of the measured COALESC natural mixed-phase clouds might actually have been observed in the WBF regime.

To summarize, the fraction of frozen cloud particles in the COALESC natural clouds is generally low. Especially above −13 °C/260 K, only few ice crystals are observed. Coex-

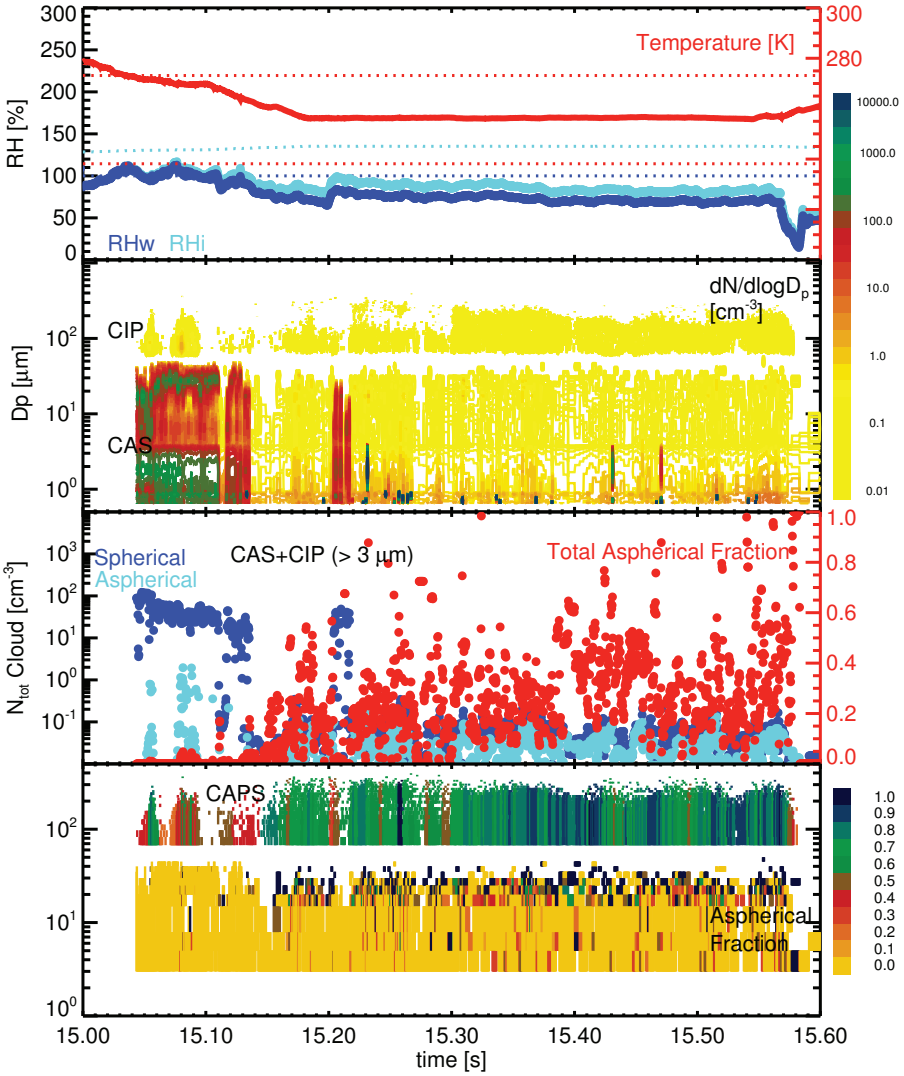

Figure 5.5.: Same as Figure 5.1 but for a mixed-phase cloud observed during the first flight of the CO-ALESC campaign

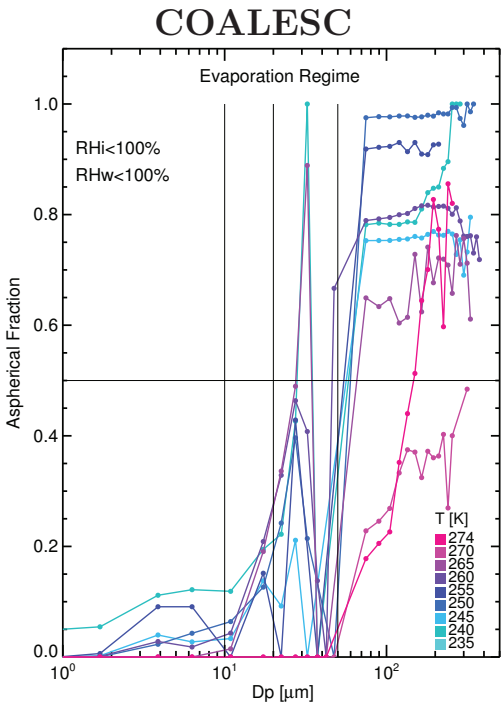

Figure 5.6.: Same as Figure 5.3(a) but for the natural mixed-phase clouds observed during the COALESC campaign in the evaporation regime

istence of large ice crystals and smaller liquid droplets is found regardless of the humidity regime. In contrast, for the AIDA mixed-phase clouds, larger ice crystals and smaller liquid droplets are only observed simultaneously in the coexistence regime, while complete glaciation is found in the WBF regime. A discussion of these results is presented in Section 5.4.

5.3. Size distributions of water droplets and ice crystals

5.3.1. AIDA clouds

The amount of liquid droplets and ice crystals influences the clouds radiative properties. Therefore, the drop and ice crystal size distributions ($dN/dlogD_{p,i}$ and $dN/dlogD_{p,w}$) are important cloud properties which could be measured for the first time in the frame of this thesis. The same mixed-phase cloud intervals presented as in section 5.2 have been selected and a classification into the three humidity regions (WBF, coexistence and evaporation regime) has been performed. The droplet and ice crystal size distributions of each

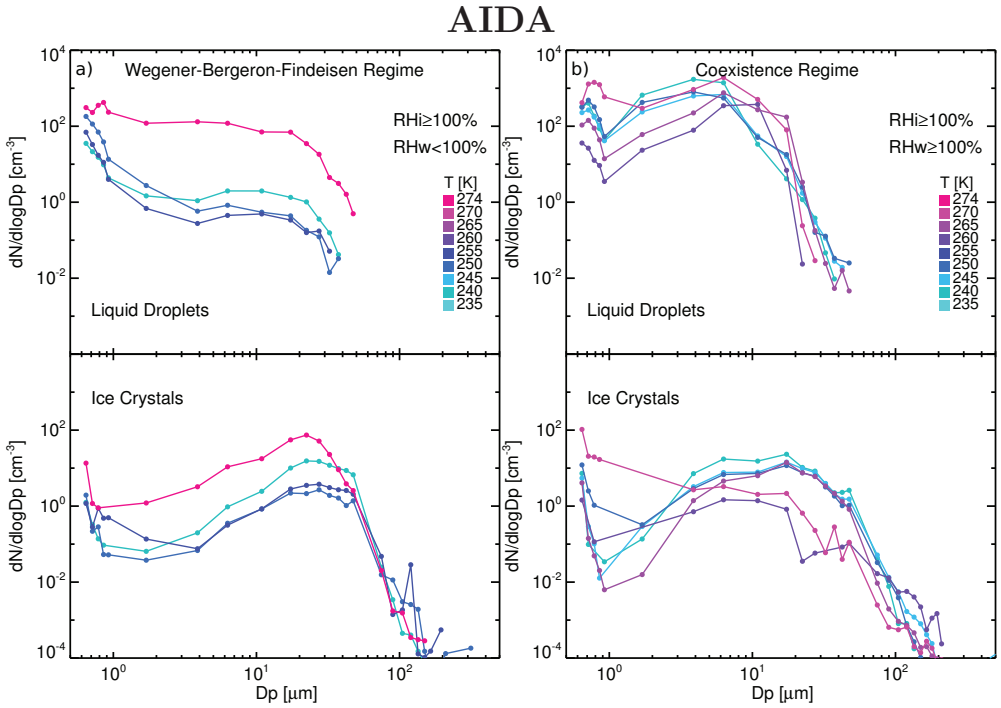

Figure 5.7.: Average size distribution of liquid droplets (top panels) and ice crystals (bottom panels) per size and temperature interval for mixed-phase clouds observed in the AIDA chamber in a) Wegener-Bergeron-Findeisen (WBF) and b) coexistence humidity conditions. The data is averaged into 5 K temperature intervals. Colder ambient temperatures are indicated in blue whereas warmer temperatures are colored in magenta.

dataset are averaged into 5 K temperature intervals.

The mean ice crystal and liquid drop size distributions observed in AIDA clouds are shown in Figures 5.7(a) and 5.7(b) for the WBF and coexistence regimes. The top and bottom panels display the averaged droplet and ice crystal size distributions in the different temperature intervals. Warmer mixed-phase cloud temperatures (near 0 °C) are colored in purple and colder temperatures (near −35 °C) in light blue.

In Section 5.2 it is shown that the AIDA clouds in the WBF conditions are mostly glaciated. Only in the size interval below 15 µm spherical particles classified as liquid droplets are detected. This behavior is reflected in the drop and ice size distributions (Figure 5.7(a)). The concentration of the droplets (>1 µm) is in general low in the WBF regime (1 cm^{-3}) for lower temperatures (Figure 5.7(a)) and becomes negligible for sizes larger than 20 µm. As already explained in Section 5.2, the NIXE-CAS phase detection algorithm has an increased uncertainty in the small size range. Thus, the number of small droplets might be smaller. The concentration of ice particles increases from 0.1 cm^{-3} at 1 µm to a few

10 cm^{-3} at 20 µm and decreases again for larger sizes. Thus, below 10 µm the droplets dominate the size spectrum, while above 10 µm the ice crystals prevail. The largest observed ice crystals are a few hundred µm in diameter.
No strong temperature dependence of the size distributions is obvious, except for the highest temperature interval of −3 °C to 0 °C (270 K and 273 K, pink line). This behavior is reflected in the ice fractions shown in Figure 5.3(a). There, it is already discussed that the difference between RH_w and RH_i might drive the evaporation of the droplets and thus the drop number is higher at warmer temperatures. From the ice crystal size distribution it can be seen that the largest amount of crystals are found in the highest temperature interval.
For AIDA clouds in the coexistence regime, the inspection of the ice fraction (Section 5.2 and Figure 5.3(b)) already revealed that the small cloud particles (<20 µm) have an increased probability to remain liquid. This behavior is reflected in the drop and ice size distributions shown in Figure 5.7(b). Since $RH_w > 100$ %, the size spectrum in the small size range up to 20 µm is dominated by liquid droplets with concentrations around 500 cm^{-3} to 1000 cm^{-3}. For larger sizes, the liquid droplet concentration decreases rapidly down to 0.001 cm^{-3} at 50 µm. On the other hand, the concentration of frozen cloud particles remains quite constant (around 10 cm^{-3}) in the size range of 5 µm to 40 µm and decreases for smaller or larger sizes.The largest frozen cloud particles of a few hundred µm are observed at concentrations around 0.001 cm^{-3}.
For the coexistence region (Figure 5.7(b)), only a slight temperature dependence of the droplet and ice crystal sizes is observable, i.e. the drop spectrum shifts to smaller sizes and the ice crystal concentration increases with decreasing temperature. This shift causes the 'cut-off' size (where 50 % of the droplets are frozen) to decrease with temperature (see Figure 5.3(b)).
When comparing the liquid and ice size spectra of clouds evolved in WBF and coexistence humidity regimes (Figures 5.7(a) and 5.7(b)), both the maximum size of the liquid droplets and ice crystals tend to be slightly larger in the coexistence regime due to the supersaturated humidity conditions. The evolved ice concentrations tend to be of the same order in the coexistence and the WBF regimes for sizes <20 µm.

5.3.2. COALESC natural clouds

The ice fraction in the COALESC natural clouds observed over the UK was shown to be smaller than in the AIDA clouds (see Section 5.2). Additionally, the ice fractions are similar for all COALESC natural clouds regardless of the humidity regimes. No increased ice fraction is detected in the WBF regime. In Section 5.2 it is pointed out that probably most COALESC clouds are observed in the WBF regime, but that the assignment of a cloud to a regime might suffer from the limited precision of the RH_w measurement.
This is also obvious from the ice and drop size distributions (see Figures 5.8(a), 5.8(b) and 5.9) which are similar for all three regions. It is especially peculiar, that the drop and ice size distributions don't change in the evaporation regime. This again points to a difficulty

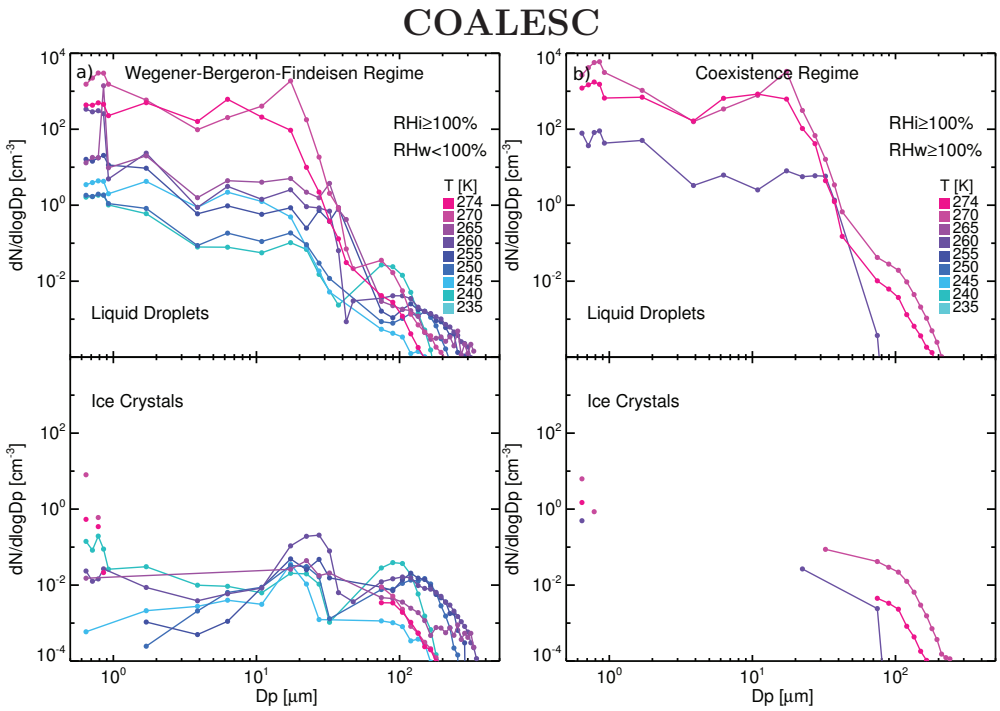

Figure 5.8.: Same as Figure 5.7(a) and 5.7(b) but for the natural mixed-phase clouds observed during the COALESC campaign.

in sorting the clouds into regimes based on the RH_w measurements.
Since the drop numbers are comparable to those in the AIDA WBF regime and also decrease with temperature, the COALESC clouds seem to be mostly in the subsaturated WBF regime. However, a much lesser amount of ice crystals and also larger ice crystals and liquid droplets are found in the COALESC clouds in comparison to the AIDA clouds and the ice fraction (see Figures 5.4(a), 5.4(b) and 5.6) is far from complete glaciation, which is expected in the WBF regime.

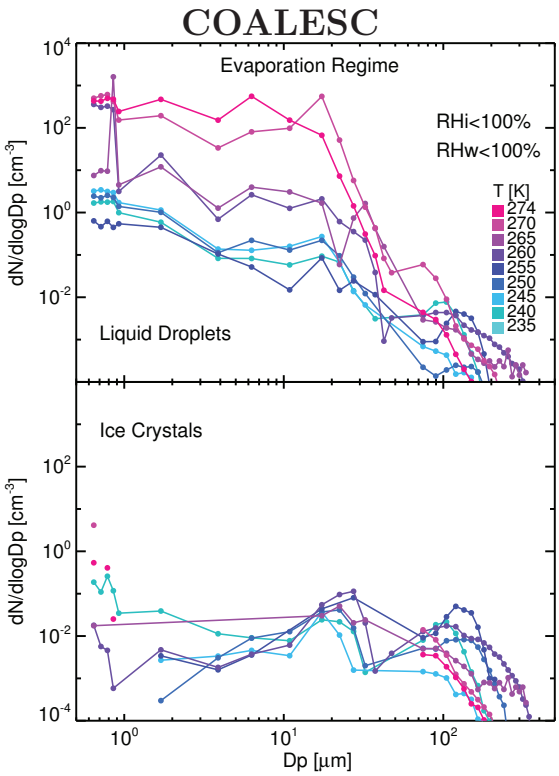

Figure 5.9.: Same as Figure 5.7(a) and 5.7(b) but for the natural mixed-phase clouds observed during the COALESC campaign in the evaporation regime.

5.4. Discussion

A number of questions arise from the observations of mixed-phase cloud glaciation presented in the last sections. The most interesting are: Is a dynamic influence detectable in the AIDA or COALESC cloud datasets and does the initial aerosol play a role? Which of the two influences dominates? Why do the microphysical characteristics of the COALESC natural and AIDA clouds respond differently?
Before discussing the microphysical properties observed in this thesis, they are compared to other mixed-phase cloud observations.

Observations in the context of current knowledge

AIDA clouds in the subsaturated WBF humidity regime were observed to develop into a mostly glaciated state, while the liquid phase dominated the AIDA clouds in the coexistence humidity regime and all observed COALESC clouds (see Section 5.2). Similarly, Korolev and Isaac (2003a) concluded that in general one phase (liquid or ice) dominates in mixed-phase clouds.
For the COALESC natural clouds (Figure 5.8(a),5.8(b) and 5.9), a decrease of the droplet size distribution with temperature is observed. In contrast, the ice size distribution does not show a comparably large decrease. Thus, the total cloud particle concentration is dominated by liquid droplets and decreases with temperature (see Figure 5.10 upper left panel, green curves) in agreement with the total droplet concentrations observed by Korolev and Isaac (2003a).
It is also evident from Figure 5.8(a) that the liquid droplet concentration in the COALESC clouds is dominated by small droplets with sizes up to 20 µm. For temperatures between −5 °C and −25 °C (268 K and 248 K), the concentration of the small liquid droplets ranges from 1 cm^{-3} to 100 cm^{-3}. In that temperature interval, McFarquhar and Cober (2004) analogously found a large amount (up to 10 cm^{-3}) of small cloud particles up to 15 µm in their liquid-dominated clouds. In Figure 5.8(a), the ice crystal size distribution in the temperature range −5 °C and −25 °C is more evenly distributed with concentrations up to 1 cm^{-3}. In their ice dominated cloud observations McFarquhar and Cober (2004) additionally detected a slight minimum at around unit10µm which is not as evident in the measurements presented here. In addition, the largest detected cloud particles are a few hundred µm in diameter which is considerably smaller than the largest particle sizes (larger than 1000 µm) observed by McFarquhar and Cober (2004). However, this discrepancy might be partly due to the deployed instrumentation. The NIXE-CAPS instrument can only detect particles as large as 937.5 µm in diameter. The advantage of the instrumentation used for this thesis in comparison to McFarquhar and Cober (2004) is that here a quantitative detection of the liquid droplet and ice crystal concentration is possible. Whereas McFarquhar and Cober (2004) could only qualitatively classify mixed-phase clouds in the category mostly liquid, mostly glaciated or mixed-phase.

The total ice number concentrations observed in the COALESC natural clouds in Figure 5.10 (upper right panel, light and dark green curve) are displayed in dependence on temperature. In general, the observed total ice crystal concentrations are low and increase slightly with decreasing temperature. The comparison to the measurements of IN concentration by DeMott et al. (2010) (see Chapter 2.1.2, Figure 2.5) indicate a surprisingly good agreement, especially when taking into account the completely different measurement approaches. DeMott et al. (2010) determined the IN concentration from measurements of aerosol particles whereas in this thesis the ice crystal concentration is detected through direct cloud particle measurements. From this comparison it can also be concluded that neither secondary ice production nor severe shattering of ice crystals (and successful removal of the remaining shattering events) in the COALESC clouds took place.

5.4.1. Aerosol and dynamic impact on mixed-phase cloud glaciation

The apparent differences of the microphysical properties and the degree of glaciation in the AIDA clouds and the COALESC natural stratocumulus clouds described in the last sections are most probably caused by either varying dynamic and/or aerosol conditions. The present thesis is dedicated to explore the importance of each contribution to the mixed-phase cloud microphysical properties. An overview of these properties is given in Figure 5.10.

To highlight the difference between the two observed cloud types (AIDA and COALESC

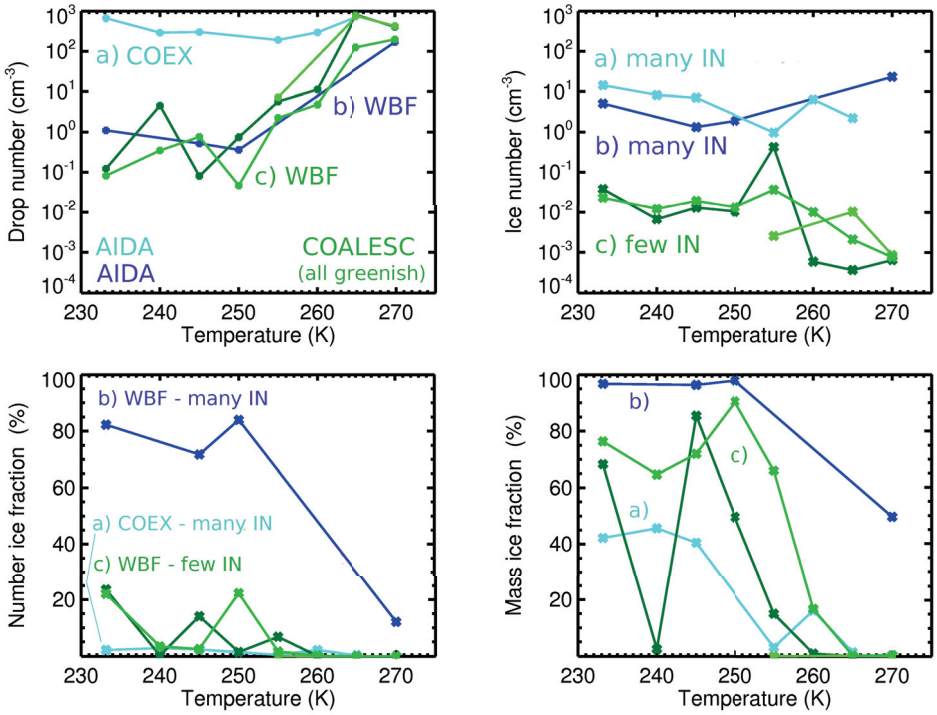

Figure 5.10.: Temperature dependence of average total droplet and total ice crystal concentration (top left and right panel), number ice fraction (bottom left panel) and mass ice fraction (bottom right panel) for mixed-phase clouds observed in the AIDA chamber in a) Wegener-Bergeron-Findeisen (WBF, dark blue) or b) coexistence (coex, light blue) humidity regimes or c) COALESC natural mixed-phase clouds (green). The data is averaged into 5 K temperature intervals.

natural clouds) and humidity regimes (WBF and coexistence regime), the average total droplet and ice number concentrations are shown in the upper left and right panels of Figure 5.10 in dependence on temperature. Concentrating on the two AIDA cloud types (light and dark blue lines), it becomes obvious that the AIDA clouds evolved in the WBF regime (dark blue curve) in general contain less liquid droplets than those in the coexistence region (light blue curve). The total droplet concentration in the WBF regime decreases with temperature. In contrast, the average drop concentration in the coexistence regime shows no dependence on temperature. The temperature dependence of the liquid droplet total number concentration is probably caused by the increasing difference between ice and liquid saturation pressure $e_{s,i} - e_{s,w}$ with decreasing temperature as already mentioned in Section 5.2. The evaporation rate of liquid droplets in the vicinity of ice crystals depends on the interchange of water molecules between the different cloud particle types and the gas phase. The temperature independence of the droplet concentration in the coexistence regime is due to the fact that droplets and ice crystals exist in a supersaturated environment. Thus liquid droplets can be maintained independently of the increasing difference between $e_{s,i}$ and $e_{s,w}$ with decreasing temperature. Hence, the completely different behavior of the droplet concentrations in the WBF and coexistence regime is clearly caused by the thermodynamic environmental conditions.

No obvious differences of the total droplet concentrations are observed for the COALESC natural clouds in the different regimes (Figure 5.10 upper right panel, light and dark green curves). As already mentioned in Section 5.2, we suspect that the relative humidity measurements on board of the BAE146 are inadequate. On the other hand, the COALESC clouds show the same temperature trend as the AIDA clouds in the WBF regime. Therefore, are all classified to the latter regime. Consequentially, the question arises if the total ice crystal concentration and thus the degree of glaciation is also mainly influenced by the dynamic system. Or does the number of ice active aerosol plays a role on the mixed-phase cloud glaciation?

To answer this question, the total ice concentrations of the COALESC natural and AIDA chamber clouds in the different humidity regimes are displayed in the upper right panel of Figure 5.10. First of all, no dependence of the total ice concentration on temperature is obvious for the AIDA clouds, while a slight increase of the total ice crystal concentration with decreasing temperature is seen for the COALESC clouds. Furthermore, no difference in total ice crystal concentration between clouds of the same cloud type (AIDA or COALESC) but evolved in different humidity regimes is observable. Rather the total ice concentrations of the AIDA clouds is two orders of magnitude higher than these of the COALESC natural clouds. It is clear that the ice crystal concentration reflects the number of IN (see Section 5.4). Obviously a very high number of IN are dispersed in the AIDA chamber in comparison to the atmosphere, represented by the COALESC ice crystal numbers. Thus, in contrast to the drop concentration, the ice crystal concentration is driven by the aerosol particles.

But this is not the only difference between the AIDA and COALESC natural clouds. Remembering the COALESC natural and AIDA cloud size distributions (Figures 5.7(a), 5.7(b), 5.8(a), 5.8(b) and 5.9), the droplet and ice spectra especially for the large cloud

particles differ significantly.
The droplets of the AIDA clouds do not grow to sizes larger than approximately 20 µm.Thus, all ice crystals originate from droplets with diameters between 10 µm to 20 µm. The frozen droplets then grow to larger sizes. A result is that the large cloud particles are all frozen and the ice fraction for sizes larger than 40 µm is 1 (compare Figure 5.7(b)). Additionally, many IN are dispersed in the AIDA chamber. Therefore, a large fraction of the droplets contain active IN and thus the degree of glaciation for clouds in the WBF regime is high. In summary, these mixed-phase clouds consist of a narrow droplet size spectrum with no droplets growing to sizes larger than 50 µm and thus reaching precipitation size. This type of cloud is thus non-precipitating and glaciates completely in the WBF regime. This can also be seen in Figure 5.10 (blue curve in the lower left and right panels), where the number and mass ice fractions are shown in dependence on temperature. The AIDA clouds in the WBF regime have the highest degree of glaciation. This is triggered by the high number of IN. In the AIDA chamber, the decrease of the ice number and mass ice fraction (lower left and right panels in Figure 5.10) with increasing temperature is caused by the droplet concentration (upper left panel in Figure 5.10), which is thermodynamically controlled. Altogether, the degree of glaciation, either expressed by number or mass ice fraction, is determined by both initial aerosol and cloud dynamics.
Contrary, in the COALESC natural mixed-phase clouds in the WBF regime, the liquid droplets grow to drizzle size (Figure 5.8(a)). Predominantly the largest droplets freeze. The reason for the different development of the COALESC clouds cannot be discussed here, since the temporal evolution of the droplet spectra is not known. In contrast to the AIDA experiments, in the COALESC natural clouds the ice fraction does not reach 1 (Figure 5.10, green curves in the lower panels). This is because the low IN concentration during the COALESC measurement period causes only a small part of the droplets to freeze (Figure 5.10, green curves in the lower panels). Nevertheless, since the large droplets freeze first, the mass ice fraction is only slightly smaller than for the AIDA clouds in the WBF regime (lower right panel in Figure 5.10). These types of clouds clearly demonstrate the effect of IN number on the degree of glaciation. It is especially remarkable that due to the low IN number a coexisting of droplets and ice crystals is possible although the clouds are in the WBF regime.
The last cloud type observed in this thesis are the AIDA clouds in the coexistence regime (light blue curves in Figure 5.10). Due to the high number of droplets over the whole temperature region (upper left panel in Figure 5.10), they show only a low degree of glaciation (lower panels in Figure 5.10) despite the high IN concentration (upper right panel in Figure 5.10). Here, the influence of the cloud dynamics greatly exceeds the influence of high IN numbers.
In summary, the above observations indicate that if a large number of active IN is available, the degree of glaciation in the mixed-phase clouds is influenced by the dynamic situation. On the other hand, if the available number of active IN is limited, the glaciation in the mixed-phase clouds is suppressed even if the dynamic situation is beneficial for a complete glaciation. These results are the experimental evidence of the recent model studies by Ervens et al. (2011), who numerically showed that the glaciation can be influenced both by

the cloud dynamic situation as well as aerosol effects. The model studies indicate that, in agreement with the results presented here, even for beneficial thermodynamic situations, plenty of active aerosol is needed before a complete glaciation of the mixed-phase cloud takes place.
The lower right panel in Figure 5.10 displays the mass ice fraction for the two AIDA and COALESC natural cloud types in the WBF and coexistence regime in dependence of temperature. Not surprising, the mass ice fraction is highest for the AIDA cloud in the WBF regime and decreases with increasing temperature. The AIDA clouds in the coexistence regime on the other hand on average exhibit the lowest mass ice fraction. Astonishingly, the COALESC natural clouds show higher mass ice fractions than the AIDA clouds in the coexistence regime. This apparent contrast in Figure 5.10 can be resolved when taking the ice crystal size distributions in Figure 5.8(a) into account. Although the ice crystal concentration in the COALESC natural clouds is low, the ice crystals are large in size and thus the mass ice fraction is higher than in the AIDA clouds in the coexistence regime which only exhibit small ice crystals.

6. Summary and conclusions

This thesis explored the glaciation process in mixed-phase clouds. To access the cloud particle phase and concentration in the whole cloud particle size spectrum, in a first step the new cloud particle spectrometer NIXE-CAPS (Novel Ice EXpEriment - Cloud and Aerosol Particle Spectrometer) was taken into operation. This new instrument resembles the established CAPS and for this thesis, was equipped with a new polarization detector to measure the cloud particle shape on a single particle basis. In the frame of this thesis, mixed-phase clouds were investigated at the AIDA cloud chamber in 144 experiments during four measurement periods between 2008 and 2010. Additionally, natural clouds were observed during 16 flights with the British aircraft BAE146 in the course of the airborne field campaign COALESC over the UK in 2011. For the first time, extensive size and phase resolved in-situ mixed-phase cloud observations were performed. The aim of this thesis was to study the mixed-phase cloud evolution in different humidity and temperature regimes to better understand the interplay of dynamical and aerosol effects on mixed-phase cloud glaciation.

NIXE-CAPS accurately detects the size, concentration and form of cloud particles in the size range of 0.61 µm to 937.5 µm. The newly developed shape detection algorithm on the basis of polarization and scattering measurements was applied for the first time and proved to be an essential tool for the detection of microphysical properties in mixed-phase clouds. Before the operation in the field, the NIXE-CAPS underwent a number of tests and comparisons to other instruments under controlled conditions at the AIDA chamber and overall proved to accurately operate in its stated measurement range. Further, an extensive data evaluation library was developed to process the raw output of the instrument.

An influence of the environmental humidity on the microphysical properties of mixed-phase clouds could clearly be confirmed by the AIDA chamber measurements. In the subsaturated Wegener-Bergeron-Findeisen regime[1] in general a high cloud glaciation was observed, whereas in the coexistence regime[2] the glaciation was much lower. The degree of glaciation varied in the two humidity regimes due to the different evolution of the cloud droplet concentrations. The total liquid droplet concentration of AIDA clouds in the co-

[1] Wegener-Bergeron-Findeisen regime: $RH_w < 100$ % and $RH_i \geq 100$ %

[2] Coexistence regime: $RH_w \geq 100$ % and $RH_i \geq 100$ %,
$RH_{w;i}$: relative humidities with respect to liquid (w) and ice (i)

existence regime on average was high in the whole temperature range, whereas the droplet concentration of clouds in the Wegener-Bergeron-Findeisen regime had about the same droplet concentration near 0 °C, but rapidly decreased with temperature. Overall, the droplet concentration seemed to be mainly driven by the dynamic situation. The decrease of the droplet concentration with temperature was probably caused by the increasing difference of the liquid and ice saturation pressure. In contrast, the ice crystal concentrations of the AIDA clouds were rather high and did not vary with temperature. This was most likely caused by the initially high ice active aerosol concentrations injected into the chamber.
The droplet spectra observed in the COALESC natural clouds were quite similar to those observed in AIDA clouds in the Wegener-Bergeron-Findeisen regime. Contrary to the AIDA observations, the COALESC clouds classified into the different humidity regimes did not show any differences in the droplet concentrations. We assume that the humidity classification scheme based on the water measurements on board the BAE146 was inadequate and that most of the natural COALESC clouds were encountered in the Wegener-Bergeron-Findeisen regime. The number ice fraction observed in the natural clouds was on average low compared to the AIDA clouds in the Wegener-Bergeron-Findeisen regime. Also, the total ice concentration in the natural clouds was two orders of magnitude lower than in the AIDA clouds, which is most probably due to the limited availability of ice nuclei in the atmosphere.
Overall, the experiments impressively demonstrate the interaction of relative humidity and aerosol properties on mixed-phase cloud glaciation. If a large number of active ice nuclei is present, then the mixed-phase cloud glaciation is driven by the cloud dynamics. A low concentration of ice nuclei, on the other hand, can efficiently suppress freezing, even if the thermodynamic situation is beneficial.

6.1. Outlook

One important aspect to improve the findings of this thesis is to deploy faster and more accurate hygrometers in future airborne campaigns. It has been shown here that the classification of mixed-phase clouds to different humidity regimes is crucial for the understanding of the mixed-phase cloud microphysical properties.
Another aspect which is worth taking into account in future studies is the impact of the initial aerosol on the mixed-phase cloud glaciation. Therefore, aerosol measurements prior to each AIDA experiment or prior to mixed-phase cloud encounters during the COALESC campaign could be related to the amount of frozen cloud particles in the mixed-phase clouds. Thus, a quantification of the aerosol influence on the evolution of these clouds could be obtained.
Finally, this thesis indicates that the glaciation process in mixed phase clouds is a complex interplay between dynamic and aerosol influences. The here presented results are limited to one spatial and temporal location, though. A larger dataset would help to quantify the

importance of both freezing regimes (Wegener-Bergeron-Findeisen and coexistent regime) in mixed-phase clouds. Up to now, conclusions can only be drawn for a specific set of meteorological conditions. Further studies in other than stratocumulus mixed-phase clouds are planned in 2012. Airborne experiments in the Canadian Arctic as well as ground based measurements at the German mid-latitude mount Zugspitze will be performed.

A. Appendices

A.1. AIDA experiment overview

Campaign	Exp. No.	Aerosol	T start
HALO02	2	GfG soot	−28 °C
HALO02	3	GfG soot	−28 °C
HALO02	4	GfG soot	−28 °C
ACI03	2	AD2	−20 °C
ACI03	3	AD2	−20 °C
ACI03	5	min OC CAST soot	−23 °C
ACI03	6	min OC CAST soot+AD2	−23 °C
ACI03	7	AD2+SOA	−22 °C
ACI03	8	AD2+SOA+min OC CAST soot	−22 °C
ACI03	9	AD2 coated with SOA	−22 °C
ACI03	10	AD2 coated with SOA+min OC CAST soot	−22 °C
ACI03	11	AD2 coated with SOA	−22 °C
ACI03	12	AD2 coated with SOA+min OC CAST soot	−22 °C
ACI03	31	SD2	−22 °C
ACI03	33	outside aerosol	−10 °C
ACI03	34	outside aerosol+SD2	−10 °C
ACI03	36	outside aerosol	−20 °C
ACI03	39	SD2 coated with SOA	−22 °C
ACI03	40	SD2 coated with SOA	−22 °C
ACI03	41	SD2 coated with SOA+min OC CAST soot	−22 °C
ACI03	43	outside aerosol	−30 °C
ACI03	44	AD2	−30 °C
BI05	2	B1	−5 °C
BI05	4	B2	−5 °C
BI05	5	B2	−5 °C
BI05	7	B2	−2 °C
BI05	8	B2	−2 °C

Campaign	Exp. No.	Aerosol	T start
BI05	10	B2	2 °C
BI05	13	snowmax	−5 °C
BI05	16	B3	−3 °C
BI05	17	B3	−3 °C
BI05	19	B1	−3 °C
BI05	20	B2	−3 °C
BI05	22	B3	−3 °C
BI05	23	B3	−3 °C
BI05	25	B3	−3 °C
BI05	26	B3	−3 °C
BI05	29	B3+ATD	−3 °C

Table A.1.: Overview of the AIDA experiments used for this study, as well as the AIDA experiment start temperature and the injected aerosol.

A.2. COALESC flight overview

Exp. No.	T range	Description
1	−63 °C - 10 °C	test flight
2	−63 °C - 10 °C	cirrus
3	−5 °C - 10 °C	stratocumulus
4	−45 °C - 10 °C	stratocumulus
5	−10 °C - 10 °C	stratocumulus
6	−10 °C - 10 °C	stratocumulus
7	−5 °C - 10 °C	stratocumulus
8	−5 °C - 10 °C	stratocumulus
10	−63 °C - 10 °C	cirrus
11	−5 °C - 10 °C	stratocumulus
13	−63 °C - 10 °C	cirrus
14	−5 °C - 10 °C	stratocumulus

Table A.2.: Overview of the COALESC experiments used for this study, as well as the sampled temperature range and the measured cloud type.

A.3. NIXE-CAS

The electro-optical design of the Novel Ice EXpERiment - Cloud and Aerosol Spectrometer (NIXE-CAS) instrument is described in detail in Section 3.1. Here, certain aspects regarding the operation of the NIXE-CAS instrumentation as well as a theoretical background on single particle scattering is given to deepen the readers knowledge.

A.3.1. CAS A/D count conversion

The intensities measured by the NIXE-CAS instrument are amplified and digitized in different stages to better resolve the size regions of interest. The scattered intensity is thus internally converted into an analog to digital (A/D) value, from here on called analog to digital (A/D) count. The A/D values can range from 0 to 12287. For the forward scattered light three different gain stages exist, where each is applied depending on the forward scattered intensity. For the perpendicular polarized component of the backscattered intensity only one gain is applied to the whole intensity range whereas for the total backward scattered light two gain stages exist.
The A/D counts are coded to be able to distinguish the different gain stage operations. The decoding of all A/D counts between 3072 and 6143 is described in Equation A.1 and the decodings of all counts between 6144 and 9216 is specified in Equation A.2.

$$\mathrm{AD_{FWD}} = (\mathrm{AD_{CODED}} - 3072) \cdot 22 \tag{A.1}$$

$$\mathrm{AD_{FWD}} = (\mathrm{AD_{CODED}} - 6144) \cdot 506 \tag{A.2}$$

where $\mathrm{AD_{CODED}}$ describes the coded A/D counts and $\mathrm{AD_{FWD}}$ the uncoded A/D counts. The amplification rates are 22 and $22 \cdot 23$.

A.3.2. Particle size determination - Theory

The concept of the NIXE-CAS particle size measurement is based on the Mie scattering theory for spherical particles. The Mie theory solves the wave equations for the electric field which are derived from Maxwell's equations (cf Bohren and Huffman (1998)). The differential wave equation of the electric field vector is simplified by reducing it to a problem of solving a scalar differential equation. A spherical coordinate system is then introduced and the scalar wave equation is separated into three different functions each only dependent on one of the spherical coordinates ϕ, θ and r. These functions can then be solved by making use of Bessel functions and Legendre polynomials. The electric field vector can thus also be expanded in Bessel and Legendre polynomials. Finally, the electric field vector is separated into its polarization components with respect to the spherical coordinate system. The

dependence of the incident and scattered electrical field amplitudes can be calculated by Equation A.3.

$$\begin{pmatrix} \mathrm{E}_{\parallel \mathrm{s}} \\ \mathrm{E}_{\perp \mathrm{s}} \end{pmatrix} = \frac{\exp\left(i\mathrm{k}\left(\mathrm{r_d}-\mathrm{z}\right)\right)}{-i\mathrm{kr_d}} \begin{pmatrix} \mathrm{S}_2 & \mathrm{S}_3 \\ \mathrm{S}_4 & \mathrm{S}_1 \end{pmatrix} \begin{pmatrix} \mathrm{E}_{\parallel \mathrm{i}} \\ \mathrm{E}_{\perp \mathrm{i}} \end{pmatrix} = \frac{\exp\left(i\mathrm{k}\left(\mathrm{r_d}-\mathrm{z}\right)\right)}{-i\mathrm{kr_d}} \mathbb{S} \begin{pmatrix} \mathrm{E}_{\parallel \mathrm{i}} \\ \mathrm{E}_{\perp \mathrm{i}} \end{pmatrix} \tag{A.3}$$

where $\mathrm{E}_{\parallel \mathrm{s}}$, $\mathrm{E}_{\perp \mathrm{s}}$,$\mathrm{E}_{\parallel \mathrm{i}}$ and $\mathrm{E}_{\perp \mathrm{i}}$ are the scattered and incident parallel and perpendicular electrical field components with respect to the spherical coordinate system, k is the wave vector, $\mathrm{r_d}$ is the radial distance between particle origin and observer and S_1 to S_4 are the components of the amplitude scattering function. The exact relation between the amplitude function elements and the Bessel functions and Legendre polynomials can be found in Bohren and Huffman (1998). The matrix $\mathbb{S}$ describes the relative energy flux per solid angle dependent on the scattering angle.
For spherical particles, the amplitude scattering matrix reduces to two independent elements:

$$\begin{pmatrix} \mathrm{E}_{\parallel \mathrm{s}} \\ \mathrm{E}_{\perp \mathrm{s}} \end{pmatrix} = \frac{\exp\left(i\mathrm{k}\left(\mathrm{r_d}-\mathrm{z}\right)\right)}{-i\mathrm{kr_d}} \begin{pmatrix} \mathrm{S}_2 & 0 \\ 0 & \mathrm{S}_1 \end{pmatrix} \begin{pmatrix} \mathrm{E}_{\parallel \mathrm{i}} \\ \mathrm{E}_{\perp \mathrm{i}} \end{pmatrix} = \frac{\exp\left(i\mathrm{k}\left(\mathrm{r_d}-\mathrm{z}\right)\right)}{-i\mathrm{kr_d}} \mathbb{S}_{\mathrm{sphere}} \begin{pmatrix} \mathrm{E}_{\parallel \mathrm{i}} \\ \mathrm{E}_{\perp \mathrm{i}} \end{pmatrix} \tag{A.4}$$

A detailed description of a way to model the scattering by spherical particles is given by Bohren and Huffman (1998). This technique is implemented in the Jülich evaluation program.

The NIXE-CAS particle size measurement is based upon measuring the total intensity scattered into the forward direction. The total intensity measured at a specific angle can be related to the incident intensity of the laser beam by Equation A.5.

$$\mathrm{I_s} = \mathrm{E}_{\parallel \mathrm{s}}\mathrm{E}^*_{\parallel \mathrm{s}} + \mathrm{E}_{\perp \mathrm{s}}\mathrm{E}^*_{\perp \mathrm{s}} = \frac{\sigma_\mathrm{i}}{\mathrm{r_d}^2}\mathrm{I_i} \tag{A.5}$$

σ_i is the differential scattering cross section and $\mathrm{I_s}$ is the measured intensity at the detector position.
The differential scattering cross section depends on the particle shape and the observer position:

$$\sigma_\mathrm{i} = \frac{1}{\mathrm{k}^2} \int_{0^\circ}^{360^\circ} \int_{\theta_1}^{\theta_2} \frac{1}{2}\left(\left|\mathrm{S}_1\right|^2 + \left|\mathrm{S}_2\right|^2\right) \sin\left(\theta\right) d\theta d\phi = \frac{1}{\mathrm{k}^2} \int_{0^\circ}^{360^\circ} \int_{\theta_1}^{\theta_2} \mathrm{Z}_{11} \sin(\theta) d\theta d\phi \tag{A.6}$$

where $\theta_1 = 4^\circ/\theta_1 = 168^\circ$ and $\theta_2 = 12^\circ/\theta_2 = 176^\circ$ are the restricting angles for the forward and backward observer positions, $\mathrm{Z}_{11} = \frac{1}{2}\left(\left|\mathrm{S}_1\right|^2 + \left|\mathrm{S}_2\right|^2\right)$ and S_1 and S_2 are dependent on the size, shape and refractive index of the particle as described above. The incident NIXE-CAS laser intensity is assumed to be constant.

NIXE-CAS does not directly measure σ_i but the detectors and the electronic amplification system output analog to digital (A/D) counts (see Section 3.1.1 and A.3.1) that are related to the measured intensity. The relation between σ_i and the analog to digital (A/D) counts can be determined by calibration.

A.3.3. Particle shape determination

From the intensity measurements of light scattered by cloud particles, not only the particle size but also the asphericity of the particles can be deduced. On the basis of the particles asphericity, a distinction between spherical water droplets and aspherical ice particles is possible. This is based on additional information on the polarization state of the scattered light. For the detection of the particles asphericity, the polarized components of the scattered light are usually measured in backward direction because the scattering in that direction is influenced by the particle shape. For the NIXE-CAS setup, the initial laser light is polarized linearly and the scattered cross-polarized component, which is the perpendicularly polarized component to the polarization state of the incident laser light, is detected. Furthermore the total backscattered light is recorded.

Theoretically, the incident and scattered polarization components can be visualized by the Stokes vector:

$$\begin{pmatrix} \mathrm{I} \\ \mathrm{Q} \\ \mathrm{U} \\ \mathrm{V} \end{pmatrix} = \begin{pmatrix} \mathrm{E}_{\parallel}\mathrm{E}_{\parallel}^{*} + \mathrm{E}_{\perp}\mathrm{E}_{\perp}^{*} \\ \mathrm{E}_{\parallel}\mathrm{E}_{\parallel}^{*} - \mathrm{E}_{\perp}\mathrm{E}_{\perp}^{*} \\ \mathrm{E}_{\parallel}\mathrm{E}_{\perp}^{*} + \mathrm{E}_{\perp}\mathrm{E}_{\parallel}^{*} \\ i\left(\mathrm{E}_{\parallel}\mathrm{E}_{\perp}^{*} - \mathrm{E}_{\perp}\mathrm{E}_{\parallel}^{*}\right) \end{pmatrix} = \begin{pmatrix} \mathrm{I}_{\mathrm{tot}} \\ \mathrm{I}_{\parallel} - \mathrm{I}_{\perp} \\ \mathrm{I}_{+} - \mathrm{I}_{-} \\ \mathrm{I}_{\mathrm{R}} - \mathrm{I}_{\mathrm{L}} \end{pmatrix} \tag{A.7}$$

where I,Q,U and V are the Stokes components. $\mathrm{I}_{\mathrm{tot}}$, $\mathrm{I}_{\parallel}$,$\mathrm{I}_{\perp}$,I_{+},I_{-},I_{R} and I_{L} are the total, parallel and perpendicular polarized intensities with respect to the spherical coordinate system, the by $-45°$ and $45°$ rotated polarized intensity components and finally the right-circularly and left-circularly polarized components. The polarization state of each electromagnetic wave can be represented by a Stokes vector. The degree of linear polarization $\mathrm{P_l}$ is defined by:

$$\mathrm{P_l} = -\frac{\sqrt{\mathrm{Q}^2 + \mathrm{U}^2}}{\mathrm{I}} \tag{A.8}$$

The scattering of light can also be represented in the Stokes regime (see Equation A.9; Mishchenko et al. (2000, 2005) and Bohren and Huffman (1998)):

$$\begin{pmatrix} I_s \\ Q_s \\ U_s \\ V_s \end{pmatrix} = \frac{1}{k^2 {r_d}^2} \mathbb{Z} \begin{pmatrix} I_i \\ Q_i \\ U_i \\ V_i \end{pmatrix} \tag{A.9}$$

The scattered and incident intensities of the polarization components are related by the phase function $\mathbb{Z}$. The elements of the phase function $\mathbb{Z}$ can be related to the elements of the amplitude function $\mathbb{S}$. The conversion from the phase to the amplitude matrix is described in Mishchenko et al. (2000, 2005) and Bohren and Huffman (1998). As the phase matrix can be constructed from the elements of the amplitude matrix, the exact form of the matrix elements is also dependent on particle radius, form, orientation and observer position. Due to particle symmetries the phase function for spherical particles, presented in the spherical coordinate system, reduces to four independent elements:

$$\mathbb{Z}_{sphere} = \begin{pmatrix} S_{11} & S_{12} & 0 & 0 \\ S_{12} & S_{22} & 0 & 0 \\ 0 & 0 & S_{33} & S_{34} \\ 0 & 0 & S_{34} & S_{33} \end{pmatrix} \tag{A.10}$$

But why does the polarization state of light scattered by aspherical particles differ from that scattered by spherical particles? Aspherical particles that scatter light alter the polarization state due to internal reflections of the light on the particle lattice. Furthermore, electric dipoles are induced within the particle when the particles are exposed to external electric fields. Bends and edges in the particle surface can influence the strength and orientation of the electric dipoles and thus alter the state of polarization of the re-emitted light waves.

The polarization state of laser light that initially is completely polarized perpendicular or parallel in the spherical coordinate system, does not change upon scattering by spherical particles (compare Equations A.9 and A.10). The NIXE-CAS laser light is initially polarized linearly within the laboratory system. Light, which is polarized parallel with respect to the laboratory system, has parallel and perpendicular components when transformed into a spherical coordinate system. Thus, the scattered light in the spherical coordinate system also has parallel and perpendicular components. The scattering of the perpendicular and parallel polarized components into one observer direction is different. To evaluate the polarization state of the NIXE-CAS laser light upon scattering, the scattered intensities then have to be transformed back into the laboratory reference frame. For spherical particle scattering, no change in the state of the light polarization would be detected from observer points along the azimuthal line $\phi = 0°$ and arbitrary θ positions (see Pal and Carswell (1985)). In contrast, light scattered by aspherical particles would generate a change in the laser light polarization when observed at these positions. Unfortunately, the NIXE-CAS detector is no point in space. Rather the detectors cover an angular range in polar θ and

azimuthal ϕ direction. For observer positions $\phi \neq 0°$, a change in the laser light polarization is expected even for scattering by spherical particles (compare Pal and Carswell (1985)). Thus, the detection of a small amount of cross polarized light is expected to be detected even for scattering by spherical particles when observed with the NIXE-CAS instrumental setup due to the dimensions of the NIXE-CAS detector measuring the cross-polarized component of the scattered light.
Nicolet et al. (2007) used T-matrix calculations to evaluate the change of the polarization state of light upon scattering by aspherical particles in dependence of the particle (in that case a circular cylinder) orientation. They found out that the expected scattered polarized amplitudes varied depending on the particle orientation. The numerical calculations are only performed for observer positions at exactly 180° and thus are not directly comparable to the NIXE-CAS optical setup. Nevertheless, for single ice crystal measurements, a distribution of different polarization states of the scattered light is expected even for the NIXE-CAS optical setup due to different particle orientations.

The technique of measuring two polarized components of the backscattered light is already successfully adopted in LIght Detection And Ranging (LIDAR) systems and LIDAR observations thus provide a guideline for similar measurement techniques. LIDAR systems direct a polarized laser beam into the sky. The light scattered by aerosol and cloud particles are measured at the exact backward direction with two detectors. In that way informations about the phase of the particles are obtained. To be able to compare the NIXE-CAS measurements to lidar systems which normally perform measurements on an ensemble of particles rather than on single particles, the bulk linear depolarization value needs to be calculated from the NIXE-CAS measurements:

$$\delta_l = c \cdot \frac{I_\perp}{I_{ges} - c \cdot I_\perp} \tag{A.11}$$

To obtain δ_l, the two backward measuring detectors need to be calibrated to each other. One method employed is to use Equation A.11 and inter-calibrate the calibration constant c until the best fit to another external measurement is found. Then this calibration constant can be used throughout the whole measurement period. This method is adopted for the HALO02 measurement period. Another method which is not dependent on other external measurements is the use of a spectralon target (Haner and McGuckin, 1997) with known depolarizing characteristics. Such a calibration neglects the NIXE-CAS electronic response characteristics because the target is held permanently into the beam, but the system is optimized for pulse stimulations. Thus, the signal caused by the spectralon target can only be measured at the first amplification stage. The spectralon calibration method is adapted for the ACI03 measurement period.

The LIDAR measurements of the polarization state of light backscattered by aspherical particles provide a background to evaluate the NIXE-CAS measurements. For example

Sassen (1991) determined that the bulk linear depolarization ratio δ_l of water droplets measured by the LIDAR system is lower than 0.1 whereas δ_l for pure ice clouds is larger than 0.45. For mixtures of water droplets and ice crystals, the δ_l values are expected between 0.1 and 0.5 (Sassen (1991)). Sassen and Hsueh (1998), Freudenthaler et al. (1996) and Mishchenko et al. (2000) examined the bulk linear depolarization ratios for different ice crystal shapes experimentally and theoretically. They found different bulk linear depolarization ratios but also almost equal values for different ice shapes. Model studies revealed that the calculated depolarization ratio is also dependent on particle size. Thus a clear shape separation on the basis of only measured bulk linear depolarization ratios is difficult but a shape tendency can be extracted. The studies indicate that the knowledge of cloud particle size might further help to distinguish different crystal types.
The NIXE-CAS shape detection scheme is equivalent to the LIDAR system. Nevertheless, the above mentioned findings can not be completely transfered to the NIXE-CAS system. The largest difference between LIDAR and NIXE-CAS polarization measurements is that LIDAR systems can only measure the mean value of a larger number of cloud particles whereas for NIXE-CAS measurements the polarization of each single cloud particle is detected. The LIDAR system thus measures the average scattering behavior of a particle ensemble whereas the NIXE-CAS detects single particle scattering properties.
This studies, for the first time, uses NIXE-CAS polarization measurements to distinguish liquid droplets and ice crystals. Therefore, a technique has to be developed to separate water droplets from ice crystals on the basis of measurements of the backscattered polarized components.

As explained above, water droplets do not strongly depolarize the incident light. T-matrix calculations for aspherical particles however predict a wide variety of different depolarization values depending on the size and orientation of the sampled ice crystals. This theoretical knowledge is used as starting point to develop a new cloud phase detection algorithm.
The NIXE-CAS measures the intensities of the total and the cross polarized components of the backscattered light. The raw output, however, is no differential scattering cross section but A/D counts (see Section 3.1.1), which are hereafter called total backward and cross polarized A/D counts. For the separation of water droplets and ice crystals on the basis of the NIXE-CAS measurements of forward and backward scattered light, a cloud of water droplets is used as reference. For spherical cloud particles it is expected that the measured cross-polarized component is small. Additionally, either the total backscattered or the total forward scattered intensity is also taken into account, which are sensitive to the particle size. This is based upon the above described LIDAR observations which indicate that the state of the scattered light might also vary with particle size for a given particle habit. Depending on the number of particles within the liquid cloud, either of the two following schemes is executed. In the case that only a limited number of water droplets is available, the measured total backward A/D counts are compared to the ratio of A/D counts of the cross-polarized to the total backscattered light. If a more extensive set of differently sized water droplets is available for calibration, first the size of the particles based upon

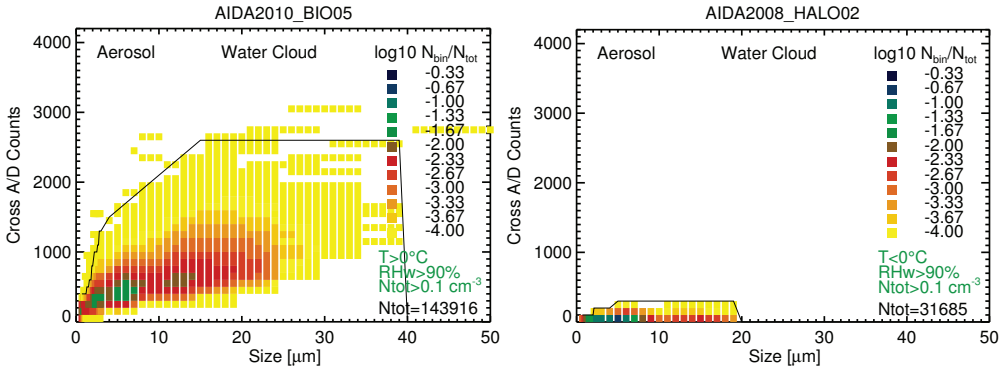

Figure A.1.: Frequency histogram of measured particle sizes vs cross polarized A/D counts, the latter measured by the detector installed in back direction and masked by a polarization filter, for two pure water clouds produced during the HALO02 (experiment 4) and BIO05 (experiment 10) measurement periods. For the two measurement periods different amplification gains are set for the measurement of the cross-polarized component of the backscattered light. The here displayed frequency histograms are used to define a threshold line which separates water droplet and ice crystals.

the measured A/D counts in forward direction and Mie theory is calculated. Then these sizes are compared to the measured cross polarized A/D counts. Figure A.1a displays the cross polarized A/D counts vs size frequency distribution of a pure water cloud obtained during the measurement period ACI03. It is evident that the counts corresponding to the cross polarized component of the backscattered light are size dependent. The larger the particles, the larger are the measured counts of the cross-polarized light component on average. In comparison, Figure A.1b displays the measured A/D counts of the cross-polarized backscattered light vs size frequency histogram for a water cloud measured during the measurement period HALO02. The amplification of the measured cross polarized light component for this measurement period was set lower than for the measurement period ACI03. The NIXE-CAS system was not as sensitive to small amounts of cross polarized light as for the other measurement period. Thus the measured cross polarized A/D counts for water droplets do not show a size dependence and the measured A/D counts in general are small. To distinguish water droplets and ice crystals a threshold line is defined for each measurement period. Alternatively, a threshold dependent on the ratio of the A/D counts of the cross polarized component to the total backscattered light can be identified (cf Figure A.2a). The use of the size vs the cross polarized A/D counts or cross polarized to total backward A/D counts vs total backward counts to separate water droplets and ice crystals do not result in major differences in the amount of classified liquid and ice particles. Thus if possible, the size vs cross method is preferred. All points situated below the threshold lines are classified as spherical, all above as aspherical. A related technique is adopted to separate liquid droplet and ice crystals clouds measured with lidar systems (cf Hu et al., 2007).

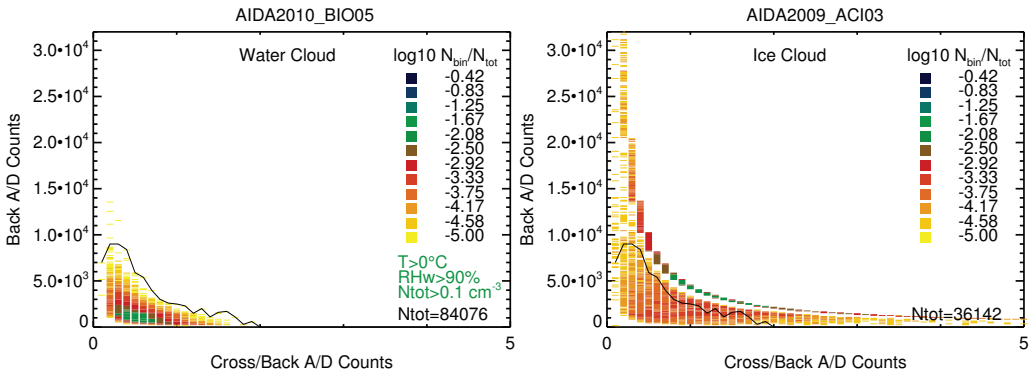

Figure A.2.: Same as Figure A.1, but the threshold between water droplet and ice crystal counts is based upon the cross polarized A/D counts (compare Figure A.1) divided by the total backward A/D counts, the latter measured with the unmasked detector in backward direction. The left graph displays the counts of a pure liquid cloud produced during the experiment 10 of the BIO05 measurement period. The black threshold line is defined from this dataset. The right graph displays a pure ice cloud generated during the ACI03 experiment 22.

The above described methods are not only applicable to measurements of liquid droplets and ice crystals, but also to the aerosol mode measured by NIXE-CAS. In this mode, condensed aerosol particles are distinguished from dry highly aspherical aerosol particles. In comparison to pure water clouds, Figure A.3 displays the cross polarized A/D counts vs size distribution for two ice clouds formed below −38 °C. The threshold line to separate ice crystals from liquid droplets is plotted in black. At this temperature, droplets no longer exist, so that the cloud can clearly be identified to consist of only ice particles. For both measurements, a number of particles are detected at the cross polarized backscattered saturation threshold of the NIXE-CAS amplification system. The particles scatter a cross polarization signal which is larger than the maximum value of the amplification system and thus their signals are set to the saturation value of 4095. In Figure A.3 the saturated counts are aligned along the horizontal line at 4095 cross polarized counts. In Figure A.2b, which displays the frequency histogram of the cross polarized to total backscattered A/D counts vs cross polarized A/D counts, the saturated counts are the points on the curved line above the majority of the colored area. All particles with counts between the threshold (black line) and the saturation line and all particles at the saturation line are classified as ice particles. Thus in ice clouds, some fraction of the cloud particles especially those of smaller size which are located below the threshold line are not unambiguously classified as ice particles.

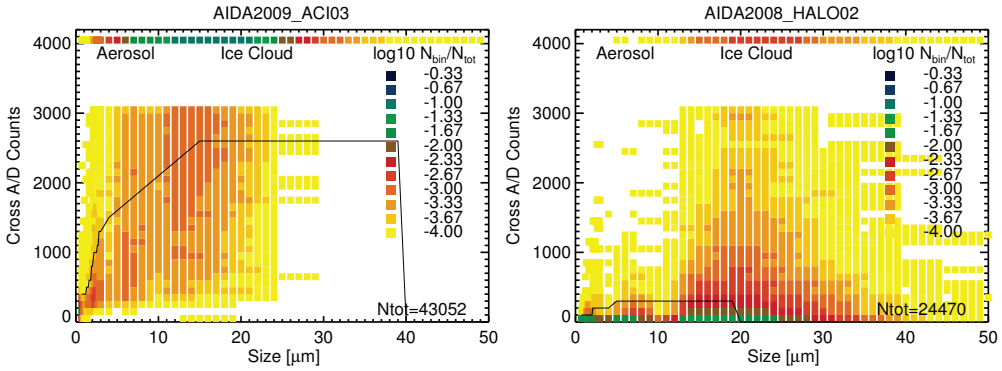

Figure A.3.: Frequency histograms of particle sizes vs A/D counts of the cross polarized backscattered light component (compare Figure A.1) for two pure ice clouds generated during the ACI03 experiment 22 and HALO02 experiments 18. The black line represents the threshold line to distinguish spherical and aspherical particles.

A.4. NIXE-CIP

The electro-optical design of the Novel Ice EXpEriment - Cloud Imaging Probe (NIXE-CIP) instrument is described in detail in Section 3.2. Here, certain aspects of the NIXE-CIP instrumentation are discussed in detail to provide more insight into the instruments operation.

A.4.1. CIP sample volume determination

The determination of the NIXE-CIP sample volume is important to determine the NIXE-CIP number concentration. The mathematical expression of the NIXE-CIP sample volume (SV) is given by Equation A.12 equivalently to Equation 3.1.

$$\mathrm{SV} = \mathrm{DOF} \cdot \mathrm{EAW} \cdot \mathrm{v} \cdot \mathrm{t} \tag{A.12}$$

The sample area (SA) is defined by its length along the laser beam called depth of field (DOF) and the width of the sample area perpendicular to the Depth Of Field (DOF) and air flow, called Effective Array Width (EAW). Unlike for the NIXE-CAS Sample Area (SA), the NIXE-CIP SA depends on the measured particle diameter. The NIXE-CIP EAW can be evaluated by three different methods described in the following.
If one or both of the end diodes of the diode array are shaded a part of the particle lies outside of the depth of field (DOF). Three methods exist to deal with particles only partially contained in the sample volume, the 'reconstructed','center-in', and 'entire-in' methods.
The 'entire-in' analysis (Droplet Measurement Technologies, 2009) includes a rejection of all particles which shade one or both end diodes. The use of this technique is reasonable

when a high concentration of particles smaller than the array width is sampled. The technique should also be applied when highly asymmetric particles pass through the sample volume (SV). No assumptions about the particle symmetry need to be made in this case. The 'entire-in' effective array width (EAW) is defined by:

$$\mathrm{EAW} = \mathrm{RES} \cdot (\mathrm{N} - \mathrm{X} - 1) \tag{A.13}$$

where N is the number of detector elements and X is the number of shadowed elements.
The 'center-in' technique (Heymsfield and Parrish, 1978) can be applied to quasi-symmetric or symmetric particles like raindrops, graupel, hail, dendrites and rimed aggregates whose centers are located within the detector array. The 'center-in' effective array width (EAW) is defined by:

$$\mathrm{EAW} = \mathrm{RES} \cdot \mathrm{N} \tag{A.14}$$

A comparison of the 'entire-in' and 'center-in' Equations A.13 and A.14 reveals that the sample volume (SV) is larger for the 'center-in' technique.
The 'reconstructed' technique (Heymsfield and Parrish, 1978) is preferred over the 'center-in' technique when the sampled particles are symmetric. It provides an even larger sample volume. The width of the diode array is effectively increased by reconstructing particle parts which are positioned outside the diode array. The 'reconstructed' effective array width (EAW) is defined by:

$$\mathrm{EAW} = \mathrm{RES} \cdot \mathrm{N} + 2 \cdot \left(\frac{\mathrm{D_p}}{2} - \frac{\mathrm{D_p}}{7.25} \right) \tag{A.15}$$

where $\mathrm{D_p}$ is the particle diameter.

The depth of field (DOF) is the distance within which the particle can move away from the focal point but still appears acceptably sharp. This is equivalent to only accept a small variation of the image size. For the determination of the DOF the optical setup and interaction between the light beam and the particles need to be taken into account. The shadow of a particle is mapped on the detector array by a collimating lens. The distance between lens and particle (b) and the focus of the lens (f) is definite. To obtain an exact image of the particle, also taking into account the optical magnification, the particle needs to be in its center of field (COF) defined by $\frac{1}{\mathrm{COF}} = \frac{1}{\mathrm{b}} + \frac{1}{\mathrm{f}}$. Particles passing the laser beam exactly at the center of field (COF) will cause a decrease of the light intensity by almost 100 %.
Particles which pass the laser beam away from the Center Of Focus (COF) will decrease the light level to a lesser extent and will cause blurring of the image. This is due to the lens system as well as refraction, reflection, diffraction and absorption of light on the particle object. For the NIXE-CIP measurement technique the diffraction of light is the crucial parameter which has an influence on the image. Knollenberg (1970) estimated the depth of field (DOF) by applying classic far-field diffraction. The Rayleigh criterion defines an

image as sharp if the diffraction maximum of a point source located at the edge of the image coincides with the first diffraction minimum of a point source located at the central point of the image. Thus, in axial direction the optical path difference of the on-axis path between the center of the particle and the DOF edge and the off-axis path between the particle edge and the DOF edge is equal to $\delta - \delta\cos(\theta) = \frac{\lambda}{4}$, where δ is the distance between the center and the edge of the DOF. Expanding $\cos(\theta)$ into a Taylor expansion results in a maximum resolvable path difference proportional to $\frac{\lambda}{\sin^2(\theta)}$. The first diffraction minimum θ of the classical far-field diffraction is given by $\theta = 0.61\frac{\lambda}{\mathrm{r}}$ where λ is the laser wavelength, r the particle radius and θ the angular resolution. Assuming that the angular spreading is small, the depth of field (DOF) is a function of:

$$\mathrm{DOF} \sim \frac{\lambda}{\theta^2} = \frac{\mathrm{r}^2}{\lambda} \tag{A.16}$$

To define the depth of field (DOF) of Optical Particle Counter (OPC)s, Knollenberg (1970) performed measurements with glass beads and opaque disks which he injected at varying distances from the center of field (COF). He concluded that the size of the image deviates by no more than 10 % from the actual particle diameter when the depth of field (DOF) is limited to:

$$\mathrm{DOF} = \frac{3 \cdot \mathrm{r}^2}{\lambda} \tag{A.17}$$

This DOF limitation is technically enforced by accepting only detector elements which are shadowed by more than 50 % for sizing.

A.5. NIXE-CAPS data processing

The primary Novel Ice EXpEriment - Cloud and Aerosol Particle Spectrometer (NIXE-CAPS) output parameters are described in Sections 3.1.1 and 3.2.1. To evaluate the NIXE-CAPS measurements scientifically, these data sets need further processing to reduce the instruments uncertainties. In addition, the NIXE-CAPS output parameters are converted into scientifically useful quantities.
The first step is the synchronization of the time recorded by NIXE-CAPS and the respective platform (Aerosol Interaction and Dynamics in the Atmosphere (AIDA) or aircraft). Therefore, the platform pressure is compared to the measured NIXE-CAPS pressure, especially at pressure changes. The determined shift between the pressure measurements is the drift of the NIXE-CAPS time to the platform time.
A next step is the validation of the NIXE-CAPS velocity, since this is a crucial parameter to determine the sampling volume and thus the particle concentrations. For laboratory experiments normally no NIXE-CAPS air velocity measurements are available and thus the airspeed needs to be evaluated by a different method. For the measurements performed at the AIDA chamber, the method is described in detail in Section 4.2. However, even during

airborne experiments internally measured air velocities might cause a high uncertainty of the NIXE-CAPS measurements depending on the measurement conditions. Thus, instead of the NIXE-CAPS velocity, other more precise externally measured velocities can be assembled.
The housekeeping data of NIXE-CIP and NIXE-CAS do not need to be processed. Nevertheless, plots of the time evolution of the housekeeping data are produced to trace any possible instruments failures.
The primary NIXE-CIP output is stored in two different files types. Possible corrections can only be applied to the image data set. No correction schemes for the already pre-evaluated NIXE-CIP frequency distribution are available.
To deduce the size from the NIXE-CIP image measurements, the SODA software, developed at National Center for Atmospheric Research (NCAR) (Boulder, USA) is embedded into the Jülich evaluation program (see Section A.5.2). The SODA program outputs two data files. The first contains the particles interarrival times (IATs) between successive particles as well as the speed, size and the area of the particles. Pre-evaluated number frequency distributions as well as additional parameters describing the analysis setup are stored within the second file. For the number frequency distribution, several size bins are defined and the particles within the bin limits are counted.
The NIXE-CIP and NIXE-CAS single particle data files, containing information on each individual measured particle, are then edited to produce number frequency histograms. Therefore, for the NIXE-CAS Particle by Particle (PBP) data a maximum of 31 forward scattering A/D thresholds are defined which are related to scattered intensity and thus particle size as described in Section 3.1.3. For the NIXE-CIP PBP data a maximum of 63 size thresholds can be chosen. The size channels are then generated by two successive thresholds. The number of particles in each channel is determined and thus a frequency histogram is generated. One other primary NIXE-CAS and NIXE-CIP data file already offers number frequency histograms.
The unnormalized and normalized size distributions and total number concentrations are calculated for all NIXE-CAPS datasets as described above. The reason why all NIXE-CAPS data files are evaluated although the contained information overlap is that transmission errors sometimes occur which necessitate a cross-check of the data.
After successful post-processing the Jülich evaluation program outputs the data in nasa ames, ncdf or ascii format and produces plots of time series of the particle measurements. Additional comparisons to other instruments can be produced on request.
Corrections need to be applied to each data set to improve the quality of the measurements. These correction schemes are described in the following sections.

A.5.1. NIXE-CAS

Corrections applied to the NIXE-CAS dataset concern cloud particle shattering, particle coincidences in the laser beam and scattering ambiguities.

Cloud particle shattering:
During aircraft operation, particles may hit the NIXE-CAS sample tube edges. This can lead to shattering of the particles into a high number of smaller fragments. These particle pieces may reach the NIXE-CAS sample volume and falsify the particle number size concentration. Field et al. (2003), Korolev and Isaac (2005), McFarquhar et al. (2007) and Heymsfield (2007) and others evaluated the influence of the shattered artifacts on cloud particle measurements. They came to the conclusion that, depending on the cloud conditions, shattering effects may lead to a significant oversampling of small particles up to a factor of 5. However, Field et al. (2006) proposed a scheme to reject shattered particles from the data sets. Therefore, the interarrival time (IAT), which is the time between two successive particle counts, needs to be measured. Based upon the assumption that particles are randomly distributed in space, the interarrival time (IAT) for natural cloud particles is estimated to be Poisson distributed. Field et al. (2006) showed that the interarrival time distribution of a set of particles, contaminated by shattered particles, can be represented by a two Poisson process (cf Figure A.4), where the shattered artifacts do have significantly lower InterArrival Time (IAT) times:

$$\mathrm{P}\left(\Delta \mathrm{t} > \Delta \mathrm{t_i}\right) = \mathrm{A} \cdot e^{-\frac{\delta \mathrm{t}}{\tau_1}} + (1 - \mathrm{A}) \cdot e^{-\frac{\delta \mathrm{t}}{\tau_2}} \tag{A.18}$$

where P is the probability of finding interarrival times larger than δt, A is the fraction of particles associated with IAT τ_1 and A $-$ 1 is the fraction of particles associated with IAT τ_2.
The easiest way to sort out shattered particles from the measurements, is to reject all particles with interarrival times smaller than a given threshold τ_c. This threshold can be defined by the user or it can be set automatically as for example 0.05 time the larger peak value. Generally, the user needs to estimate the severity of the shattering process to accurately determine the threshold τ_c. A disadvantage of this method is that also natural cloud particles might be removed by this algorithm in case the two IAT distributions overlap. Then, natural cloud particles will also be rejected from the Poisson tail of the natural cloud particle distribution. The fraction of falsely rejected particles is $1 - e^{-\frac{\tau_c}{\tau_1}}$. Additionally, the leading particle of the shattered particle cloud is not removed by the rejection of all particles with interarrival times smaller τ_c. This is because the time between the first shattered particle and the last natural cloud particle is long compared to the interarrival times between the shattered particles. The corrected total number concentration of particles ($\mathrm{N_{total}}$) is given by:

$$\mathrm{N_{total}} = \mathrm{N_{accepted}} \cdot \frac{1}{2 \cdot e^{-\frac{\tau_c}{\tau_1}} - 1} \tag{A.19}$$

where $\mathrm{N_{accepted}}$ is the total number of particles with interarrival times (IAT) above τ_c.

This correction scheme can only be applied to data sets where the individual particle IATs are stored. The NIXE-CAS PBP dataset contains this information. The NIXE-CAS

frequency histogram data set provides an interarrival time (IAT) frequency distribution which can be used to correct the total number concentration contained in that file.

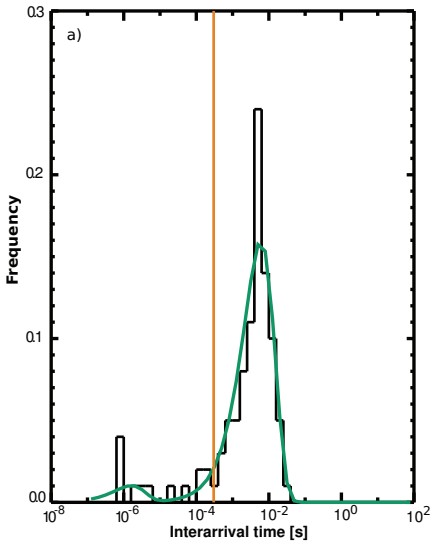

Figure A.4.: Example of a NIXE-CAS interarrival time distribution in black and a two Poisson distribution fit in green.

Particle coincidence:
Another source of error in the NIXE-CAS measurements occurs when clouds contain high numbers of particles. Then, the probability that two particles coincide in the NIXE-CAS sample volume increases. Moreover, the active time within which the NIXE-CAS processes information increases with increasing cloud particle number concentration. A measure to estimate the time which the instrument needs to process the particle information is the activity A_c. The activity of the NIXE-CAS consists of the time period for which a particle is present in the sample volume and the time period the NIXE-CAS electronics needs to process the scattered intensity. Particles which enter the NIXE-CAS sample volume during the active time are not counted. Several authors examined the effect of coincidence and dead-time losses and supplied different correction schemes. Baumgardner (1983) suggested a simple correction scheme based on the measurement of the activity:

$$N_m = N_a \cdot (1 - m \cdot A_c) \tag{A.20}$$

where N_m is the measured number of particles, N_a is the actual number of particles, A_c is the measured activity and m is a probe-dependent correction factor (Dye and Baumgardner, 1984). The manufacturer suggests a probe-dependent correction factor of 0.7 to

0.8. Nevertheless, m is dependent on the individual instruments electronic and optical responses (Baumgardner et al. (1985)) and might deviate from that value.
Baumgardner et al. (1985) improved the correction algorithm by Baumgardner (1983) based upon statistical estimation of the number of undetected particles due to coincidence and dead-time. They suggested two correction schemes, a quadratic and an iterative correction. These types of correction schemes rely upon an identification of several instrument characteristics such as the beam width, the length of the depth of field (DOF) or the length of the beam outside the DOF. These characteristics are unknown for most instruments and thus these correction schemes are often not applicable.
A simpler correction algorithm bases upon a statistical analysis of the probability of coincident particles and dead-time losses (Brenguier and Amodei, 1989, Brenguier, 1989). The correction scheme only requires the knowledge of a limited number of additional information such as slow and fast reset (explained below), time response of the amplifiers (for standard instruments between 0.4 µs to 0.6 µs) and the measurement of the number of slow or fast resets or total resets. Slow and fast resets are the time periods in which the NIXE-CAS electronics is active after a particle traveled through the depth of field (DOF) or the outer regions of the laser beam. For a complete description of the correction scheme the reader is referred to Brenguier and Amodei (1989), Brenguier (1989), Brenguier et al. (1994). The newer NIXE-CAPS instruments provide measurements of fast and slow resets (included in the histogram data set) and thus this algorithm can easily be applied and is normally more accurate than the one proposed by Baumgardner (1983). This correction scheme is currently being implemented into the Jülich evaluation program.
A different approach, called slope method, is described by Baumgardner et al. (1993). They proposed a correction scheme based upon the measurement of interarrival times (IAT) between successive particles. The particle concentration N is related to the average rate of particle detection α:

$$\mathrm{N} = \frac{\alpha}{\mathrm{A} \cdot \mathrm{v}} \tag{A.21}$$

where A is the area defined by the beam diameter and v is the airspeed.
The average rate of droplet detection can be estimated from the measured interarrival time (IAT) distribution. Nevertheless, the IAT distribution $\mathrm{P} = \mathrm{C} \cdot e^{-\alpha \mathrm{t}}$ is affected by coincidence and dead-time losses. Baumgardner et al. (1993) showed that the normalization coefficient C and the tail of the distribution containing the small interarrival times changes. But the majority of the distribution is unaffected by coincidence and dead-time losses. Thus, α is equal to the slope of the IAT distribution when the first τ_m bins of the IAT histogram are neglected. The algorithm is described in detail in Baumgardner et al. (1993).
Another useful method to correct the measured total number concentration is the compensation method also suggested by Baumgardner et al. (1993). This method is similar to the slope method and thus also based upon the measurement of interarrival times. From each interarrival time (IAT) a fixed time $\mathrm{t_m}$ is subtracted. Negative times and a fraction of the

zero values are ignored. The fraction f is determined iteratively by:

$$\mathrm{f} = \frac{e^{\alpha}}{e^{\alpha} + 1} \tag{A.22}$$

The average rate of particles α is then calculated by dividing the number of arrivals by the sum of their IATs.

According to Brenguier et al. (1994) the rates determined from the Brenguier (1989) coincidence equations and the rate determined from the slope method are between the maximum and average rate of the sample. The rate determined by the compensation method is somewhat less than the average rate. Thus, the calculation of all correction schemes can locate the true number concentration within a narrow range. The correction schemes should not be applied below concentration of 750 cm^{-3}, because uncertainties in the measured activity and other parameters lead to number concentrations with increased uncertainty compared to the measured ones.

Scattering ambiguities:
A further correction needs to be applied when highly aspherical particles are sized. One assumption made to compute the particle size is that scattering in the forward direction is assumed to be shape independent. Then, the Mie scattering curves, which are easy to calculate, are applicable to all particle types. Borrmann et al. (2000) simulated the scattering characteristics of different particle sizes and spheroidal shapes for the instrument setup using a T-matrix model. They found out that the scattering curve is different for different asphericities. Thus, to accurately measure the particle size the scattering intensities for the appropriate particle asphericities need to be modeled. Within the Jülich evaluation program T-matrix and geometric optics calculation results are embedded to correctly relate the measured scattering intensity to the size of the aspherical particles (see Section 3.1.3).

A.5.2. NIXE-CIP

For the NIXE-CIP dataset, corrections are only applied to raw image evaluation.

Particle image processing:
The images are processed by the SODA software in order to determine the particle sizes and shapes. At first, the SODA program reads and decompresses the image data. Before each image is sized, corrections can be applied to minimize particle distortions, originating from different sources.
First of all, the velocity used to record the particle images is controlled. For laboratory experiments a constant velocity is predefined which is normally set to values larger than the maximum of the expected sample airspeed. Thus, an oversampling of the particles occur and the images are elongated. The measured NIXE-CIP velocity during airborne

experiments might be imprecise. The images can afterwards be multiplied by the ratio of precise air velocity to the air velocity used for the image acquisition to correct their shapes. The distortions of the particles can also have other reasons. To reject particles which are not measured within the focus of the optical setup, the depth of field (DOF) criterion by Knollenberg (1970) is applied (Section 3.2.1). A number of authors, for example Korolev et al. (1991), Korolev et al. (1998) and experimentally Strapp et al. (2001), showed that the distortions of particle images and sizes can be significantly larger than 10 % as predicted by Knollenberg (1970). The reason is that the measured size obtained from the 50 % occultation condition is an oscillating function of the displacement of the particle from the center of field (COF). Thus, particles with a larger displacement as predicted by Knollenberg (1970) may be accepted. This leads to a sizing error of up to 65 % for particles smaller than 60 µm. The sizing for small spherical particles can be significantly improved by applying a correction scheme suggested by Korolev (2007b). The correction involves measuring the diameter of the Poisson spot D_{spot} and the outer edge diameter of the particle image D_{edge}. Korolev (2007b) produced a look-up table based on a Fresnel diffraction model where a correction factor is determined based upon the measured ratio D_{spot}/D_{edge}. Joe and List (1987), Reuter and Bakan (1998) and Korolev et al. (1998) furthermore suggest to take advantage of different shadow levels to improve the sizing of small particles. Korolev et al. (1998) furthermore introduced a correction algorithm based upon the analysis of an ensemble of particles. Unfortunately all these correction schemes can only be applied to spherical particles and not to aspherical ice crystals. This is due to the form and size of the Poisson spot which does not change in the same way for aspherical particles and spherical particles that pass the laser beam away from the center of field (COF). Up to now, only the basic Korolev (2007b) correction is implemented within the SODA program. Fortunately the sizing of particles larger than 60 µm is quite accurate. Thus, a combination of the small NIXE-CAS and the larger NIXE-CIP particle size measurements is done to minimize the sizing uncertainties.

For the calculation of the NIXE-CIP depth of field (DOF), the response time of the detector electronics is another detail to take care of. Baumgardner and Korolev (1997) discovered that an increase in the electronic response time leads to a decrease of the shading and thus a decrease in the minimum measurable particle size. They suggested an airspeed correction to the DOF. However, the electronic system of the Jülich NIXE-CIP is designed to allow aircraft operations for velocities larger than 200 m/s. The above mentioned airspeed correction does not need to be implemented for the Jülich instrument.

The main step in the SODA program is the determination of the size of each particle image. The operator can choose between 5 different sizing methods: 'x-sizing', 'y-sizing', 'circle fit', 'area equivalent size' and 'maximum dimension'. The size of the image for the 'x-' and 'y-'sizing methods is equal to the highest number of illuminated detector elements in the x- or y-direction of each image. The size obtained with the 'circle-fit' method is equal to the diameter of the smallest circle which encloses the whole particle. To obtain the 'area equivalent size', the projected particle area of each particle is determined and the equivalent size of a circle enclosing the same area is calculated. Alternatively, the maximum dimension of the crystal is obtained with the 'maximum dimension' technique. For spherical particles,

all these sizes are equal, for aspherical particles they are not. The applied sizing method should be matched to the scientific question and must be clearly stated in the output data file.
The SODA program also includes a rejection scheme for particles. Depending on the chosen method to calculate the effective array width (EAW) (Section 3.2.1), particles that shade the first and/or last detector element can be rejected. To eliminate streakers caused by splashing or particles and particles traveling with a lower speed through the sample volume (SV) than the airspeed are also rejected. Therefore, all particles with an area ratio below 0.1 are sorted out. The area ratio is the shaded particle area divided by the area covered by a circle with the above determined diameter. This rejection criteria also removes most of the images where more than one particle is present in the depth of field (DOF) at the same time. If the time between one particle and the previous one is negative, the particle will be rejected due to a bad time stamp. To remove shattered artifacts particles are sorted out by the interarrival time (IAT) correction scheme which is described in Section A.5.1.

Particle shape determination:
Lastly, a scheme to identify the particle shape from the NIXE-CIP images is implemented within the Jülich evaluation program. To automatically identify the particle shape from the measured NIXE-CIP images, several methods are published. Rahman et al. (1981) and Hunter et al. (1984) used different methods involving Fourier transformations to determine the particle shape. In contrast, Duroure et al. (1994), Korolev and Sussman (2000) and Holroyd (1987) employed simple measurements of diameter, perimeter, area and x and y dimensions of the particle. The particle habits are derived from ratios of these geometrical measures. Within the Jülich evaluation program, the method proposed by Korolev and Sussman (2000) is implemented. A special characteristic of the Korolev and Sussman (2000) habit scheme is, that the particles are not classified separately. Rather the distributions $B(R_1)$ and $B(R_2)$ of two different geometric measures R_1 and R_2 (defined below) for a particle ensemble of at least 100 particles is analyzed. Additionally, for this thesis only particles with diameters larger than 67.5 µm which corresponds to at least 4 pixels along the sizing direction, are accepted for habit classification. The algorithm distinguishes 4 different particle habits: spherical, needle like, dendrite and irregular particles.
For complete images the ratio R_1 is calculated to sort the particles into the four classes:

$$R_1 = \frac{\pi \left({D_x}^2 + {D_y}^2 \right)}{8S} = \frac{\pi \left({N_x}^2 + {N_y}^2 \right)}{8N_{tot}} \tag{A.23}$$

where N_x, N_y are the number of shaded diodes in x- and y- direction. N_{tot} represents the total number of shaded diodes. D_x, D_y are the equivalently deduced particle diameters and S represents the total projected particle area.
For partial images the perimeter of the particle P_p is compared to the perimeter of the reconstructed particle assuming it to be a circle P_{circ}:

$$R_2 = \frac{P_p}{P_{circ}} \tag{A.24}$$

The derivation of the actual particle perimeter and the perimeter of a reconstructed image assuming the particle to be circular, are explained in detail in Korolev and Sussman (2000). Furthermore, the basic distributions $B_i(R_1)$ and $B_i(R_2)$ of the dimensionless ratios R_1 and R_2 for clouds containing only one of the four different particle habits, based upon a test data set, are also presented in Korolev and Sussman (2000).
A measured distribution M(R) of the different geometric measures for an ensemble of particles, can then be represented by:

$$M(R) = \sum_i f_i B_i(R) \tag{A.25}$$

where f_i is the fraction of particles in the ith habit and $B_i(R)$ is the distribution of the geometric measure R for particles of the ith habit. M(R) and $B_i(R)$ are normalized and $\sum_i f_i = 1$.
Thus, the actual fraction f of particles classified into the ith habit category for each geometric measure R can be calculated as follows:

$$f = B^{-1}M \tag{A.26}$$

Finally, the number of partial and complete images N_p and N_c must be taken into account to determine the fraction of all particles being classified within the ith habit:

$$f = \frac{N_c f_c + N_p f_p}{N_c + N_p} \tag{A.27}$$

The above described algorithm is limited to the four categories. Unfortunately, spherical ice crystals (e.g. plates) can not be distinguished from spherical liquid droplets. The fraction of frozen particles (= irregular + needle like + dendric ice crystals) should thus be understood as a lower ice fraction threshold.

A.6. NIXE analysis setup

Parameter	AIDA	BAE146
CAS shattering correction	no	yes
CIP shattering correction	no	yes
CAS coincidence monitoring	yes	yes
CAS airspeed correction	yes	no
CIP airspeed correction	yes	no
CAS aspherical particle correction	A/B=0.75	A/B=0.75
CIP sizing method	eqiuvalent area size	equivalent area size
CIP out of focus correction for water droplets	yes	no
CIP sample volume detection	all-in method	all-in method

Table A.3.: NIXE-CAPS post-processing adjustments

A.7. List of abbreviations

A/D	analog to digital
AIDA	Aerosol Interaction and Dynamics in the Atmosphere
APS	Aerodynamic Particle Sizer
CCN	Cloud Condensation Nuclei
COALESC	Combined Observation of the Atmospheric boundary Layer to study the Evolution of StratoCumulus
COF	Center Of Focus
DOF	Depth Of Field
EAW	Effective Array Width
EBD	Effective Beam Diameter
HALO	High Altitude and LOng range reseach aircraft
IAT	InterArrival Time
IEK-7	Institute of Energy and Climate Research - 7
IN	Ice Nuclei
IWC	Ice Water Content
IWP	Ice Water Path
KIT	Karlsruhe Institute of Technology
LIDAR	LIght Detection And Ranging
LWC	Liquid Water Content
LWP	Liquid Water Path
NCAR	National Center for Atmospheric Research
NIXE-CAS	Novel Ice EXpEriment - Cloud and Aerosol Spectrometer
NIXE-CAPS	Novel Ice EXpEriment - Cloud and Aerosol Particle Spectrometer
NIXE-CIP	Novel Ice EXpEriment - Cloud Imaging Probe
OPC	Optical Particle Counter
PADS	Particle Analysis and Display System
PBP	Particle by Particle
PHIPS	Particle Habit Imaging and Polar Scattering
SA	Sample Area
SID3	Small Ice Detector 3
SIMONE	Scattering Intensity Measurements for the Optical detectioN of icE
SMPS	Scanning Mobility Particle Sizer
SLM	Standard Liters per Minute
SV	Sample Volume
TDLAS	Tunable Diode Laser Absorption Spectroscopy
2-DS	2 - Dimensional Stereo probe

UK	United Kingdom
WBF	Wegener-Bergeron-Findeisen
WELAS	WhitE Light ScAttering Spectrometer
WELAS1	WhitE Light ScAttering Spectrometer 1
WELAS2	WhitE Light ScAttering Spectrometer 2
VIPS	Video Ice Particle Sampler

A.8. Mathematical notation

Symbol	Description	Unit
A_c	activity	
e_{gas}	air pressure	hPa
T	air temperature	K
v	air velocity	ms^{-1}
$\mathbb{S}$	amplitude scatttering matrix	
δ_l	bulk linear depolarization ratio	
COF	center of focus	m
r	cloud particle radius (liquid and/or ice)	µm
T_k	cloud temperature	K
I_R	right-circularly polarized intensity	$\mu Wcm^{-2}nmsr^{-1}$
I_L	left-circularly polarized intensity	$\mu Wcm^{-2}nmsr^{-1}$
γ	cooling rate	Ks^{-1}
a_c	critical Köhler radius	µm
s_c	critical Köhler saturation	
A	cross section	m^2
ρ	density	gm^{-3}
T_d	dew point	K
D_{edge}	diameter of particle edge	µm
D_{spot}	diameter of Poisson spot	µm
σ_i	differential scattering cross section	m^2sr^{-1}
b	distance between lens and particle	m
EAW	effective array width	cm^{-2}
R_{eff}	effective radius (liquid and/or ice)	µm
$s_{v/l}$	equilibrium Köhler saturation	
f	focal length	m
T_f	frost point	K
λ	laser wavelength	µm
P_l	linear polarization	
a	liquid droplet radius	µm
M_l	liquid molar weight	$kgmol^{-1}$
$LWC = W_{liq}$	liquid water content	gm^{-3}
LWP	liquid water path	gm^{-2}
μ	ice fraction	%
$IWC = W_{ice}$	ice water content	gm^{-3}
IWP	ice water path	gm^{-2}
n_{IN,T_k}	ice nuclei (IN) active concentration	cm^{-3}
I	intensity	kgs^{-3}
τ_1, τ_2, τ_c	interarrival time	ms

Symbol	Description	Unit
Q	mass air flow	kgs^{-1}
M(R)	measured distribution of geometrical measure R	
$n_{aer,0}$	number concentration of aerosol particles larger than 0.5 µm	cm^{-3}
dN_{dlogD_p}	normalized number concentration	cm^{-3}
dN	unnormalized number concentration	cm^{-3}
N	number of cloud particles	
N_i	number of ice crystals	
N_x	number of shaded diodes in x direction	
N_y	number of shaded diodes in y direction	
X	number of shaded NIXE-CIP diodes	
J	nucleation rate	$s^{-1}m^{-3}$
τ	optical thickness	
$E_{\parallel}$	parallel electric field vector	Vm^{-1}
$I_{\parallel}$	parallel polarized intensity	$\mu Wcm^{-2}nmsr^{-1}$
D_p	particle diameter	µm
D_x	particle diameter in x direction	µm
D_y	particle diameter in y direction	µm
P_p	particle perimeter	µm
S	particles projected area	μm^2
α	particle rate	s^{-1}
C	peak A/D value	
$E_{\perp}$	perpendicular electric field vector	Vm^{-1}
$I_{\perp}$	perpendicular polarized intensity	$\mu Wcm^{-2}nmsr^{-1}$
I_{+}	polarized intensity rotated by 45°	$\mu Wcm^{-2}nmsr^{-1}$
I_{-}	polarized intensity rotated by −45°	$\mu Wcm^{-2}nmsr^{-1}$
P	probability	%
r_d	radial distance	m
n	refractive index	
RH_i	relative humidity with respect to ice	%
RH_w	relative humidity with respect to water	%
res	resolution	µm
m_s	salt mass	kg
SA	sample area	cm^2
t	sample time	s
SV	sample volume	cm^3
e_w	saturation pressure with respect to water	hPa
e_i	saturation pressure with respect to ice	hPa
θ	scattering angle	
ϕ	scattering angle	
$\mathbb{Z}$	scattering phase matrix	

Symbol	Description	Unit
I,Q,U,V	Stokes vector components	$\mu Wcm^{-2}nmsr^{-1}$
$\sigma_{l/a}$	surface tension of water	kgs^{-2}
B(R)	theoretical distribution of geometrical measure R	
N_{tot}	total cloud particle concentration (liquid and/or ice)	m^{-3}
I_{tot}	total intensity	kgs^{-3}
R	universal gas constant	$Jkg^{-1}mol^{-1}$
u_z	updraft velocity	ms^{-1}
ν	viscosity	m^2s^{-1}
k	wave vector	cm^{-1}

Bibliography

Abdelmonem, A., M. Schnaiter, P. Amsler, E. Hesse, J. Meyer, and T. Leisner, 2011: First correlated measurements of the shape and scattering properties of cloud particles using the new Particle Habit Imaging and Polar Scattering (PHIPS) probe. *Atmospheric Measurement Techniques*, 4:2125–2142, doi:10.5194/amt-4-2125-2011.

Abel, S., 2011: personal communication.

Archuleta, C., P. DeMott, and S. Kreidenweis, 2005: Ice nucleation by surrogates for atmospheric mineral dust and mineral dust/sulfate particles at cirrus temperatures. *Atmospheric Chemistry and Physics*, 5:2617–2634, doi:doi:10.5194/acp-5-2617-2005.

Bacon, N., B. Swanson, M. Baker, and E. Davis, 1998: Breakup of levitated frost particles. *Journal of Geophysical Research*, 103:13,763–13,775, doi:doi:10.1029/98JD01162.

Bailey, M. and J. Hallet, 2002: Nucleation effects on the habit of vapour grown ice crystals from 18 to 42°C. *Quarterly Journal of the Royal Meteorological Society*, 128:1461–1483, doi:10.1256/00359000260247318.

Bailey, M. and J. Hallet, 2004: Growth rates and habits of ice crystals between -20° and -70°C. *Journal of the Atmospheric Sciences*, 61:514–544, doi:10.1175/1520-0469(2004)061<0514:GRAHOI>2.0.CO;2.

Baker, B., 1992: Turbulent entrainment and mixing in clouds: A new observational approach. *Journal of the Atmospheric Sciences*, 49:387–404, doi:10.1175/1520-0469(1992)049<0387:TEAMIC>2.0.CO;2.

Baker, B. and R. Lawson, 2006: Improvement in determination of ice water content from two-dimensional particle imagery. Part i: Image-to-mass relationships. *Journal of Applied Meteorology and Climaterology*, 45:1282–1290, doi:10.1175/JAM2399.1.

Baumgardner, D., 1983: An analysis and comparison of five water droplet measuring instruments. *Journal of Applied Meteorology*, 22:891–910, doi:10.1175/1520-0450(1983)022<0891:AAACOF>2.0.CO;2.

Baumgardner, D., 1986: A new technique for the study of cloud microstructure. *Journal of Atmospheric and Oceanic Technology*, 3:340–343, doi:10.1175/1520-0426(1986)003<0340:ANTFTS>2.0.CO;2.

Baumgardner, D., 2011: personal communication.

Baumgardner, D., B. Baker, and K. Weaver, 1993: A technique for the measurement of cloud structure on centimeter scales. *Journal of Atmospheric and Oceanic Technology*, 10:557–565, doi:10.1175/1520-0426(1993)010<0557:ATFTMO>2.0.CO;2.

Baumgardner, D., J. Dye, B. Gandrud, K. Barr, K. Kelly, and K. Chan, 1996: Refractive indices of aerosols in the upper troposphere and lower stratosphere. *Geophysical Research Letters*, 23:749–752, doi:10.1029/96GL00707.

Baumgardner, D., J. Dye, B. Gandrud, and R. Knollenberg, 1992: Interpretation of measurements made by the forward scattering spectrometer probe (FSSP-300) during the airborne arctic stratospheric expedition. *Journal of Geophysical Research*, 97:8035–8046, doi:10.1029/91JD02728.

Baumgardner, D., J. Gayet, H. Gerber, A. Korolev, and C. Twohy, 2002: *Cloud properties and their impact on the environment*, chapter Clouds:Measurement techniques in-situ in the encyclopaedia of atmospheric science, pages 489–498. Academic Press, U.K.

Baumgardner, D., H. Jonsson, W. Dawson, D. O'Connor, and R. Newton, 2001: The cloud, aerosol and precipitation spectrometer: a new instrument for cloud investigations. *Atmospheric Research*, 59-60:251–264, doi:10.1016/S0169-8095(01)00119-3.

Baumgardner, D. and A. Korolev, 1997: Airspeed corrections for optical array probe sample volumes. *Journal of Atmospheric and Oceanic Technology*, 14:1224–1229, doi:10.1175/1520-0426(1997)014<1224:ACFOAP>2.0.CO;2.

Baumgardner, D., W. Strapp, and J. E. Dye, 1985: Evaluation of the forward scattering spectrometer probe. Part ii: Corrections for coincidence and dead-time losses. *Journal of Atmospheric and Oceanic Technology*, 2:626–632, doi:10.1175/1520-0426(1985)002<0626:EOTFSS>2.0.CO;2.

Beard, K., 1992: Ice initiation in warm-base convective clouds: An assessment of microphysical mechanisms. *Atmospheric Research*, 28:125–152, doi:doi:10.1016/0169-8095(92)90024-5.

Benz, S., 2006: *Experimente zur Eisnukleation von Wassertröpfchen und Sulfatpartikeln bei Temperaturen zwischen* $-65°C$ *und* $-30°C$. Ph.D. thesis, Fakultät fur Physik der Universität Karlsruhe (TH).

Bigg, E., 1996: Ice forming nuclei in the high Arctic. *Tellus B*, 48:223–233, doi:10.1034/j.1600-0889.1996.t01-1-00007.x.

Bohren, C. and D. Huffman, 1998: *Absorption and scattering of light by small particles*. John Wiley & Sons, Inc., doi:10.1002/9783527618156.

Borrmann, S., B. Luo, and M. Mishchenko, 2000: Application of the t-matrix method to the measurement of aspherical (ellipsoidal) particles with forward scattering optical particle counters. *Journal of Aerosol Science*, 31:789–799, doi:doi:10.1016/S0021-8502(99)00563-7.

Brenguier, J., 1989: Coincidence and dead-time corrections for particle counters. Part ii: High concentration measurements with an FSSP. *Journal of Atmospheric and Oceanic Technology*, 6:585–598, doi:10.1175/1520-0426(1989)006<0585:CADTCF>2.0.CO;2.

Brenguier, J. and L. Amodei, 1989: Coincidence and dead-time corrections for particle counters. Part i: A general mathematical formalism. *Journal of Atmospheric and Oceanic Technology*, 6:575–584, doi:10.1175/1520-0426(1989)006<0575:CADTCF>2.0.CO;2.

Brenguier, J., D. Baumgardner, and B. Baker, 1994: A review and discussion of processing algorithms for fssp concentration measurements. *Journal of Atmospheric and Oceanic Technology*, 11:1409–141, doi:10.1175/1520-0426(1994)011<1409:ARADOP>2.0.CO;2.

Buck research instruments L.L.C., 2008: *Model CR-2 hygrometer: Operating Manual*.

Burnet, F. and J.-L. Brenguier, 2002: Comparison between standard and modified forward scattering spectrometer probes during the small cumulus microphysics study. *Journal of Atmospheric and Oceanic Technology*, 19:1516–1531, doi:10.1175/1520-0426(2002)019<1516:CBSAMF>2.0.CO;2.

Cantrell, W. and A. Heymsfield, 2005: Production of ice in tropospheric clouds: A review. *Bulletin of the American Meteorological Society*, 86:795–807, doi:10.1175/BAMS-86-6-795.

Carey, L., J. Niu, P. Yang, J. Kankiewicz, V. Larson, and T. V. Haar, 2008: The vertical profile of liquid and ice water content in midlatitude mixed-phase altocumulus clouds. *Journal of Applied Meteorology and Climaterology*, 47:2487–2495, doi:10.1175/2008JAMC1885.1.

Cober, S., G. Isaac, A. Korolev, and J. Strapp, 2001: Assessing cloud-phase conditions. *Journal of Applied Meteorology*, 40:1967–1983, doi:10.1175/1520-0450(2001)040<1967:ACPC>2.0.CO;2.

Cziczo, D., K. Froyd, S. Gallavardin, O. Möhler, S. Benz, H. Saathoff, and D. Murphy, 2009: Deactivation of ice nuclei due to atmospherically relevant surface coatings. *Environmental Research Letters*, 4:044013 (9pp), doi:10.1088/1748-9326/4/4/044013.

DeMott, P., A. Prenni, X. Liu, S. Kreidenweis, M. Petters, C. Twohy, M. Richardson, T. Eidhammer, and D. Rogers, 2010: Predicting global atmospheric ice nuclei distributions and their impacts on climate. *Proceedings of the National Academy of Sciences of the United States of America*, 107:11217–11222, doi:10.1073/pnas.0910818107.

DeMott, P. J., K. Sassen, M. Poellot, D. Baumgardner, D. Rogers, S. Brooks, A. Prenni, and S. Kreidenweis, 2003: African dust aerosols as atmospheric ice nuclei. *Geophysical Research Letters*, 30:1732, doi:10.1029/2003GL017410.

DeMott, P. J., C. H. Twohy, and D. C. Rogers, 2006: Ice nuclei variability and ice formation in mixed-phase clouds. In *Sixteenth ARM Science Team Meeting Proceedings*.

Diehl, K., M. Simmel, and S. Wurzler, 2006: Numerical sensitivity studies on the impact of aerosol properties and drop freezing modes on the glaciation, microphysics, and dynamics of clouds. *Journal of Geophysical Research*, 111:D07202:1–15, doi:10.1029/2005JD005884.

Droplet Measurement Technologies, 2008a: *CIP / PIP image file structure*.

Droplet Measurement Technologies, 2008b: *CIP and CIP-GS interfaces document*.

Droplet Measurement Technologies, 2009: *Data Analysis User 's Guide*, doc-0222, rev a edition.

Duroure, C., H. Larsen, H. Isaka, and P. Personne, 1994: 2D image population analysis. *Atmospheric Research*, 34:195–205, doi:10.1016/0169-8095(94)90091-4.

Dye, J. and D. Baumgardner, 1984: Evaluation of the forward scattering spectrometer probe. Part i: Electronic and optical studies. *Journal of Atmospheric and Oceanic Technology*, 1:329–344, doi:10.1175/1520-0426(1984)001<0329:EOTFSS>2.0.CO;2.

Ebert, V., H. Teichert, C. Giesemann, H. Saathoff, and U. Schurath, 2005: Fasergekoppeltes In-situ-Laserspektrometer für den selektiven Nachweis von Wasserdampfspuren bis in den ppb-Bereich. *Technisches Messen*, 72:23–30, doi:10.1524/teme.72.1.23.56689.

Ehrlich, A., M. Wendisch, E. Bierwirth, J. Gayet, G. Mioche, A. Lampert, and B. Mayer, 2009: Evidence of ice crystals at cloud top of artic boundary-layer mixed-phase clouds derived from airborne remote sensing. *Atmospheric Chemistry and Physics*, 9:9401–9416, doi:10.5194/acp-9-9401-2009.

Ehrlich, A., M. Wendisch, E. Bierwirth, A. Herber, and A. Schwarzenböck, 2008: Ice crystal spape effects on solar radiative properties of artic mixed-phase clouds - dependence on microphysical properties. *Atmospheric Research*, 88:266–276, doi:10.1016/j.atmosres.2007.11.018.

Ervens, B., G. Feingold, K. Sulia, and J. Harrington, 2011: The impact of microphysical parameters, ice nucleation mode, and habit growth on the ice/liquid partitioning in mixed-phase arctic clouds. *Journal of Geophysical Research*, 116:D17205:1–19, doi:10.1029/2011JD015729.

Field, P., R. Cotton, D. Johnson, K. Noone, P. Glantz, P. Kaye, E. Hirst, R. Greenaway, C. Jost, R. Gabriel, T. Reiner, M. Andreae, C. Saunders, A. Archer, T. Choularton, M. Smith, B. Brooks, C. Hoell, B. Bandy, and A. Heymsfield, 2001: Ice nucleation in orographic wave clouds: Measurements made during INTACC. *Quarterly Journal of the Royal Meteorological Society*, 127:1493–1512, doi:10.1002/qj.49712757502.

Field, P., A. Heymsfield, and A. Bansemer, 2006: Shattering and particle interarrival times measured by optical array probes in ice clouds. *Journal of Atmospheric and Oceanic Technology*, 23:1357–1371, doi:10.1175/JTECH1922.1.

Field, P., R. Wood, and P. Brown, 2003: Ice particle interarrival times measured with a fast FSSP. *Journal of Atmospheric and Oceanic Technology*, 20:249–261, doi:10.1175/1520-0426(2003)020<0249:IPITMW>2.0.CO;2.

Fleishauer, R., V. Larson, and T. V. Haar, 2002: Observed microphysical structure of midlevel, mixed-phase clouds. *Journal of the Atmospheric Sciences*, 59:1779–1803, doi:10.1175/1520-0469(2002)059<1779:OMSOMM>2.0.CO;2.

Freudenthaler, V., F. Homburg, and H. Jäger, 1996: Optical properties of contrails from lidar measurements: Linear depolarization. *Geophysical Research Letters*, 23:3715–3718, doi:10.1029/96GL03646.

Fridlind, A., A. Ackerman, G. McFarquhar, M. Poellot, P. DeMott, A. Prenni, and A. Heymsfield, 2007: Ice properties of single-layer stratocumulus during the Mixed-Phase Artic Experiment: 2. model results. *Journal of Geophysical Research*, 112:D24202:1–25, doi:10.1029/2007JD008646.

Fu, Q. and K. Liou, 1993: parameterization of the radiative properties of cirrus clouds. *Journal of the Atmospheric Sciences*, 50:2008–2025, doi:10.1175/1520-0469(1993)050<2008:POTRPO>2.0.CO;2.

Garsteiger, J., 2011: personal communication.

Gayet, J., S. Asano, A. Yamazaki, A. Uchiyama, A. Sinyuk, O. Jourdan, and F. Auriol, 2002: Two case studies of winter continental-type water and mixed-phase stratocumuli over the sea. 1. microphysical and optical properties. *Journal of Geophysical Research*, 107:11–1 – 11–15, doi:10.1029/2001JD001106.

Gayet, J., P. Brown, and F. Albers, 1993: A comparison of in-cloud measurements obtained with six PMS 2D-C probes. *Journal of Atmospheric and Oceanic Technology*, 10:180–194, doi:10.1175/1520-0426(1993)010<0180:ACOICM>2.0.CO;2.

Gayet, J., G. Mioche, A. Dörnbrack, A. Ehrlich, A. Lampert, and M. Wendisch, 2009: Microphysical and optical properties of Artic mixed-phase clouds. the 9 april 2007 case study. *Atmospheric Chemistry and Physics*, 9:6581–6595, doi:10.5194/acp-9-6581-2009.

General Eastern Instruments, 1987: *Model 1011B: Dew point hygrometer for aircraft Preliminary operating manual*.

Gregory, D. and D. Morris, 1996: The sensitivity of climate simulations to the specification of mixed phase clouds. *Climate Dynamics*, 12:641–651, doi:10.1007/BF00216271.

Gultepe, I., D. Judak, R. Nissen, and J. Strapp, 2000: Dynamical and microphysical characteristics of arctic clouds during BASE. *Journal of Climate*, 13:1225–1254, doi:10.1175/1520-0442(2000)013<1225:DAMCOA>2.0.CO;2.

Haner, D. and B. McGuckin, 1997: Measurement of the depolarization of reflected light from spectralon. Article. URL `http://hdl.handle.net/2014/22623`.

Harrington, J., T. Reisin, W. Cotton, and S. Kreidenweis, 1999: Cloud resolving simulations of Artic stratus. Part ii: Transition-season clouds. *Atmospheric Research*, 55:45–75, doi:10.1016/S0169-8095(98)00098-2.

Heymsfield, A., 2007: On measurements of small ice particles in clouds. *Geophysical Research Letters*, 34:L23812, doi:10.1029/2007GL030951.

Heymsfield, A., S. Lewis, A. Bansemer, J. Iaquinta, and L. Miloshevich, 2002: A general approach for deriving the properties of cirrus and stratiform ice cloud particles. *Journal of the Atmospheric Sciences*, 59:3–29, doi:10.1175/1520-0469(2002)059<0003:AGAFDT>2.0.CO;2.

Heymsfield, A. and J. Parrish, 1978: A computational technique for increasing the effective sampling volume of the PMS 2-D particle size spectrometer. *Journal of Applied Meteorology*, 17:1566–1572, doi:10.1175/1520-0450(1978)017<1566:ACTFIT>2.0.CO;2.

Hobbs, P. and A. Rangno, 1985: ice particle concentrations in clouds. *Journal of the Atmospheric Sciences*, 23:2523–2549, doi:10.1175/1520-0469(1985)042<2523:IPCIC>2.0.CO;2.

Hobbs, P., A. Rangno, M. Shupe, and T. Uttal, 2001: Airborne studies of cloud structures over the Arctic Ocean and comparisons with retrievals from ship-based remote sensing measurements. *Journal of Geophysical Research*, 106:15,029–15,044, doi:10.1029/2000JD900323.

Holroyd, E., 1987: Some techniques and uses of 2D-C habit classification software for snow particles. *Journal of Atmospheric and Oceanic Technology*, 4:498–511, doi:10.1175/1520-0426(1987)004<0498:STAUOC>2.0.CO;2.

Hovenac, E. and J. Lock, 1993: Calibration of the forward-scattering spectrometer probe: Modeling scattering from a multimode laser beam. *Journal of Atmospheric and Oceanic Technology*, 10:518–525, doi:10.1175/1520-0426(1993)010<0518:COTFSS>2.0.CO;2.

Hu, Y., M. Vaughan, Z. Liu, B. Lin, P. Yang, D. Flittner, B. Hunt, R. Kuehn, J. Huang, D. Wu, S. Rodier, K. Powell, C. Trepte, and D. Winker, 2007: The depolarization - attenuated backscatter relation: CALIPSO lidar measurements vs. theory. *Optics Express*, 15:5327–5332, doi:10.1364/OE.15.005327.

Hunter, H., R. Dyer, and M. Glass, 1984: A two-dimensional hydrometeor machine classifier derived from observational data. *Journal of Atmospheric and Oceanic Technology*, 1:28–36, doi:10.1175/1520-0426(1984)001<0028:ATDHMC>2.0.CO;2.

Husar, R., D. Tratt, B. Schichtel, S. Falke, F. Li, D. Jaffe, S. Gassó, T. Gill, N. Laulainen, F. Lu, M. Reheis, Y. Chun, D. Westphal, B. Holben, C. Gueymard, I. McKendry, N. Kuring, G. Feldman, C. McClain, R. Frouin, J. Merrill, D. DuBois, F. Vignola, T. Murayama, S. Nickovic, W. Wilson, K. Sassen, N. Sugimoto, and W. Malm, 2001: Asian dust events of April 1998. *Journal of Geophysical Research*, 106:18,317–18,330, doi:10.1029/2000JD900788.

IMK-AAF and S. Vogt, 2011: Website. URL `http://www.imk-aaf.kit.edu/105.php`.

Joe, P. and R. List, 1987: Testing and performance of two-dimensional optical array spectrometers with greyscale. *Journal of Atmospheric and Oceanic Technology*, 4:139–150, doi:10.1175/1520-0426(1987)004<0139:TAPOTD>2.0.CO;2.

Johnson, B., 2011: personal communication.

Knollenberg, R., 1970: The optical array: An alternative to scattering or extinction for airborne particle size determination. *Journal of Applied Meteorology*, 9:86–103, doi:10.1175/1520-0450(1970)009<0086:TOAAAT>2.0.CO;2.

Knopf, D. and T. Koop, 2006: Heterogeneous nucleation of ice surrogates of mineral dust. *Journal of Geophysical Research*, 111:D12201, doi:10.1029/2005JD006894.

Korolev, A., 2007a: Limitations of the Wegner-Bergeron-Findeisen mechanism in the evolution of mixed-phase clouds. *Journal of the Atmospheric Sciences*, 64:3372–3375, doi:10.1175/JAS4035.1.

Korolev, A., 2007b: Reconstruction of the sizes of spherical particles from their shadow images. Part i: Theoretical considerations. *Journal of Atmospheric and Oceanic Technology*, 24:376–389, doi:10.1175/JTECH1980.1.

Korolev, A., 2011: personal communication.

Korolev, A. and P. Field, 2008: The effect of dynamics on mixed-phase clouds: Theoretical considerations. *Journal of the Atmospheric Sciences*, 65:66–86, doi:10.1175/2007JAS2355.1.

Korolev, A. and G. Isaac, 2003a: Phase transformation of mixed-phase clouds. *Quarterly Journal of the Royal Meteorological Society*, 129:19–38, doi:10.1256/qj.01.203.

Korolev, A. and G. Isaac, 2003b: Roundness and aspect ratio of particles in ice clouds. *Journal of the Atmospheric Sciences*, 60:1795–1808, doi:10.1175/1520-0469(2003)060<1795:RAAROP>2.0.CO;2.

Korolev, A. and G. Isaac, 2005: Shattering during sampling by OAPs and HVPS. Part i: Snow particles. *Journal of Atmospheric and Oceanic Technology*, 22:528–542, doi:10.1175/JTECH1720.1.

Korolev, A. and G. Isaac, 2006: Relative humidity in liquid, mixed-phase, and ice clouds. *Journal of the Atmospheric Sciences*, 63:2865–2880, doi:10.1175/JAS3784.1.

Korolev, A., G. Isaac, S. Cober, J. Strapp, and J. Hallett, 2003: Microphysical characterization of mixed-phase clouds. *Quarterly Journal of the Royal Meteorological Society*, 129:39–65, doi:10.1256/qj.01.204.

Korolev, A., S. Kuznetsov, Y. Makarov, and V. Novikov, 1991: Evaluation of measurements of particle size and sample area from optical array probes. *Journal of Atmospheric and Oceanic Technology*, 8:514–522, doi:10.1175/1520-0426(1991)008<0514:EOMOPS>2.0.CO;2.

Korolev, A. and I. Mazin, 2003: Supersaturation of water vapor in clouds. *Journal of the Atmospheric Sciences*, 60:2957–2974.

Korolev, A., J. Strapp, and G. Isaac, 1998: Evaluation of the accuracy of PMS optical array probes. *Journal of Atmospheric and Oceanic Technology*, 15:708–720, doi:10.1175/1520-0426(1998)015<0708:EOTAOP>2.0.CO;2.

Korolev, A. and B. Sussman, 2000: A technique for habit classification of cloud particles. *Journal of Atmospheric and Oceanic Technology*, 17:1048–1057, doi:10.1175/1520-0426(2000)017<1048:ATFHCO>2.0.CO;2.

Lawson, R., B. Baker, and C. Schmitt, 2001: An overview of microphysical properties of Artic clouds observed in May and July 1998 during FIRE ACE. *Journal of Geophysical Research*, 106:14,989–15,014, doi:10.1029/2000JD900789.

Lawson, R., D. O. 'Connor, P. Zmarzly, K. Waever, B. Baker, and Q. Mo, 2006: The 2D-S (stereo) probe: design and preliminary tests of a new airborne, high-speed, high-resolution particle imaging probe. *Journal of Atmospheric and Oceanic Technology*, 23:1462–1477, doi:10.1175/JTECH1927.1.

Lohmann, U. and K. Diehl, 2006: Sensitivity studies of the importance of dust ice nuclei for the indirect aerosol effect on stratiform mixed-phase clouds. *Journal of the Atmospheric Sciences*, 63:968–982, doi:10.1175/JAS3662.1.

Malinowski, S., M. Leclerc, and D. Baumgardner, 1994: Fractal analyses of high-resolution cloud droplet measurements. *Journal of the Atmospheric Sciences*, 51:397–413, doi:10.1175/1520-0469(1994)051<0397:FAOHRC>2.0.CO;2.

Marcolli, C., S. Gedamke, T. Peter, and B. Zobrist, 2007: Efficiency of immersion mode ice nucleation on surrogates of mineral dust. *Atmospheric Chemistry and Physics*, 7:5081–5091, doi:10.5194/acp-7-5081-2007.

McFarquhar, G. and S. Cober, 2004: Single-scattering properties of mixed-phase arctic clouds at solar wavelengths: Impacts on radiative transfer. *Journal of Climate*, 17:3799–3813, doi:10.1175/1520-0442(2004)017<3799:SPOMAC>2.0.CO;2.

McFarquhar, G., J. Um, M. Freer, D. Baumgardner, G. Kok, and G. Mace, 2007: Importance of small ice crystals to cirrus properties: Observations from the tropical warm pool international experiment (TWC-ICE). *Geophysical Research Letters*, 34:L13803, doi:10.1029/2007GL029865.

McFarquhar, G., M. Wendisch, A. Korolev, P. Brown, R. Jackson, G. Zhang, and J. Um, 2010: Ice/liquid phase partitioning in mixed-phase clouds. Workshop on airborne, in situ instrumentation to measure ice clouds, Seaside, Oregon, USA, 25-27 June 2010.

Mishchenko, M., J. Hovenier, and L. Travis, 2000: *Light scattering by nonspherical particles*. Academic Press.

Mishchenko, M., L. Travis, and A. Lacis, 2005: *Scattering, absorption, and emission of light by small particles*. NASA Goddard Institute for Space Studies.

Mitchell, D., 1996: Use of mass- and area-dimensional power laws for determining precipitation particle terminal velocities. *Journal of the Atmospheric Sciences*, 53:1710–1723, doi:10.1175/1520-0469(1996)053<1710:UOMAAD>2.0.CO;2.

Mitchell, D., R. Zhang, and R. Pitter, 1990: Mass-dimensional relationships for ice particles and the influence of riming on snowfall rates. *Journal of Applied Meteorology*, 29:153–163, doi:10.1175/1520-0450(1990)029<0153:MDRFIP>2.0.CO;2.

Möhler, O., S. Büttner, C. Linke, M. Schnaiter, H. Saathoff, O. Stetzer, R. Wagner, M. Krämer, A. Mangold, V. Ebert, and U. Schurath, 2005: Effect of sulfuric acid coating on heterogeneous ice nucleation by soot particles. *Journal of Geophysical Research-Atmospheres*, 110:D11210, doi:10.1029/2004JD005169.

Möhler, O., P. DeMott, G. Vali, and Z. Levin, 2007: Microbiology and atmospheric processes: the role of biological particles in cloud physics. *Biogeosciences*, 4:1059–1071, doi:10.5194/bg-4-1059-2007.

Möhler, O., P. Fieldenz, H. Saathoff, M. Schnaiter, R. Wagner, R. Cotton, M. Krämer, A. Mangold, and A. Heymsfield, 2006: Efficiency of the deposition mode ice nucleation on mineral dust particles. *Atmospheric Chemistry and Physics*, 6:3007–3021, doi:10.5194/acp-6-3007-2006.

Möhler, O., D. Georgakopoulos, C. Morris, S. Benz, V. Ebert, S. Hunsmann, H. Saathoff, M. Schnaiter, and R. Wagner, 2008: Heterogeneous ice nucleation activity of bacteria: new laboratory experiments at simulated cloud conditions. *Biogeosciences*, 5:1425–1435, doi:10.5194/bg-5-1425-2008.

Moss, S. and D. Johnson, 1994: Aircraft measurements to validate and improve numberical model parameterisations of ice to water ratios in clouds. *Atmospheric Research*, 34:1–25, doi:10.1016/0169-8095(94)90078-7.

Murphy, D., D. Cziczo, K. Froyd, P. Hudson, B. Matthew, A. Middlebrook, R. Peltier, A. Sullivan, D. Thomson, and R. Weber, 2006: Single-particle mass spectrometry of tropospheric particles. *Journal of Geophysical Research*, 111:D23S32, doi:10.1029/2006JD007340.

Murphy, D. and D. Thomson, 1997: Chemical composition of single aerosol particles at Idaho hill: Negative ion measurements. *Journal of Geophysical Research*, 102:6353–6358, doi:10.1029/96JD00859.

Murphy, D. M. and T. Koop, 2005: Review of the vapour pressures of ice and supercooled water for atmospheric applications. *Quarterly Journal of the Royal Meteorological Society*, 131:1539–1565, doi:10.1256/qj.04.94.

Nelson, J., 1998: Sublimation of ice crystals. *Journal of the Atmospheric Sciences*, 55:910–919, doi:10.1175/1520-0469(1998)055<0910:SOIC>2.0.CO;2.

Nicolet, M., O. Stetzer, and U. Lohmann, 2007: Depolarization rations of single ice particles assuming finit circular cylinders. *Applied Optics*, 46:4465–4476, doi:10.1364/AO.46.004465.

Niedermeier, D., S. Hartmann, R. Shaw, D. Covert, T. Mentel, J. Schneider, L. Poulain, P. Reitz, C. Spindler, T. Clauss, A. Kiselev, E. Hallbauer, H. Wex, K. Mildenberger, and F. Stratmann, 2010: Heterogeneous freezing of droplets with immersed mineral dust particles - measurements and parameterisation. *Atmospheric Chemistry and Physics*, 10:3601–3614, doi:10.5194/acp-10-3601-2010.

Niedermeier, D., R. Shaw, S. Hartmann, H. Wex, T. Clauss, J. Voigtländer, and F. Stratmann, 2011: Heterogeneous ice nucleation: bridging stochastic and singular freezing behavior. *Atmospheric Chemistry and Physics Discussion*, 11:3161–3180, doi:10.5194/acpd-11-3161-2011.

Oraltay, R. and J. Hallett, 2005: The melting layer: A laboratory investigation of ice particle melt and evaporation near 0°C. *Journal of Applied Meteorology*, 44:206–220, doi:10.1175/JAM2194.1.

Ou, S., K. Liou, X. Wang, D. Hagan, A. Dybdahl, M. Mussetto, L. Carey, J. Niu, J. Kankiewicz, S. Kidder, and T. H. V. Haar, 2009: Retrievals of mixed-phase cloud

properties during the national polar-orbiting operational environmental satellite system. *Applied Optics*, 48:1452–1462, doi:10.1364/AO.48.001452.

Pal, S. and I. Carswell, 1985: Polarization anisotropy in lidar multiple scattering from atmospheric clouds. *Applied Optics*, 24:3464–3471, doi:10.1364/AO.24.003464.

Paluch, I. and D. Baumgardner, 1989: Entrainment and fine-scale mixing in a continental convective cloud. *Journal of the Atmospheric Sciences*, 46:261–278, doi:10.1175/1520-0469(1989)046<0261:EAFSMI>2.0.CO;2.

Pinto, J., 1998: Autumnal mixed-phase cloudy boundary layers in the Arctic. *Journal of the Atmospheric Sciences*, 55:2016–2038, doi:10.1175/1520-0469(1998)055<2016:AMPCBL>2.0.CO;2.

Pinto, J., J. Curry, and J. Intrieri, 2001: Cloud-aerosol interactions during autumn over Beaufort Sea. *Journal of Geophysical Research*, 106:15,077–15,097, doi:10.1029/2000JD900267.

Prenni, A., J. Harrington, P. J. Tjernstrom, A. DeMott, A. Avramov, C. N. Long, S. M. Kreidenweis, P. Q. Olsson, and J. Verlinde, 2007: Can ice-nucleating aerosols effect Arctic seasonal climate? *BAMS*, 88:541–550, doi:10.1175/BAMS-88-4-541.

Pruppacher, H. and J. Klett, 1997: *Microphysics of clouds and precipitation.* Kluwer Academic Publishers, doi:10.1080/02786829808965531.

Rahman, M., E. Quincy, R. Jacquot, and M. Magee, 1981: Feature extinction and selection for pattern recognition of two-dimensional hydrometeor images. *Journal of Applied Meteorology*, 20:521–535, doi:10.1175/1520-0450(1981)020<0521:FEASFP>2.0.CO;2.

Rauber, R. and A. Tokay, 1991: An explanation for the existance of supercooled water at the top of cold clouds. *Journal of the Atmospheric Sciences*, 48:1005–1023, doi:10.1175/1520-0469(1991)048<1005:AEFTEO>2.0.CO;2.

de Reus, M., S. Borrmann, A. Bansemer, A. Heymsfield, R. Weigel, C. Schiller, V. Mitev, W. Frey, D. Kunkel, A. Kürten, J. Curtius, N. Sitnikov, A. Ulanovsky, and F. Ravegnani, 2009: Evidence for ice particles in the tropical stratosphere from in-situ measurements. *Atmospheric Chemistry and Physics*, 9:6775–6792, doi:10.5194/acp-9-6775-2009.

Reuter, A. and S. Bakan, 1998: Improvements of cloud particle sizing with a 2D-grey probe. *Journal of Atmospheric and Oceanic Technology*, 15:1196–1203, doi:10.1175/1520-0426(1998)015<1196:IOCPSW>2.0.CO;2.

Roberts, P. and J. Hallet, 1968: a laboratory study of the ice nucleating properties of some mineral particulates. *Quarterly Journal of the Royal Meteorological Society*, 94:25–34, doi:10.1002/qj.49709439904.

Sassen, K., 1991: The polarization lidar technique for cloud research: A review and current assessment. *Bulletin of the American Meteorological Society*, 72:1848–1866, doi:10.1175/1520-0477(1991)072<1848:TPLTFC>2.0.CO;2.

Sassen, K. and C. Hsueh, 1998: Contrail properties derived from high-resolution polarization lidar studies during SUCCESS. *Geophysical Research Letters*, 25:1165–1168, doi:10.1029/97GL03503.

Schnaiter, M., 2011: Website. URL `http://www.imk-aaf.kit.edu/55.php`.

Schnaiter, M., R. Schön, O. Möhler, H. Saathoff, and R. Wagner, 2007: Backscattering linear depolarization ratio of laboratory generated ice clouds composed of pristine and complex-shaped ice crystals. In *Tenth International Conference on Light Scattering by Non-spherical Particles*.

Shupe, M., P. Kollias, P. Persson, and G. McFarquhar, 2008: Vertical motions in artic mixed-phase stratiform clouds. *Journal of the Atmospheric Sciences*, 65:1304–1322, doi:10.1175/2007JAS2479.1.

Shupe, M. and S. Matrosov, 2006: Arctic mixed-phase cloud properties derived from surface-based sensors at SHEBA. *Journal of the Atmospheric Sciences*, 63:697–711, doi:10.1175/JAS3659.1.

Solomon, S., D. Qin, M. Manning, Z. Chen, M. Marquis, K. Averyt, M. Tignor, and H. Miller, 2007: *Contribution of working group I to the fourth assessment report of the Intergovernmental Panel on Climate Change, 2007*. Cambridge University Press.

Spangenberg, D., P. Minnis, S. Sun-Mack, M. Shupe, and M. Poellot, 2006: Chracterization of mixed-phase clouds during Mixed-Phase Arctic Cloud Experiment from satellite, ground-based, and in-situ data. In *Sixteenth ARM Science Team Meeting Proceedings*.

Steinke, I., O. Möhler, A. Kiselev, M. Niemand, H. Saathoff, M. Schnaiter, J. Skrotzki, C. Hoose, and T. Leisner, 2011: Ice nucleation properties of fine ash particles from the EyjafjallajÃűkull eruption in April 2010. *Atmospherc Measurement Techniques Discussion*, 11:17665–17698, doi:10.5194/acpd-11-17665-2011.

Strapp, J., F. Albers, A. Reuter, A. Korolev, U. Maixner, E. Rashke, and Z. Vukovic, 2001: Laboratory measurements of the response of a PMS OAP−2DC. *Journal of Atmospheric and Oceanic Technology*, 18:1150–1170, doi:10.1175/1520-0426(2001)018<1150:LMOTRO>2.0.CO;2.

Sun, Z. and K. Shine, 1994: Studies of the radiative properties of ice and mixed-phase clouds. *Quarterly Journal of the Royal Meteorological Society*, 120:111–137, doi:10.1002/qj.49712051508.

Takahashi, T., Y. Nagao, and Y. Kushiyama, 1995: Possible high ice particle production during graupel-graupel collisions. *Journal of the Atmospheric Sciences*, 52:4523–4527, doi:10.1175/1520-0469(1995)052<4523:PHIPPD>2.0.CO;2.

Thomas, A., 2003: *Flugzeuggestützte Messungen des atmosphärischen Aerosols: Saharastaub, stratosphärisches Hintergrundaerosol und nichtsichtbare Wolken in den Tropen*. Ph.D. thesis, Johannes Gutenberg-Universität.

Tremblay, A., A. Glazer, W. Yu, and R. Benoit, 1996: A mixed-phase cloud scheme based on a single prognostic equation. *Tellus A*, 48:483–500, doi:10.1034/j.1600-0870.1996.t01-3-00001.x.

Viadaurre, G. and J. Hallett, 2009: Ice and water content of stratiform mixed-phase cloud. *Quarterly Journal of the Royal Meteorological Society*, 135:1292–1306, doi:10.1002/qj.440.

Wendisch, M., A. Keil, and A. Korolev, 1996: FSSP characterization with monodisperse water droplets. *Journal of Atmospheric and Oceanic Technology*, 13:1152–1165, doi:10.1175/1520-0426(1996)013<1152:FCWMWD>2.0.CO;2.

Zobrist, B., T. Koop, B. Luo, C. Marcolli, and T. Peter, 2007: Heterogeneous ice nucleation rate coefficient of water droplets coated by a nonadecanol monolayer. *Journal of Physical Chemistry C*, 111:2149–2155, doi:10.1021/jp066080w.

Zobrist, B., C. Marcolli, T. Peter, and T. Koop, 2008: Heterogeneous ice nucleation in aqueous solutions: The role of water activity. *Journal of Physical Chemistry A*, 112:3965–3975, doi:10.1021/jp7112208.

Zuberi, B., A. Bertram, T. Koop, L. Molina, and M. Molina, 2001: Heterogeneous freezing of aqueous particles induced by crystallized (NH4)(2)SO4, ice, and letovicite. *Journal of Physical Chemistry A*, 105:6458–6464, doi:10.1021/jp010094e.

Acknowledgements

For the completion of this thesis a number of persons contributed whom I would like to express my sincere thanks.
First of all I would like to thank Prof. Martin Riese and Dr. Martina Krämer for offering me the possibility to start this work at IEK-7 (Forschungszentrum Jülich) and to give me the opportunity to take part in a number of research campaigns, workshops and summer schools all over the world. Special thanks to Martina Krämer for listing to my problems and to always providing a different perspective to the topic in question. Thank you to Martin Riese who frequently took the time for personal discussions and who always had a look at the time schedule of this thesis.
I would also like to especially thank Armin Afchine who provided the technical background for the operation of the NIXE-CAPS at IEK-7. He also supervised a number of experiments and the NIXE-CAPS repairs. Thank you also to Reimar Bauer who helped with the IT equipment and Nicole Spelten who helped me with additional technical equipment.
Without the great support of the company who build the instrumentation used for this thesis, the measurements could not have been performed as smoothly and as numerous. Special thanks to Darrel Baumgardner, Roy Newton, Gary Granger and the whole Droplet Measurement team for always providing the instrumentation in time and for all the personal support. Especially Darrel Baumgardner spent a lot of time to answer all my questions and to point my thoughts into the right direction.
I am also very grateful for the opportunities to perform laboratory experiments at the AIDA chamber at IMK-AAF (Karlsruhe Institute of Technology) and airborne measurements on board the british aircraft BAE146. Special thanks to Martin Schnaiter, Ottmar Möhler, Phil Brown, Mo Smith and Doug Anderson for giving us the opportunity to take part in the AIDA research campaigns HALO02, ACI03, ACI04 and BIO05 and the airborne campaign COALESC. Also thanks to the AIDA, the Metoffice and Directflight team for providing the technical support.
Thank you to Ottmar Möhler, Martin Schnaiter, Ahmet Abdelmonem, Stefan Benz, Monika Niemand, Caroline Ohm and Julian Skrotzki for providing additional data essential for the evaluation of the NIXE-CAPS measurements at the AIDA. Just like the AIDA team I would like to thank Carl Schmitt for forwarding me the VIPS measurements of the HALO02 campaign and also Alan Foster for providing me with additional measurements on board the BAE146. Special thanks to Josef Garsteiger who helped me with the T-Matrix and Geometric Optics calculations and provided additional data.
I would also like to thank Andy Heymsfield and Aaron Bansemer for allowing us to use their SODA software which helped me to evaluate the NIXE-CIP measurements. I am grateful for their support and patience to answer all my questions. Thank you also to Wiebke Frey who introduced me to the NIXE-CAPS instrumentation and analysis methods.
Sincere thanks to Prof. Ralf Koppmann and Prof. Francesco Knechtli for supervising this thesis alongside Prof. Martin Riese. A special thanks goes to the EOS programme in which

framework this thesis took part.
Finally, I would like to pass my gratitude to all members of IEK-7. I enjoyed working at the institute for the last years. In particular, the joint campaigns have been a pleasure. I am grateful to Cornelius Schiller who supported my first steps at the institute. Special thanks to my colleagues Tim Klostermann, Jochen Barthel, Miriam Kübbeler and Margit Hildebrandt with whom I shared the office and who witnessed all of my achievements and set backs. Without their support and conversations, my time at IEK-7 would not have been the same.
Last but not least, I need to especially thank my family for their assistance and encouragement. Especially my boyfriend Tilman Sanders who accompanied all of my ideas and the development of this thesis.

Band / Volume 146
Electron Spin Resonance Investigation of Semiconductor Materials for Application in Thin-Film Silicon Solar Cells
L. Xiao (2012), VIII, 147 pp.
ISBN: 978-3-89336-805-1

Band / Volume 147
Untersuchungen zum Sicherheits- und Transmutationsverhalten innovativer Brennstoffe für Leichtwasserreaktoren
O. Schitthelm (2012), V, 150 pp.
ISBN: 978-3-89336-806-8

Band / Volume 148
IEK-Report 2011. Klimarelevante Energieforschung
(2012), ca. 250 pp.
ISBN: 978-3-89336-808-2

Band / Volume 149
IEK-Report 2011. Climate-Relevant Energy Research
(2012), ca. 250 pp.
ISBN: 978-3-89336-809-9

Band / Volume 150
Netzintegration von Fahrzeugen mit elektrifizierten Antriebssystemen in bestehende und zukünftige Energieversorgungsstrukturen (2012)
ISBN: 978-3-89336-811-2

Band / Volume 151
Stratospheric ClOOCl chemistry at high solar zenith angles
O. Suminska-Ebersoldt (2012), VI, 126 pp
ISBN: 978-3-89336-817-4

Band / Volume 152
Keramiken und Keramikkombinationen zur Feinstpartikelabscheidung mit Hilfe thermisch induzierter Potentialfelder und Elektronenemissionen
D. Wenzel (2012), XXV, 155 pp
ISBN: 978-3-89336-820-4

Band / Volume 153
Bildung von sekundären Phasen bei tiefengeologischer Endlagerung von Forschungsreaktor-Brennelementen – Struktur- und Phasenanalyse
A. Neumann (2012), 329 pp
ISBN: 978-3-89336-822-8

Band / Volume 154
Coupled hydrogeophysical inversion for soil hydraulic property estimation from time-lapse geophysical data
M. Cho Miltin (2012), xi, 79 pp
ISBN: 978-3-89336-823-5

Band / Volume 155
Tiefentschwefelung von Flugturbinenkraftstoffen für die Anwendung in mobilen Brennstoffzellensystemen
Y. Wang (2012), 205 pp.
ISBN: 978-3-89336-827-3

Band / Volume 156
Self-consistent modeling of plasma response to impurity spreading from intense localized source
M. Koltunov (2012), V, 113 pp.
ISBN: 978-3-89336-828-0

Band / Volume 157
Phosphorsäureverteilung in Membran-Elektroden-Einheiten dynamisch betriebener Hochtemperatur-Polymerelektrolyt-Brennstoffzellen
W. Maier (2012), VI, 105 pp.
ISBN: 978-3-89336-830-3

Band / Volume 158
Modellierung und Simulation von Hochtemperatur-Polymerelektrolyt-Brennstoffzellen
M. Kvesic (2012), ix, 156 pp.
ISBN: 978-3-89336-835-8

Band / Volume 159
Oxidation Mechanisms of Materials for Heat Exchanging Components in CO_2/H_2O-containing Gases Relevant to Oxy-fuel Environments
T. Olszewski (2012), 200 pp.
ISBN: 978-3-89336-837-2

Band / Volume 160
Ice Crystal Measurements with the New Particle Spectrometer NIXE-CAPS
J. Meyer (2013), ii, 132 pp.
ISBN: 978-3-89336-840-2

Weitere ***Schriften des Verlags im Forschungszentrum Jülich*** unter
http://wwwzb1.fz-juelich.de/verlagextern1/index.asp

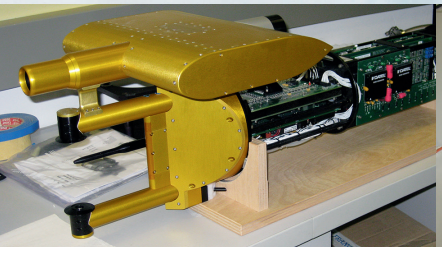

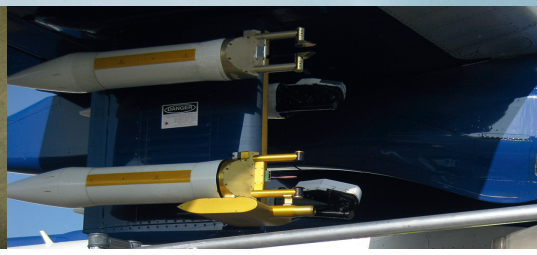

Energie & Umwelt / Energy & Environment
Band / Volume 160
ISBN 978-3-89336-840-2

JÜLICH
FORSCHUNGSZENTRUM